A multi-omics integrative approach unravels novel genes and pathways associated with senescence escape after targeted therapy in NRAS mutant melanoma

Vincent Gureghian[1], Hailee Herbst[1], Ines Kozar[2], Katarina Mihajlovic[3], Noël Malod-Dognin[3], Gaia Ceddia[3], Cristian Angeli[1], Christiane Margue[1], Tijana Randic[1], Demetra Philippidou[1], Milène Tetsi Nomigni[1], Ahmed Hemedan[4], Leon-Charles Tranchevent[4], Joseph Longworth[5], Mark Bauer[1], Apurva Badkas[1], Anthoula Gaigneaux[1], Arnaud Muller[6], Marek Ostaszewski[2], Fabrice Tolle[1], Nataša Pržulj[3,7,8*] and Stephanie Kreis[1*]

[*]co-last author

[1]Department of Life Sciences and Medicine, University of Luxembourg, 6, Avenue du Swing, L-4367 Belvaux, Luxembourg

[2]Laboratoire National de Santé, Dudelange, Luxembourg

[3]Barcelona Supercomputing Center, 08034 Barcelona, Spain and 3 ICREA, 08010 Barcelona, Spain

[4]Luxembourg Centre for Systems Biomedicine, University of Luxembourg, Esch-sur-Alzette, Luxembourg

[5]Experimental and Molecular Immunology, Department of Infection and Immunity, Luxembourg Institute of Health, Esch-sur-Alzette, Luxembourg

[6]LuxGen, TMOH and Bioinformatics platform, Data Integration and Analysis unit, Luxembourg Institute of Health, Luxembourg

[7]Department of Computer Science, University College London, London WC1E 6BT, UK

[8]ICREA, Pg. Lluís Companys 23, 08010 Barcelona, Spain

Corresponding author: stephanie.kreis@uni.lu

Competing interests

The authors declare that they have no competing interests.

Abstract

Therapy Induced Senescence (TIS) leads to sustained growth arrest of cancer cells. The associated cytostasis has been shown to be reversible and cells escaping senescence further enhance the aggressiveness of cancers. Together with targeted therapeutics, senolytics, specifically targeting senescent cancer cells, constitute a promising avenue for improved cancer treatments. Understanding how cancer cells evade senescence is needed to optimise the clinical benefits of this therapeutic approach. Here we characterised the response of three different NRAS mutant melanoma cell lines to a combination of CDK4/6 and MEK inhibitors over 33 days. Transcriptomic data show that all cell lines trigger a senescence programme coupled with strong induction of interferons. Kinome profiling revealed the activation of Receptor Tyrosine Kinases (RTKs) and enriched downstream signaling of neurotrophin, ErbB and insulin pathways. Characterisation of the miRNA interactome associates miR-211-5p with resistant phenotypes. Finally, iCELL-based integration of bulk and single-cell RNA-seq data identified biological processes perturbed during senescence, and predicts new genes involved in its escape. Overall, our data associate insulin signaling with persistence of a senescent phenotype and suggest a new role for interferon gamma in senescence escape through the induction of EMT and the activation of ERK5 signaling.

INTRODUCTION

Hayflick first observed in 1961 that fibroblasts stop proliferating after 50 passages and display an enlarged and flattened phenotype characteristic of senescence [1, 2]. This observation was later explained by the progressive shortening of telomeres upon replication, which ultimately triggers a DNA Damage Response (DDR) leading to cell cycle arrest [3, 4]. This process was called “replicative senescence”. Several cellular events and environmental conditions induce senescence, and it now emerges as a generic stress response involved in central biological processes such as embryonic development, wound healing and aging [2, 4, 5].

52 Many stressors that induce senescence (*e.g.*, oxidative stress, radiation), induce DNA damage and
53 activate DDR. This leads to engagement of the Senescence Associated Secretory Phenotype (SASP),
54 one of the characteristic features of senescence in which cells produce and secrete cytokines and
55 growth factors. The SASP itself can trigger senescence in adjacent cells and contributes to the
56 emergence of an inflammatory environment as the senescent cells, which are not eliminated by the
57 immune system, accumulate in the organism [5]. This accumulation leads to the development of
58 degenerative and hyperplastic pathologies and carcinogenesis, linking senescence to aging [6, 7].
59 Research in this field is challenging due to the heterogeneous and dynamic nature of the SASP and the
60 lack of a universal marker for senescence.

61 Focusing on cancer, the activation of known oncogenes results in a constant proliferative signaling
62 which causes replication forks to trigger DNA damage and drive primary cells to undergo oncogene-
63 induced senescence (OIS) [8]. Therefore, senescence may be considered as an early evolutionary
64 mechanism of protection against cancer leading to cell cycle arrest of over-proliferating cells [9].
65 However, cells can escape this arrest and re-establish growth, ultimately leading to the development
66 of cancer. Cancer cells can also undergo senescence when exposed to therapies, so called Therapy-
67 induced senescence (TIS).

68 Thus, senescence appears as a natural barrier against cancer, but recent works suggest that
69 senescence may be a reversible process [10]. Exit from senescence has been recently linked with the
70 stem-like properties of cancer cells, reinforcing the idea that aside from the SASP, senescence itself
71 may be a transient state in carcinogenesis.

72 Melanoma arises from the deregulated proliferation of melanocytes representing the deadliest type
73 of skin cancer accounting for about 75% of related deaths. Standard of care involves targeted
74 therapies and immunotherapies [11]. For the BRAF mutated subtype, representing half of the cases,
75 specific first line inhibitors targeting both MEK and BRAF have been developed. The NRAS mutated
76 subtype, which accounts for a quarter of all melanoma cases, lacks such a targeted approach but

77 ongoing clinical trials are assessing the effects of combined MEK and CDK4/6 inhibitors (NCT01781572;
78 NCT02065063). However, tolerance or resistance to such targeted treatments inevitably develops.

79 MicroRNAs have been shown to be involved in resistance to treatment. miRNAs are 20-22 nucleotides
80 short RNAs, which in complex with the Argonaute (AGO) protein, act as post-transcriptional regulators
81 of gene expression [12]. Canonically, miRNAs destabilise mRNAs by binding to a complementary
82 sequence within the 3' UTR, this resulting in downregulation of the mRNA and the encoded protein
83 [13]. Experimental methods based on immune-precipitation and sequencing have been developed to
84 profile miRNA-mRNA interactions. The qCLASH method has the advantage of capturing direct physical
85 interactions only, through an additional intermolecular ligation step linking mRNAs to their bound
86 miRNAs [14].

87 To characterise the response of 3 NRAS mutant melanoma cell lines to a combination of MEK and
88 CDK4/6 inhibitors, we treated the cells over 33 days and collected samples at multiple time points.
89 Samples were analyzed by total RNA-seq, small RNA-seq, qCLASH and kinome profiling. Our results
90 recapitulate several previous observations while displaying an unforeseen interplay between
91 interferon signalling and senescence. Additionally, we uncover deregulated processes associated with
92 the onset of senescence and its exit by adapting a non-negative matrix tri-factorization (NMTF)-based
93 methodology, "iCell" [15], to integrate bulk RNA-seq and single-cell data. Moreover, the
94 dimensionality reduction and the clustering properties of the NMTF allowed us to associate novel
95 genes to senescence escape.

96

97

98

99

100 **RESULTS**

101 **Experimental design and description of the data sets**

102 To study the effects of MEKi and CDK4/6i, 3 NRAS mutant melanoma cell-lines were selected: IPC298,
103 MELJUSO and SKMEL30. We determined the GI50 (drug concentration at which cell growth is reduced
104 by half) and opted for a concentration of 16nM, 110nM and 35nM of Binimetinib (MEKi) for IPC298,
105 MELJUSO and SKMEL30, respectively and 1 μM for Palbociclib (CDK4/6i) as this inhibitor led to
106 incomplete dose-response curves (Supp. Table 1). Upon treatment over 33 days, distinct cellular
107 responses (Fig. 1) were observed. IPC298 suffered very little from the treatment showing constant
108 proliferation and no morphological change. SKMEL30 stopped proliferating and accumulated
109 pigmentation before restoring proliferation after around 14 days. Finally, MELJUSO stopped dividing
110 and started to stretch to acquire a spindle-shape phenotype after 4 days.

111 As distinct morphological changes were observed at these time points, we profiled the transcriptome
112 of the cell lines at day 0, 4, 14 and 33 using total RNA-seq. Cellular signaling supporting the adaptation
113 to the treatment was investigated by profiling the kinome of the senescent MELJUSO and adaptative
114 SKMEL30 cell lines using PamGene technology. Next, we characterised the resistant miRNA
115 interactome of the SKMEL30 and IPC298 at 33 days by combining small RNA-seq and the qCLASH
116 method. Finally, by integrating bulk and single cell RNA-seq data, deregulated pathways and predicted
117 genes associated with senescence escape were identified.

118

119 **Cell lines display coherent transcriptomic profiles composed of interferons, EMT and senescent**
120 **responses under prolonged CDK4/6i and MEKi treatment**

121 Distinct cellular responses to treatment were reflected at the transcriptomic level where the cell lines
122 clustered separately on the PCA (Fig. 2.A). As MELJUSO displayed a different evolution over time, we
123 decided to analyze each cell line individually. Differential expression analysis, comparing later time

124 points to day 0, revealed a greater change in the MELJUSO transcriptome. MELJUSO corresponds to
125 9548, 11362 and 10126 significant (p.adj <= 0.05) differentially expressed genes at day 4, day 14 and
126 day 33, respectively when compared to SKMEL30 and IPC298 (9208, 9749, 6509 and 5436, 7575 and
127 3217, respectively) (Supp. Fig 1).

128 Gene Set Enrichment Analysis (GSEA) was performed on differentially expressed genes using the
129 "hallmarks" from MSigDB, which revealed the downregulation of pathways related to proliferation
130 such as "MYC TARGETS V1", "E2F TARGETS", and "G2M CHECKPOINT" (Fig. 2.B), all affected by our
131 inhibitors. The clustering of samples on top of the heatmap clearly separates proliferative samples
132 (left part) comprising the IPC298 cell line and SKMEL30 day 33 from cytostatic samples (right part)
133 with MELJUSO and early time points for SKMEL30. Interestingly, we noticed across all cell lines an
134 enrichment in interferon responses and an enrichment in Epithelial Mesenchymal Transition (EMT)
135 for the cytostatic samples (Fig 2.B). CDK4/6 inhibitors have been shown to induce cellular senescence
136 in different cell types [16, 17]. We therefore used a recently published classifier, "SENESCopedia", to
137 predict the levels of senescence in our samples (Fig. 2.C) [18]. On day 14, all cell lines display high
138 senescence scores suggesting that they all engage in a related transcriptional programme. Of note, all
139 samples with a high senescence score are also enriched in EMT which is coherent with previous
140 observations of EMT in different epithelial cell types after induction of senescence (fibroblasts,
141 colorectal and lung cancer) [19, 20, 21].

142 Altogether, these results suggest that all 3 cell lines trigger the same type of responses composed of
143 an interferon response, a senescence and "EMT" programme but with a different intensity and
144 temporality, which may explain the different phenotypes observed.

145

146 **Kinome profiling of adapting cell lines shows reactivation of RTK pathways and suggests a key role**
147 **of ERK5**

148 To better understand how the cell lines adapt to the treatment, we acquired PamGene data to profile
149 the kinome of SKMEL30 and MELJUSO cells at day 0, 1, 4 and 33 (Supp. Fig 2) as these two cell lines
150 showed distinct responses to combined kinase inhibitors. MELJUSO stops proliferating and changes
151 morphology after about 4 days while SKMEL30 acquires a dark pigmentation before restoring growth.
152 Kinase activities were inferred from the levels of peptide phosphorylation at different time points and
153 compared to day 0 (summarised in Fig 3.A). A phylogenetic representation shows that these two cell
154 lines react similarly to the treatment only at early time points (Supp. Fig 3).

155 To perform pathway enrichment on a reduced set of proteins such as kinases, we used a network-
156 based approach and obtained coherent results for the two cell lines (Table 1). Indeed, pathways like
157 RIG-I or Toll-like receptor signaling (related to innate immunity and interferon responses) were
158 enriched at early time points for both SKMEL30 and MELJUSO. Among the enrichment results, RTK
159 pathways involving ErbB, neurotrophin and insulin appear (Fig 3.B, 3.C). Some pathways were
160 enriched before the increase in receptor activity reached the significance threshold and those were
161 therefore not represented on the phylogenetic tree (Supp. Fig 3). This signaling seems to persist after
162 the receptor resumes normal activity (Table 1). It has previously been shown that the inhibition of
163 ERK1/2 suppresses negative feedback on RTK expression, which can then be further activated to
164 compensate for this inhibition [22] (Fig 3 B, Supp. Fig 3). Coherent with the enriched pathways, we
165 observed in both cell lines a significant increase in the activity of RTKs such as HER3 and NTRK2 as well
166 as insulin-related receptors (INSR, IGF1R and IRR). Noteworthy, downstream insulin signaling was
167 enriched in the cytostatic MELJUSO only (detailed representation of pathways Supp. Fig 4-8). Other
168 RTKs previously related to resistance such ALK, AXL or c-MET displayed an increased activity (complete
169 list Supp. Fig 9) but those were not associated with enriched downstream signaling. Within the MAPK
170 pathway, the decrease in ERK5 (*MAPK7*) activity was partially relieved in SKMEL30 but not in MELJUSO
171 (Fig 3.B). Along these lines, Tubita et al recently showed that knock-down by shRNA or inhibition of
172 the kinase activity of ERK5 triggers senescence in melanoma [23].

173 Overall, the kinome data show the reactivation of ErbB, neurotrophin and insulin pathways and
174 enrichment of their downstream signaling. Interestingly, ERK5 activity was strongly reduced in the
175 cytostatic cell line MELJUSO (Fig 3.B).

176

177 **Contribution of miRNAs to the resistant phenotype**

178 To see if miRNAs could participate in the adaptation to treatment and the proliferative phenotypes,
179 we profiled the miRNome of all three cell lines by small RNA-seq at day 0 and 33. In line with their
180 phenotypes, IPC298 showed little deregulation of miRNAs compared to SKMEL30 and MELJUSO cell
181 lines (Supp Fig. 10). Next, we performed qCLASH analysis for the two proliferative cell lines IPC298
182 (early adaptation) and SKMEL30 (late adaptation) (summarised in Fig 4.A).

183 Although qCLASH-based miRNA interactomes do not provide a complete picture of all interactions,
184 PCA was able to discriminate between the different cell lines and conditions (Supp. Fig 11). Previous
185 studies reported a correlation between the number of detected hybrids and the expression levels of
186 its miRNA and mRNA components [14, 24]. These correlations hold true for our matching total and
187 the small RNA-seq data when taking the total count across the replicates (Fig 4.B, left panels).
188 Moreover, further summing up the hybrids for each miRNA or mRNA strengthens the correlation
189 between RNA-seq and qCLASH data, especially for miRNAs (Fig. 4. B, right panels). qCLASH data also
190 contain transient interactions, which are unlikely to be functionally relevant for the cell and technical
191 replicates are often used to further select most likely interactions. We explored how the detection of
192 interactions in one, two or three replicates depends on their expression level and observed that
193 interactions detected in triplicates were associated with a greater expression supporting the rationale
194 of using such thresholds (Supp. Fig 12). To further select the most relevant miRNAs, we constructed a
195 network with the interactions specific to the resistant phenotype. We first selected the interactions
196 detected in triplicates, then ensured that they were present in both resistant IPC298 and SKMEL30
197 but absent from their untreated counterparts (Fig 4.C). Finally, we overlaid the log fold changes from

198 the small and total RNA-seq for the corresponding miRNAs and mRNAs onto the resulting network
199 (Fig. 4.D). Based on those representations, we selected some interactions to confirm their
200 deregulation by qPCR. We investigated if those observations could be extended to two BRAF mutant
201 cell lines, A375 and 624Mel which underwent the same treatment and re-established growth (Supp.
202 Fig 13). Most of the selected interactions did not exert a robust inverse expression between miRNA
203 and mRNA (Supp. Fig 14,15). Among mRNAs, we observed a robust upregulation of CCND1 which is a
204 known resistance mechanism to CDK4/6i as well as a strong upregulation of IFN related gene IFI6
205 (Supp. Fig 13). Except for the amelanotic cell line A375, we observed the upregulation of LGALS3BP,
206 TXNIP and TYRP1 (Fig 4.E). Among miRNAs, mir-211-5p was upregulated in all proliferative cell lines
207 except the amelanotic A375, which is known not to express it (Fig 4.F) [25], and MELJUSO (Fig 4.G),
208 which has very low levels.

209 Overall, the number of interactions detected by qCLASH method is influenced by the expression level
210 of the corresponding miRNA and mRNA. Most of the detected interactions did not exert the expected
211 inverse expression pattern between miRNA and mRNA. miRNAs and mRNAs displayed a more robust
212 change in expression across cell lines. Except for the amelanotic A375, upregulation of miR-211-5p is
213 associated with resistant and proliferative cell lines.

214

215 **iCell integration of bulk and single-cell RNA-seq reveals perturbed pathways and predicts genes**
216 **facilitating senescence escape**

217 To gain further insights into NRAS mutant melanoma cells' adaptation to treatment, we integrated
218 the bulk RNA-sequencing data with previous condition-matching single-cell data from our lab by
219 adapting and applying a Non-negative Matrix Tri-Factorization (NMTF) approach called iCell [15]. We
220 used the iCell methodology because it is a versatile data fusion framework, which has previously been
221 used to perform integrative comparative analyses of disease and control tissue data, predicting new

222 cancer and COVID-19 related genes [15, 26] and suggesting potential drug re-purposing candidates
223 [26].

224 For each condition (treated cell line and time point), we constructed protein-protein interaction (PPI)
225 networks by overlaying the experimentally validated PPI network for *Homo Sapiens* from BioGRID [27]
226 with the condition-specific bulk RNA-sequencing data. Also, we derived a condition-specific co-
227 expression (COEXP) network from the corresponding bulk RNA-seq data (see Methods section). Next,
228 we applied Non-negative Matrix Tri-Factorization (NMTF) on the corresponding adjacency matrices of
229 the resulting PPI, COEXP and the single-cell expression data collectively, to ensure data fusion
230 (Methods and [15]). This resulted in the creation of nine condition-specific iCell networks, by
231 multiplying the G1 matrix resulting from the data fusion and its transpose (which is equivalent to
232 computing the dot product between gene pairs) and considering as interactions the 1% highest values
233 in each row and column (see the Methods and [15]).

234 As illustrated in Supp. Fig 16, resulting condition-specific iCell networks were investigated by first
235 comparing the global topology of all resulting iCell networks over all treated single-cell line conditions
236 over all time points. Then, these topological changes were further characterised by identifying the
237 genes that change their local topology between each pair of conditions, as well as the ones whose
238 local topology is conserved. We related the identified most rewired genes and the least rewired ones
239 to MSigDB hallmarks by performing an Over-Representation Analysis (ORA) (see Methods for details).
240 For each condition, we also clustered the genes based on the local topology in the corresponding
241 condition-specific iCell network and then found the MSigDB hallmarks that are enriched in the
242 resulting clusters. We focused on two senescence-escape related hallmark pathways to predict novel
243 genes potentially related to these pathways based on their appearance in the clusters that were
244 enriched across all conditions.

245 Then, we compared the overall topology of the iCell networks obtained for each condition by using
246 thus far the most sensitive measure of global network topology, the "Graphlet Correlation Distance"

247 (GCD-11) (see Methods and [28]). The lower the GCD-11 value, the closer the topologies of the
248 networks [28]. We used Ward's hierarchical clustering to cluster the resulting heatmap of the GCD-
249 11s between all iCell networks (all-to-all matrix). In line with our phenotypic observations, we showed
250 on the heatmap (Fig 5.A) that for the resistant cell line IPC298, the conditions D4 and D33 have the
251 lowest GCD-11 value (0.26) and hence clustered together, suggesting early adaptation to treatment
252 of this cell line. For the two other cell lines, conditions D0 and D4 grouped together (GCD-11 values of
253 0.71 for SKMEL30 and 0.87 for MELJUSO), suggesting that these two cell lines adapt later.

254 Next, the local topology of genes in the condition-specific iCell networks was analysed to find out if
255 some are rewired under specific biological conditions. To this end, when comparing two conditions,
256 we focused on genes that were expressed in both conditions (Venn diagrams in Fig. 5.B and supp. Fig.
257 17). Within each iCell network, the local topology around a gene in the network was quantified by
258 using it's "Graphlet Degree Vector" (GDV). We then measure the rewiring of a gene between two
259 conditions by comparing its GDVs in the two networks using "Graphlet Degree Vector Similarity"
260 (GDVS) (detailed in Methods and in [29]). Between two conditions, genes with high GDVSs have
261 conserved topologies and are called "stable", while the genes with low GDVSs are rewired and are
262 called "perturbed". We related the top 10% of the most "stable" and the top 10% of the most
263 "perturbed" genes to MSigDB hallmarks [30] by performing ORA. For each cell line, the condition-
264 specific iCell networks were compared for all time points together (i.e., D4 vs D0, D33 vs D4, and D33
265 vs D0). For all cell lines, we observed that the top 10% of the most "perturbed" genes were enriched
266 at different contrasts in "ADIPOGENESIS" (also observed in senescent fibroblasts [31]) and "OXIDATIVE
267 PHOSPHORYLATION" (OxPhos) (a pathway commonly dysregulated in senescence which has been
268 proposed as a targeting strategy [32]) (Fig 5.C). Then, the local topology of genes was compared
269 between the condition-specific iCell networks of different cell lines, but at matching time points (e.g.,
270 MELJUSO_D0 vs SKMEL30_D0). Interestingly, the top 10% of the most "stable" genes were only found
271 to be enriched when comparing IPC298 vs MELJUSO at day 0 and when comparing MELJUSO vs
272 SKMEL30 at day 4, which suggests that these cell lines react coherently early on and diverge later

273 (supp Fig. 17). At day 0, and across all pairwise comparisons involving IPC298 cell line, the top 10% of
274 the most "perturbed" genes were enriched for OxPhos, suggesting a different initial metabolic state
275 for IPC298. On day 4, when comparing IPC298 and SKMEL30 cells, the top 10% of the most "perturbed"
276 genes were enriched in "INTERFERON ALPHA/GAMMA RESPONSE". At days 4 and 33, but not across
277 all pairwise comparisons, we found that the top 10% of the most "perturbed" genes are enriched in
278 "EPITHELIAL MESENCHYMAL TRANSITION", "ADIPOGENESIS" and "COAGULATION". Further
279 information on the relevance of these enriched pathways can be found in the Discussion.

280 Finally, to predict novel genes which could contribute to senescence escape facilitated by interferons,
281 genes were clustered based on their GDVs signatures in the corresponding condition-specific iCell
282 network using "Ward's hierarchical clustering" and the "k-medoids" algorithms. For each condition,
283 we performed ORA to associate the clusters to hallmarks from MSigDB (results of ORA on the clusters
284 obtained by using k-medoids clustering in Fig 5.D). The results for the two algorithms showed limited
285 agreement (Fig 5.E, left), as measured by Adjusted Rand Index for each condition: 0.31, 0.38 and 0.30
286 for MELJUSO at day 0, day 4 and day33; 0.32, 0.30 and 0.26 for SKMEL30 at the same time points and
287 0.27, 0.31 and 0.45 for IPC298. Therefore, we considered the results from the two different clustering
288 methods (hierarchical and k-medoids) separately. Enriched clusters were filtered to exclude genes
289 that are already known to be associated with hallmarks in MSigDB. For the remaining genes, we
290 counted the number of times a gene was found in the clusters that are enriched in one of the two
291 senescence escape-related pathways, EMT and interferon gamma (see Fig 5.E right). Then, based on
292 the distributions of the number of times genes appeared in these enriched clusters, we predicted the
293 genes that appeared in two or more of these enriched clusters as related to senescence escape. To
294 obtain more robust predictions, we only considered genes to be involved senescence escape-related
295 by using both algorithms. This resulted in a set of 90 genes, some of which are known to interact with
296 TP53, further suggesting a connection to senescence escape (Fig. 5.F, Supp. Table 2).

297 To conclude, the integrated analysis of bulk and single-cell data by using the iCell methodology further
298 confirms our phenotypic observations and uncovers the most dysregulated processes ("OXIDATIVE
299 PHOSPHORYLATION", "ADIPOGENESIS", "COAGULATION" and "EPITHELIAL MESENCHYMAL
300 TRANSITION") during adaptation to the treatment. Furthermore, it allowed us to predict 90 new genes
301 involved in senescence escape.

302

303 **DISCUSSION**

304 Most cancer cells inevitably develop resistance to targeted therapies. Anticipating the development
305 of such resistance to a newly tested combination of CDK4/6i and MEKi, we characterised the
306 transcriptomic responses in 3 NRAS mutant melanoma cell lines over an extended treatment duration
307 of 33 days. Our RNA-seq data exhibited a strong enrichment in interferon responses, coherent with
308 previous observations by Goel et al. [33] following CDK4/6 inhibition. This study showed that CDK4/6
309 inhibitors downregulate E2F2 and DNMT1, subsequently leading to a hypomethylation of the genome
310 (Supp. Fig 18). The works of Chiappinelli et al [34] and Roulois et al [35] first showed that
311 hypomethylation brought about by DNMT inhibitors induce the expression of otherwise silenced
312 endogenous retroviruses (ERVs). These ERVs then form dsRNAs in the cytoplasm and trigger an anti-
313 viral immune response associated with interferon production. This phenomenon was termed "viral
314 mimicry" and has in the meantime been reported in different cancer types and in response to different
315 epigenetic perturbations (DNMTi, HDACi, HMTi). Brägelmann et al [36] also reported the activation of
316 viral mimicry in the case of BRAF mutant melanoma and MAPK inhibitors (BRAFi + MEKi) further
317 supporting the E2F2-DNMT1 axis as a mechanism of action. Melanoma cells are considered very
318 immunogenic [37] and this partially explains why melanoma respond better to immunotherapy than
319 other cancer types. IFN signaling is known to upregulate PD-L1, explaining why many treatments
320 activating viral mimicry have been shown to synergise with immune checkpoint inhibitors. Here, we
321 confirm the appearance of an IFN signature following CDK4/6 and MEK inhibition suggesting a
322 potential induction of viral mimicry.

323 A "senescence score" predicted from our data with SENESCopedia [18] suggested induction of a
324 senescent transcriptional programme in all cell lines. Cytokines composing the SASP can induce
325 features of EMT [38] and EMT has been recently proposed to inhibit senescence in HeLa cells treated
326 with Doxorubicin [39]. TIS and EMT share common transcription factors with opposite effects on both
327 processes (Supp Fig. 19) [40] and cancer cells escaping from TIS have been associated with a

328 mesenchymal phenotype [41]. IFN gamma, by promoting EMT [42, 43, 44], could further support
329 escape from senescence (Supp Fig. 20.A). To understand the relationship between IFN gamma and
330 EMT gene sets (from the hallmarks) and a recent gene set characterizing senescence in cancer cell
331 lines [45], we looked at changes in expression (log2 fold change) between those gene sets at day 14
332 where all cell lines display high senescence scores. IFN gamma shows an opposite trend in expression
333 to the EMT and senescence gene sets (Supp Fig. 20.B), suggesting that IFN may accelerate the EMT
334 process and thereby repress senescence. Albeit interferon signaling has earlier on been linked with
335 senescence [45], only later Katlinskaya and Yu et al. showed a role of IFNAR1 in the induction of
336 senescence [47]. Recently, the accumulation of double stranded RNA was proposed to also contribute
337 to the onset of senescence [48, 49]. These findings suggest a link between senescence and viral
338 mimicry, which can engage autocrine and paracrine secretion of interferons. We propose that the
339 induced IFN gamma programme may contribute to senescence escape by inducing EMT.

340 To identify targetable proteins, which could explain the senescent phenotype, we profiled the kinase
341 activities of SKMEL30 and MELJUSO cells upon CDK4/6 and MEK inhibition. We observed the
342 reactivation of different RTKs due to ERK1/2 inhibition as previously reported by others [50]. Some of
343 the corresponding pathways such as ErbB, neurotrophin and insulin were found enriched through
344 network-based enrichment hinting at an active downstream signalling. Interestingly, all those
345 pathways have been shown to activate ERK5. In breast cancer, ERK5 contributes to the response to
346 EGF stimulation [51] and is involved in the resistance to ErbB-2 (HER2) inhibitors by facilitating G1-S
347 transition [52]. In BRAF mutant melanoma resistant to BRAFi and MEKi, IGF1R activation induces ERK5
348 phosphorylation [53]. In senescent fibroblasts, BDNF-TrkB has been shown to activate ERK5 and was
349 proposed to form an autocrine loop further enhancing senescent cell viability [54]. ERK5 activation
350 has also been linked to PDGFR signalling in NRAS mutant melanoma treated with MEK and ERK1/2
351 inhibitors [55, 56] (Fig 3B, 3D, 3E). In other cell types, Src is also known to activate ERK5 and Focal
352 Adhesion Kinases (FAK1 and FAK2) [57, 58]. Other Src Family Kinases (SFKs) display an increased
353 activity (Supp. Fig 20) and have been previously linked with EMT [59]. Finally, IFN gamma was reported

354 to activate ERK5 and its activation is necessary for the full expression of interferon stimulated genes
355 [60]. Linking this observation with our RNA-seq data (Supp. Fig. 21) further supports the idea that IFN
356 gamma could facilitate senescence escape by activating ERK5.

357 Investigating the contribution of miRNAs to the establishment of resistance, we noticed the
358 upregulation of mir-211-5p in all proliferative cell lines but the amelanotic A375. Interestingly, miR-
359 211-5p is known to derive from the TRPM1 transcript and both are very lowly expressed in the
360 senescent cell line MELJUSO (supp Fig. 21). miR-211-5p inhibits DUSP6, which regulates ERK5 kinase
361 activity, and this axis has been shown to be relevant i*n vivo* in genetic variants of A375 overexpressing
362 mir-211 or DUSP6 and treated with BRAF/MEKi [61]. In qPCR validation experiments, mRNAs displayed
363 a more robust change in expression with LGALS3BP, TXNIP and TYRP1 being upregulated in four out
364 of five cell lines. LGALS3BP and TXNIP are interferon-inducible and interestingly, LGALS3BP has been
365 reported to promote EMT.

366 Integrating single-cell and bulk RNA-seq data, we observed the perturbation of OxPhos in all cell lines.
367 This is in line with previous works demonstrating metabolic adaptation after MAPK inhibition or
368 CDK4/6i in BRAF mutant and uveal melanoma [62, 63]. Moreover, OxPhos metabolism has been
369 previously reported as a generic drug resistance mechanism and as a key decision point between cell
370 death and survival [64, 65]. Upon comparison of different treatment time points, differences in
371 processes such as “ADIPOGENESIS” and “COAGULATION” were observed. Interestingly, those have
372 recently been associated with replicative senescence [38], cell cycle arrest caused by CDK4/6i [66] and
373 escape from OIS [67]. EMT has been reported to inhibit senescence [22, 44]. We therefore clustered
374 the genes in the networks and enriched those clusters to report novel associations between genes
375 and the processes of EMT and IFN gamma response, which could support senescence escape. Our
376 predicted genes are coherent with the results of a genetic screen aiming to identify genes contributing
377 to senescence bypass after p16 overexpression in melanoma [68]. Interestingly, the IFN-inducible
378 gene LGALS3BP, previously reported to contribute to EMT and identified in our miRNA resistant

379 network, was predicted by our approach to be associated with senescence escape. On the other hand,
380 TXNIP, another IFN-inducible gene from the miRNA network, recently shown to participate in the
381 induction of senescence upon IGF1 stimulation, was found associated only once and therefore not
382 selected [69]. This further suggests that our approach can relate genes to function beyond their
383 expression pattern, providing a list of 90 genes associated with senescence escape in cancer cells (Fig.
384 5.F).

385 Taken together, our data describe how NRAS mutant melanoma adapt to CDK4/6 and MEK inhibition
386 by triggering an EMT programme. This is reminiscent of the Neural Crest Stem Cell (NCSC)-like state
387 identified in single cell RNA-seq of patient samples after MAPKi by Rambow and colleagues [70]. This
388 state was later characterised by FAK-dependent AKT activation [71], associated with slow or no
389 proliferation and the expression of EMT-related transcription factors.

390 In sum, our work sheds new light on the intimate relationships between three interacting pathways,
391 senescence, interferon and insulin signalling, with the EMT process (Fig. 6). Our data suggest a new
392 role of interferon gamma, which, by triggering EMT, can facilitate senescence escape while insulin
393 signaling is associated with a robust cytostasis and senescent transcriptome.

394 ## Methods

395 ### Cell culture

396 NRAS-mutant MELJUSO, SKMEL30 and IPC298 (ACC-74, DSMZ; ACC-151, DSMZ; ACC-74, DSMZ) and
397 BRAF-mutant A375 and 624MEL (CRCL-1619, ATCC; kindly provided by Dr. Ruth Halaban, Yale School
398 of Medicine) melanoma cell lines were grown in RPMI-1640 medium supplemented with 10% heat-
399 inactivated fetal bovine serum, L-glutamine (2 mM), streptomycin (100 µg/mL) and penicillin (100
400 units/mL). The cells were kept at 37°C, in a humidified atmosphere with 5% CO2 and sub-cultivated
401 twice a week. Resistance of MELJUSO, SKMEL30, and IPC298 cells to the MEK and CDK4 inhibitors was
402 induced by treatment with 110nM, 35nM or 16nM of Binimetinib, respectively, and 1µM of Palbociclib
403 for 33 days.

404 ### Total RNAseq

405 Transcriptome sequencing was performed using total RNA. Libraries were prepared using "TruSeq
406 Stranded Total RNA Library Prep Gold" Kit (Illumina, USA) and sequenced as 2x75bp on a NextSeq 550
407 (Illumina, USA). The sequencing was carried out at Luxgen platform, LNS. Data were aligned to the
408 reference genome (hg38) using STAR (v 2.7.9a) and differential expression analysis was performed
409 using R (v 4.2.2) and DESeq2 (v 1.34.0). This analysis was automated in a snakemake workflow (v 0.3.2)
410 [72] (https://gitlab.lcsb.uni.lu/aurelien.ginolhac/snakemake-rna-seq) using docker file (v 0.6)
411 (https://hub.docker.com/r/ginolhac/snake-rna-seq/tags). Mixing all cell lines into one analysis
412 masked the differences of each time course. Therefore, a subset per cell line was created and the
413 differential gene expression was performed independently. To predict senescence scores with
414 SENESCopedia [18], data were reprocessed and aligned to GENCODE (v 34) using kallisto (v 0.46.2)
415 according to the recommendations of the authors.

416 ### Gene-list based pathway enrichment

417 Over-Representation Analysis (ORA) and Gene Set Enrichment Analysis (GSEA) were performed using
418 R (v 4.2.2) and the package “clusterProfiler” (v 4.0.5). The Hallmark Gene Set Collection from MSigDB
419 were used as reference. Differentially expressed genes used for GSEA were ranked according to the π
420 value, which takes into consideration both the statistical significance and the biological relevance
421 through the product of the p-value and the fold change [73]. The results were represented using the
422 package “pheatmap” (v 1.0.12) using the default “Ward.D2” clustering algorithm. ORA results were
423 displayed using the “ggplot2” (v 3.3.6) package.

424 **Kinase activity (PamGene)**

425 To assess the kinase activity within the NRAS mutant melanoma cell lines MELJUSO and SKMEL30 to a
426 combination of CDK4/6 and MEK inhibitors, cell samples were collected at day 0, 1, 4 and 33. Cell
427 pellets were lysed in Mper (78501, Thermo Fisher) supplemented with Halt Phosphatase Inhibitor
428 Cocktail (78428, Thermo Fisher) and Halt Protease Inhibitor Cocktail, EDTA free (78437, Thermo
429 Fisher), for 15 min on ice. The lysate was clarified (10000g, 15 min, 4°C) before aliquoting and freezing
430 at -80°C. Adopting a balanced design, three replicates for each condition and cell line were assessed
431 for both tyrosine kinase activity on PTK chips (86402, PamGene International B.V., 's-Hertogenbosch,
432 the Netherlands) and serine threonine kinase activity on STK chips (87102, PamGene International
433 B.V., 's-Hertogenbosch, the Netherlands) using the manufacturer's protocol. Each chip contains a
434 panel of 196 (PTK) and 144 (STK) phorylatable peptides. The phosphorylation of these peptides by
435 native kinases in the applied lysate was quantified by sequence agnostic fluorescently coupled anti
436 phosphorylation antibodies (Suppl. Fig.4). Image processing was achieved using the instrument
437 manufacturer’s Bionavigator software before applying COMBAT normalization and performing
438 Upstream Kinases Analysis (UKA) using a multiple hypothesis testing approach. This identified
439 responsible kinases for the observed phosphorylation status with a median final score for the
440 likelihood of the kinase being responsible for observed phosphorylation to which a cutoff of 1.2 was
441 applied and a median kinase statistic indicating the degree of and direction of kinase activity change

442 between compared conditions. The results were compiled to construct representative kinome trees
443 with an adaptation of the CORAL tool [74] in R (v 4.2.0).

444 **Network-based pathway enrichment**

445 To identify biological pathways enriched in a protein list, we applied a network-based protein set
446 enrichment analysis approach using EnrichNet [75]. The inputs are a list of the PamGene protein
447 identifiers and the database of interest from which reference protein sets will be extracted. The
448 databases include (KEGG, BioCarta, WikiPathways, Reactome, PID, and GO. Using a genome-scale
449 molecular interaction network, we map the target and reference datasets and then perform a network
450 analysis, which involves two steps: i) the use of a random walk with restart (RWR) algorithm to score
451 the distance between the mapped target protein set and reference datasets in the network. ii) the
452 comparison of the calculated scores against a background model. Extensive information on how the
453 RWR method for node relevance scoring was developed is found in [75]. A network similarity score
454 (XD-score) measures how close the protein set of the PamGene data is to the pathways in the
455 databases. The XD score is compared to a classical enrichment analysis score (p-values) which measure
456 the significance of the overlap between pathways and the protein set.
457 A similarity ranking table of the reference datasets is generated, including their network-based
458 association scores (measured using the XD-score). The table ranks the pathways from a chosen
459 database to the protein set of the PamGene data. Using an interactive graph-based visualization, we
460 generate interoperable interaction networks for each pathway. This network (XML-based) highlights
461 the proteins that overlap in pathways, illustrating their interactions.

462 **Small RNAseq**

463 Small RNAseq was performed on the same samples used for total RNAseq. Libraries were prepared
464 using "QIASeq miRNA Library kit" (Qiagen, Germany) and sequenced as 2x75bp on a NextSeq 550
465 (Illumina, USA). The sequencing was carried out at Luxgen platform, LNS. Data were aligned to the
466 miRBase (v 2.2.2.1) and piRBase (regulatoryrna.org, v 2.0) using bowtie2 (v 2.3.4.1) and differential

467 expression analysis was performed using R (v 4.2.2) and DESeq2 (v 1.34.0). This analysis was
468 performed using a snakemake workflow adapted from a previous workflow designed by
469 https://github.com/jounikuj/ for this library preparation. Briefly, the snakemake workflow applies 4
470 passes of trimming (including UMIs) and map the obtained reads on miRBase using bowtie2 with the
471 parameter –very-sensitive-local. Next, the corresponding un-mapped reads are aligned to piRBase and
472 the successfully mapped read coming from these 2 passes of alignment are merged in a unique BAM
473 file per sample. Finally reads are counted, after UMI collapsing (UMI_tools v. 1.0.0) using a
474 combination of samtools (v 1.9) and bash commands.

475 **qCLASH**

476 qCLASH sample preparations were performed exactly as previously described by Kozar *et al.* [16]
477 Briefly, 50 million cells were UV cross-linked at a wavelength of 250nm and 600J/cm2. AGO protein
478 immunoprecipitation was performed using Protein G Dynabeads (Invitrogen), and 10µl 2A8 anti-Ago
479 antibody (Millipore) per sample. qCLASH libraries were sequenced on a NextSeq500 instrument with
480 a read length of 85bp. The raw sequences were pre-processed and analyzed as previously described
481 [16] using the bioinformatics pipeline *hyb* [76], and custom scripts available at GitHub
482 (https://github.com/RenneLab/qCLASH-Analysis).

483 **miRNA network construction and representation**

484 qCLASH data were analysed using R (v 4.2.2) and the "tidyverse" package. Interaction lists were
485 converted to "igraph" objects with the corresponding package (v 1.3.4) and further exported to
486 cytoscape using "RCy3" (v 2.12.4). Final representations were made using Cytoscape (v 3.8.2) and the
487 plugin "Legend Creator" (v 1.1.6).

488 **RT-qPCR**

489 RNA was extracted from cell lysates using the Quick-RNA MiniPrep kit with on-column DNase I
490 treatment (Zymo Research, USA) according to the mnufacturer's protocol. RNA purity and quality were

491 assessed using the NanoDrop2000 Spectrophotometer (Thermo Scientific, USA). 500ng of RNA were
492 used to perform reverse transcription using the miScript RT II Kit and HiFlex Buffer Reverse
493 Transcription (Qiagen, Netherlands). Quantitative polymerase chain reaction (qPCR) was performed
494 using the CFX384 Detection System (BioRad, USA) using 5ng and 50ng of cDNA as a template for
495 subsequent miRNA and mRNA expression detection, respectively. Primers were purchased from
496 Qiagen (miScript Primer Assay range) and from Eurogentec (primer list Supp. Table 4) to respectively
497 amplify miRNA and mRNA. Amplification curves were analyzed using CFX software (BioRad, USA) and
498 expression was normalised using three housekeeping genes (RNU1A, RNU5A, SCARNA17 for miRNA
499 and HPRT, PPIA, TBP for mRNA).

500 **Single cell RNA-seq analysis**

501 Single cell RNA-seq data from [Randic et al, in revision] were reprocessed using Seurat (v 4.2.0) and
502 SeuratObject (v 4.1.2). Reads were aligned to human genome hg38 using STAR aligner. Transcripts
503 were filtered to be detected in at least 3 cells and to totalise at least 100 counts across cells. Cells were
504 filtered based on mitochondrial transcripts (<=25%), ribosomal transcripts (<= 1%), and a cell
505 complexity (log10GenesPerUMI >=80%). Thresholds for Unique Molecular Identifiers (UMI), genes
506 detected were different between cells lines (for MELJUSO and SKMEL30: 150 and 100, for IPC298: 350
507 and 150). Finally, mitochondrial, ribosomal and hemoglobin genes were removed, and genes were
508 filtered to have at least 10 counts across the filtered cells.

509 **iCell data-fusion framework**

510 iCell methodology [15] was applied separately to each of the three cell lines (MELJUSO, SKMEL30 and
511 IPC298) at day 0, day 4 and day 33, to obtain integrated networks that encompass the condition-
512 specific (i.e., defined by a cell line and day) PPI, COEX, and single-cell RNA-seq data from our lab
513 [Randic et al, unpublished]. We used the iCell methodology because it is an intermediate data
514 integration method that uses Non-negative Matrix Tri-factorization (NMTF) to simultaneously
515 decompose multiple relational matrices through the inference of a single joint model [15, 77].

516 Therefore, it does not suffer from information loss of early integration approaches that combine all
517 datasets into a single dataset before integration, or late integration methods that first build models
518 for each dataset and then combine them into an integrated model. Additionally, NMTF-based
519 methods are co-clustering methods that encode the high-dimensional input data into three low-
520 dimensional matrix factors [78]. The clustering information is contained in the so-called cluster
521 indicator matrices that are easily interpretable (unlike the resulting matrices of other artificial
522 intelligence algorithms), making them ideal for mining biological data.

523 For each condition (treated cell lines and time points), we constructed condition-specific Protein-
524 Protein Interaction (PPI) and gene co-expression (COEXP) networks as follows. We collected the
525 experimentally validated protein-protein interactions of *Homo sapiens* from BioGRID (v 4.3.195) [32],
526 from which we excluded genes (nodes in the network) that are not expressed in our condition-specific
527 bulk RNA-seq data (zFPKM < −3, [79]). To generate the condition-specific COEXP networks, we applied
528 Spearman's correlation between the gene expression profiles from the condition-specific bulk RNA-
529 seq data, using a 0.9 correlation threshold with a *p-value ≤ 0.01*. These two condition-specific
530 networks were further filtered to exclude genes (nodes in the networks) that are not expressed in any
531 single cell according to the corresponding condition-specific single cell RNA-seq data.

532 For each condition, we followed the iCell methodology [15] to integrate the condition-specific PPI,
533 COEXP, and single-cell expression data together. To this aim, we used Non-negative Matrix Tri-
534 Factorization to simultaneously decompose the adjacency matrices of the PPI and COEXP networks,
535 A_1 and A_2, respectively, and the single cell RNA-seq expression data, *E*. More precisely, the two
536 adjacency matrices, A_1 and A_2, are simultaneously decomposed as the products of three matrix
537 factors each, A_1 as the product of matrix factors G_1, S_1 and G_1^T, and A_2 as the product of matrix factors
538 G_1, S_2 and G_1^T, i.e.: $A_1 \approx G_1 S_1 G_1^T$ and $A_2 \approx G_1 S_2 G_1^T$, where G_1 is interpreted as the cluster indicator
539 matrix of the genes and matrices S_1 and S_2 are interpreted as the compressed representations of the
540 PPI and COEXP networks, respectively. The condition-specific single-cell RNA-seq expression matrix,

541 E, is decomposed into the product of three matrix factors G_1, S_3 and G_2^T as: $E \approx G_1 S_3 G_2^T$, where S_3 is
542 interpreted as the compressed representation of the single-cell expression data, G_2 is the cluster
543 indicator matrix of single cells, and G_1 is the cluster indicator matrix of the genes that is shared across
544 the decompositions of all input matrices, which facilitates the information flow and allows for learning
545 from all data.

546 Furthermore, to ease interpretability, we constrain all matrix factors to be non-negative. We also
547 impose orthogonality constraint to the G_2 matrix factor to obtain less ambiguous functional
548 organization captured by the clusters [78].

549 This decomposition is done by minimizing the following objective function, *F*:

550 $$\min_{G_1,G_2,S_1,S_2,S_3 \geq 0} F(G_1, G_2, S_1, S_2, S_3) = \min_{G_1,G_2,S_1,S_2,S_3 \geq 0} \left[\sum_{i=1}^{2} \|A_i - G_1 S_i G_1^T\|_F^2 + \|E - G_1 S_3 G_2^T\|_F^2 \right], G_2\, G_2^T = I,$$

551 where $\| \ \|_F$ denotes the Frobenius norm and I is the identity matrix.

552 Because minimizing this objective function is an NP-hard continuous optimization problem [80], we
553 heuristically solve it by using a fixed point method that, starting from an initial solution, iteratively
554 applies multiplicative update rules [78] to converge towards a locally optimal solution (described in
555 the next section).

556 After minimizing *F*, we used the obtained matrix factors to create an integrated network that
557 encompasses the condition-specific PPI, COEXP, and single cell RNA-seq data, which we call iCell
558 network. Following the iCell methodology [15], we created this network by computing $G_1 \cdot G_1^T$ and
559 thresholding the resulting matrix to preserve only the top 1% of the strongest relationships in each
560 row and column.

561 We apply this methodology for each condition separately, resulting in nine condition-specific iCell
562 networks.

563 **Fixed point solver**

Following the iCell methodology [15], first we derive the Karush-Kuhn-Tucker (KKT) conditions, which are necessary for a solution to be optimal [80]:

$$\frac{\partial F}{\partial G_1} = \sum_{i=1}^{2}\left(-A_i^T G_1 S_i + A_i G_1 S_i^T + G_1 S_i G_1^T G_1 S_i^T + G_1 S_i^T G_1^T G_1 S_i\right) - E G_2 S_3^T + G_1 S_3 G_2^T G_2 S_3^T - \eta_1 = 0,$$

$$\frac{\partial F}{\partial G_2} = -E^T G_1 S_3 + G_2 S_3^T G_1^T G_1 S_3 - \eta_2 = 0,$$

$$\frac{\partial F}{\partial S_1} = -G_1^T A_1 G_1 + G_1^T G_1 S_1 G_1^T G_1 = 0,$$

$$\frac{\partial F}{\partial S_2} = -G_1^T A_2 G_1 + G_1^T G_1 S_2 G_1^T G_1 = 0,$$

$$\frac{\partial F}{\partial S_3} = -G_1^T E G_2 + G_1^T G_1 S_3 G_2^T G_2 = 0,$$

$$\eta_1, \eta_2, G_1, G_2 \geq 0,$$

$$\eta_1 \odot G_1 = 0,$$

$$\eta_2 \odot G_2 = 0,$$

$$G_2 G_2^T = I,$$

where $\odot$ is the Hadamard (elementwise) product, I is the identity matrix, and matrices, η_1 and η_2, are the dual variables for the primal constraints $G_1 \geq 0$ and $G_2 \geq 0$, respectively.

Then, we derive the following multiplicative update rules for all matrix factors, G_1, G_2, S_1, S_2 and S_3, to solve the KKT conditions presented above:

$$G_1 = G_1 \sqrt{\frac{\sum_{i=1}^{2}(A_i G_1 S_i^T) + E G_2 S_3^T}{\sum_{i=1}^{2}(G_1 S_i G_1^T G_1 S_i^T) + G_1 G_1^T E G_2 S_3^T}},$$

$$G_2 = G_2 \sqrt{\frac{E^T G_1 S_3}{G_2 G_2^T E^T G_1 S_3}},$$

$$S_1 = S_1 \sqrt{\frac{G_1^T A_1 G_1}{G_1^T G_1 S_1 G_1^T G_1}},$$

$$S_2 = S_2 \sqrt{\frac{G_1^T A_2 G_1}{G_1^T G_1 S_2 G_1^T G_1}},$$

$$S_3 = S_3 \sqrt{\frac{G_1^T E G_2}{G_1^T G_1 S_3 G_2^T G_2}}.$$

In our fixed point approach, we start from initial solutions of the matrix factors, which we compute using singular value decomposition (SVD) of the original input matrices [81], and iteratively use the derived update rules to compute new matrix factors, G_1, G_2, S_1, S_2 and S_3, until convergence. Initializing the matrix factors with SVD reduces the number of iterations that are needed to achieve convergence and makes our solver deterministic [81]. To satisfy the non-negativity constraint of NMTF, we generate the initial solutions by taking the absolute values of the entries from the matrices computed using SVD.

The iterative process ends when the objective function does not decrease anymore, which we measure every ten iterations with: $\left|\frac{F^{-1}-F^0}{F^0}\right| \leq 10^{-3}$, where F^0 is the value of the objective function at the current iteration, *i*, and F^{-1} is the value computed at iteration *i-10*.

Analyzing the topology of iCells

To mine the biological knowledge hidden in the iCell networks, we applied graphlet-based methods because they are the most sensitive measures of network topology to date [28, 34]. Graphlets are small, connected, nonisomorphic, induced subgraphs of a large network that appear at any frequencies in the network [82]. Within a graphlet, the symmetries between groups of nodes are called automorphism orbits and are used to characterise the different topological positions that a node participates in [82]. These orbits are used to generalised the notion of the node degree (the number of edges that the node touches in the network): for each orbit, the "graphlet degree of the

node" in the network is the number of times the node touches (is found at the position of) the particular orbit [28]. Following the methodology of Yaveroğlu *et al*. (2014), we characterised the topology of each node in a network by using the 11 nonredundant orbits of 2- to 4-node graphlets. Therefore, the topology of every node is captured by an 11-dimensional vector called "Graphlet Degree Vector" (GDV).

We compared the global topological dissimilarity between two condition-specific iCell networks by using "Graphlet Correlation Distance" (GCD-11), because it is the most sensitive network distance measure [28]. To do this, first we characterised the global topology of a network with its "Graphlet Correlation Matrix" (GCM), which is an 11×11 symmetric matrix that contains the Spearman's correlations between GDVs over all nodes of the network. Then, the GCD-11 between two networks is the Euclidean distance between the upper triangle values of their GCMs. The lower the GCD-11 value, the closer the topologies of the networks [28].

Additionally, we measure the change in the wiring of a gene between two condition-specific iCell networks by using the "Graphlet Degree Vector Similarity" (GDVS) between the GDVs of the node in the two networks, which is computed as follows. Given the GDV vector of a gene (node) in one network, $\boldsymbol{a}$, and the GDV vector of the same gene (node) in another network, $\boldsymbol{b}$, the distance between the ith coordinates of vectors $\boldsymbol{a}$ and $\boldsymbol{b}$ is defined as:

$$D_i(\boldsymbol{a}, \boldsymbol{b}) = w_i \frac{|log(\boldsymbol{a}_i + 1) - log(\boldsymbol{b}_i + 1)|}{log(max\{\boldsymbol{a}_i, \boldsymbol{b}_i\} + 2)},$$

where w_i is the weight of orbit i that accounts for dependencies between the orbits [29]. Then, GDVS between vectors $\boldsymbol{a}$ and $\boldsymbol{b}$ is defined as:

$$GDVS\ (\boldsymbol{a}, \boldsymbol{b}) = 1 - \frac{\sum_{i=1}^{11} D_i(\boldsymbol{a}, \boldsymbol{b})}{\sum_{i=1}^{11} w_i}.$$

GDVS is the similarity measure in (0,1] range, such that the similarity equal to 1 means that the two GDV vectors are identical, and thus, that the gene has the same local topology in both networks. We

625 use GDVS to identify the genes whose topology changed between two condition-specific iCell
626 networks, which we termed "perturbed" (i.e., whose GDVSs were close to 0), as well as the genes
627 whose local topology did not change, which we termed "stable" (i.e., whose GDVSs were close to 1).
628 These comparisons were made between different time points for the same cell line, as well as between
629 different cell lines for the same time point.

630 **Clustering**

631 For each cell line and each time point, we performed clustering of the Graphlet Degree Vectors (GDVs).
632 Prior to clustering, the features were weighted by using previously defined weights [29] and then log-
633 transformed. In addition, both the NMTF and GCM matrices were scaled to a 0 mean and unit variance.
634 For each input matrix, we first computed the Hopkins statistics to estimate cluster tendency. Then, to
635 identify the numbers of clusters, we estimate the cluster validity of potential solutions reporting
636 between 50 and 150 clusters, using 21 different metrics. We rank all clustering solutions for each
637 metric. Then, for each input matrix, the number of clusters is selected based on the solution associated
638 with the minimal median rank across all 21 metrics. We then performed hierarchical and k-medoids
639 clustering using a Pearson correlation-based distance and validated the obtained repartitions using
640 silhouette width and the between/within average distance ratio. All scripts are available on the
641 associated Git repository.

642 **Network representation of gene predictions**

643 Protein-Protein interactions between TP53, a known regulator of senescence, and genes associated
644 with "EMT" and "INTERFERON GAMMA RESPONSE" which have been linked with senescence escape
645 were extracted from BioGRID (v 4.4.217). A network representation was created by using Cytoscape
646 (v 3.9.1). The representation was further refined by using stringApp (v 2.0.0) and clusterMaker2 app
647 (v 2.3.2) and modified by using Inkscape (v 1.2.1).
648

Availability of data and materials

Raw data together with processed files were deposited to : PRJEB59603. Code to reproduce the results in this manuscript are available via GitLab repository (https://gitlab.com/Ahmed7emdan/integrative-multi-omics-analysishttps://github.com/).

Funding

VG is supported by the Luxembourg National Research Fond (FNR) PRIDE DTU CanBIO [grant reference: 21/16763386]. TR is supported by the FNR PRIDE DTU CriTiCS [grant reference: 10907093]. Project-related work performed by VG, HH, CM, DP, MTN, MB, AG, FT and SK were also supported by the University of Luxembourg and the Fondation Cancer, Luxembourg (grant "SecMelPro"). KM and NP are supported by funding from the European Union's EU Framework Programme for Research and Innovation Horizon 2020, Innovative Training Networks (MSCA-ITN-2019), funded under EXCELLENT SCIENCE - Marie Skłodowska-Curie Actions, Grant Agreement No 860895. KM, NMD, GC and NP are supported by funding from the European Research Council (ERC) Consolidator Grant 770827. NP is also supported by funding from the Spanish State Research Agency AEI 10.13039/501100011033 grant number PID2019-105500GB-I00.

Authors' contributions

SK conceived the study. SK, FT, DP, MT, TR and VG contributed to the experimental design. VG, FT, and DP acquired total RNA-seq and small RNA-seq data and AM, AG and VG processed, analysed and interpreted the data. TR, DP and CM acquired PamGene data, JL processed the data and performed Upstream Kinase Analysis. MO and AH performed network-based pathway enrichment and created xml models to overlay the inferred kinase activities; VG and CA interpreted the results. IK and HH performed qCLASH method, IK processed the data and AG, VG and HH analysed the hybrids and constructed the miRNA network. HH performed qPCR validations. MB processed the scRNA-seq data. NP, NMD, GC and KM conceived the data integration. KM, GC, and VG performed it and analysed the

673 results under the supervision of NMD and NP. LT performed the gene clustering; AB, MB, and VG
674 analyzed the gene clusters. VG, HH, AH, CA, AB and FT contributed to the figures. VG and SK drafted
675 the manuscript with input from all authors. NP, NMD and MO reviewed the manuscript. All authors
676 read and approved the final manuscript.

677 **Acknowledgements**

678 The authors want to thank L. Sinkonnen for his suggestions regarding the qCLASH method and its
679 extended applications, J.P. Wroblewska for her feedback and her insights regarding the biology of
680 amelanotic melanoma, A. Ginolhac for his help in the analysis of our RNA-seq data and his tips
681 regarding R language. Several *in silico* experiments presented in this paper were carried out using the
682 HPC facilities of the University of Luxembourg, Varrette et al. 2022, https://hpc.uni.lu.

683

684 **References**

685 [1] Hayflick, L., & Moorhead, P. S. (1961). The serial cultivation of human diploid cell strains.
686 *Experimental cell research*, *25*(3), 585-621.

687 [2] Kumari, R., & Jat, P. (2021). Mechanisms of cellular senescence: cell cycle arrest and senescence
688 associated secretory phenotype. *Frontiers in cell and developmental biology*, *9*, 645593.

689 [3] Ou, H. L., Hoffmann, R., González-López, C., Doherty, G. J., Korkola, J. E., & Muñoz-Espín, D. (2021).
690 Cellular senescence in cancer: From mechanisms to detection. *Molecular Oncology*, *15*(10), 2634-
691 2671.

692 [4] Liao, C., Xiao, Y., & Liu, L. (2020). The dynamic process and its dual effects on tumors of therapy-
693 induced senescence. *Cancer Management and Research*, *12*, 13553.

694 [5] Wang, L., Lankhorst, L., & Bernards, R. (2022). Exploiting senescence for the treatment of cancer.
695 *Nature Reviews Cancer*, *22*(6), 340-355.

696 [6] Campisi, Judith. "Aging, cellular senescence, and cancer." *Annual review of physiology* 75 (2013):
697 685.

698 [7] Campisi, Judith, and Ladislas Robert. "Cell senescence: role in aging and age-related diseases."
699 *Aging* 39 (2014): 45-61.

700 [8] Zhu, H., Blake, S., Kusuma, F. K., Pearson, R. B., Kang, J., & Chan, K. T. (2020). Oncogene-induced
701 senescence: From biology to therapy. *Mechanisms of ageing and development*, *187*, 111229.

702 [9] Prieur, A., & Peeper, D. S. (2008). Cellular senescence in vivo: a barrier to tumorigenesis. *Current*
703 *opinion in cell biology*, *20*(2), 150-155.

704 [10] Roger, L., Tomas, F., & Gire, V. (2021). Mechanisms and regulation of cellular senescence.
705 *International Journal of Molecular Sciences*, *22*(23), 13173.

706 [11] Caksa, Signe, Usman Baqai, and Andrew E. Aplin. "The future of targeted kinase inhibitors in
707 melanoma." *Pharmacology & Therapeutics* (2022): 108200.

708 [12] Naeli, Parisa, et al. "The intricate balance between microRNA-induced mRNA decay and
709 translational repression." *The FEBS Journal* (2022).

710 [13] Bartel, D. P. (2018). Metazoan micrornas. *Cell*, *173*(1), 20-51.

711 [14] Kozar, I., Philippidou, D., Margue, C., Gay, L. A., Renne, R., & Kreis, S. (2021). Cross-linking ligation
712 and sequencing of hybrids (qCLASH) reveals an unpredicted miRNA Targetome in melanoma cells.
713 *Cancers*, *13*(5), 1096.

714 [15] Malod-Dognin, Noël, et al. "Towards a data-integrated cell." *Nature Communications* 10.1 (2019):
715 1-13.

716 [16] Klein, M. E., Kovatcheva, M., Davis, L. E., Tap, W. D., & Koff, A. (2018). CDK4/6 inhibitors: the
717 mechanism of action may not be as simple as once thought. *Cancer cell*, *34*(1), 9-20.

718 [17] Goel, S., Bergholz, J. S., & Zhao, J. J. (2022). Targeting CDK4 and CDK6 in cancer. *Nature Reviews*
719 *Cancer*, *22*(6), 356-372.

720 [18] Jochems, F., Thijssen, B., De Conti, G., Jansen, R., Pogacar, Z., Groot, K., ... & Bernards, R. (2021).
721 The Cancer SENESCopedia: A delineation of cancer cell senescence. *Cell reports*, *36*(4), 109441.

722 [19] Laberge, Remi-Martin, et al. "Epithelial-mesenchymal transition induced by senescent
723 fibroblasts." *Cancer Microenvironment* 5 (2012): 39-44.

724 [20] Tato-Costa, Joana, et al. "Therapy-induced cellular senescence induces epithelial-to-
725 mesenchymal transition and increases invasiveness in rectal cancer." *Clinical colorectal cancer* 15.2
726 (2016): 170-178.

727 [21] Morales-Valencia, Jorge, et al. "Lipocalin 2 dictates cancer cell plasticity elicited by therapy-
728 induced senescence." *bioRxiv* (2022): 2022-03.

729 [22] Rosell, R., Karachaliou, N., Morales-Espinosa, D., Costa, C., Molina, M. A., Sansano, I., ... & Bueno,
730 A. M. (2013). Adaptive resistance to targeted therapies in cancer. *Translational lung cancer research*,
731 *2*(3), 152.

732 [23] Tubita, A., Lombardi, Z., Tusa, I., Lazzeretti, A., Sgrignani, G., Papini, D., ... & Rovida, E. (2021).
733 Inhibition of ERK5 elicits cellular senescence in melanoma via the cyclin-dependent kinase inhibitor
734 p21. *Cancer Res*.

735 [24] Fields, C. J., Li, L., Hiers, N. M., Li, T., Sheng, P., Huda, T., ... & Xie, M. (2021). Sequencing of
736 Argonaute-bound microRNA/mRNA hybrids reveals regulation of the unfolded protein response by
737 microRNA-320a. *PLoS genetics*, *17*(12), e1009934.

738 [25] Margue, Christiane, et al. "New target genes of MITF-induced microRNA-211 contribute to
739 melanoma cell invasion." *PloS one* 8.9 (2013): e73473.

[26] Xenos, A., Malod-Dognin, N., Zambrana, C., & Pržulj, N. (2023). Integrated Data Analysis Uncovers New COVID-19 Related Genes and Potential Drug Re-Purposing Candidates. *International Journal of Molecular Sciences*, 24(2), 1431.

[27] Oughtred, R. et al. (2019). The biogrid interaction database: 2019 update. *Nucleic Acids Research*, 47(D1), D529–D541.

[28] Yaveroğlu, Ömer Nebil, et al. "Revealing the hidden language of complex networks." Scientific reports 4.1 (2014): 1-9.

[29] Milenković, Tijana, and Nataša Pržulj. "Uncovering biological network function via graphlet degree signatures." *Cancer Informatics* 6 (2008): CIN-S680.

[30] Arthur, Liberzon, et al. "The molecular signatures database hallmark gene set collection." *Cell Syst* 1 (2015): 417-425.

[31] Chan, Michelle, et al. "Novel insights from a multiomics dissection of the Hayflick limit." *Elife* 11 (2022): e70283.

[32] Lee, Yun Haeng, et al. "Targeting mitochondrial metabolism as a strategy to treat senescence." *Cells* 10.11 (2021): 3003.

[33] Goel, S., DeCristo, M. J., Watt, A. C., BrinJones, H., Sceneay, J., Li, B. B., ... & Zhao, J. J. (2017). CDK4/6 inhibition triggers anti-tumour immunity. *Nature*, *548*(7668), 471-475.

[34] Chiappinelli, K. B., Strissel, P. L., Desrichard, A., Li, H., Henke, C., Akman, B., ... & Strick, R. (2015). Inhibiting DNA methylation causes an interferon response in cancer via dsRNA including endogenous retroviruses. *Cell*, *162*(5), 974-986.

[35] Roulois, D., Yau, H. L., Singhania, R., Wang, Y., Danesh, A., Shen, S. Y., ... & De Carvalho, D. D. (2015). DNA-demethylating agents target colorectal cancer cells by inducing viral mimicry by endogenous transcripts. *Cell*, *162*(5), 961-973.

763 [36] Brägelmann, J., Lorenz, C., Borchmann, S., Nishii, K., Wegner, J., Meder, L., ... & Sos, M. L. (2021).
764 MAPK-pathway inhibition mediates inflammatory reprogramming and sensitizes tumors to targeted
765 activation of innate immunity sensor RIG-I. *Nature communications*, *12*(1), 1-15.

766 [37] Huang, Alexander C., and Roberta Zappasodi. "A decade of checkpoint blockade immunotherapy
767 in melanoma: understanding the molecular basis for immune sensitivity and resistance." *Nature*
768 *immunology* 23.5 (2022): 660-670.

769 [38] Takasugi, M., Yoshida, Y., Hara, E., & Ohtani, N. (2022). The role of cellular senescence and SASP
770 in tumour microenvironment. *The FEBS Journal*.

771 [39] Hu, Xuerui, and Hongqi Zhang. "Doxorubicin-induced cancer cell senescence shows a time delay
772 effect and is inhibited by epithelial-mesenchymal transition (EMT)." *Medical science monitor:*
773 *international medical journal of experimental and clinical research* 25 (2019): 3617.

774 [40] Faheem, M. M., Seligson, N. D., Ahmad, S. M., Rasool, R. U., Gandhi, S. G., Bhagat, M., & Goswami,
775 A. (2020). Convergence of therapy-induced senescence (TIS) and EMT in multistep carcinogenesis:
776 current opinions and emerging perspectives. *Cell death discovery*, *6*(1), 1-12.

777 [41] De Blander, Hadrien, et al. "Cellular plasticity: a route to senescence exit and tumorigenesis."
778 *Cancers* 13.18 (2021): 4561.

779 [42] Imai, D., Yoshizumi, T., Okano, S., Itoh, S., Ikegami, T., Harada, N., ... & Maehara, Y. (2019). IFN-γ
780 promotes epithelial-mesenchymal transition and the expression of PD-L1 in pancreatic cancer. *Journal*
781 *of Surgical Research*, *240*, 115-123.

782 [43] Lo, U. G., Bao, J., Cen, J., Yeh, H. C., Luo, J., Tan, W., & Hsieh, J. T. (2019). Interferon-induced IFIT5
783 promotes epithelial-to-mesenchymal transition leading to renal cancer invasion. *American journal of*
784 *clinical and experimental urology*, *7*(1), 31.

785 [44] Lee, M., Kim, D. W., Khalmuratova, R., Shin, S. H., Kim, Y. M., Han, D. H., ... & Shin, H. W. (2019).
786 The IFN-γ–p38, ERK kinase axis exacerbates neutrophilic chronic rhinosinusitis by inducing the
787 epithelial-to-mesenchymal transition. *Mucosal Immunology*, *12*(3), 601-611.

788 [45] Saul, Dominik, et al. "A new gene set identifies senescent cells and predicts senescence-associated
789 pathways across tissues." *Nature communications* 13.1 (2022): 1-15.

790 [45] Fridman, A. L., & Tainsky, M. A. (2008). Critical pathways in cellular senescence and
791 immortalization revealed by gene expression profiling. *Oncogene*, *27*(46), 5975-5987.

792 [47] Katlinskaya, Y. V., Katlinski, K. V., Yu, Q., Ortiz, A., Beiting, D. P., Brice, A., ... & Fuchs, S. Y. (2016).
793 Suppression of type I interferon signaling overcomes oncogene-induced senescence and mediates
794 melanoma development and progression. *Cell reports*, *15*(1), 171-180.

795 [48] Mullani, N., Porozhan, Y., Mangelinck, A., Rachez, C., Costallat, M., Batsche, E., ... & Muchardt, C.
796 (2021). Reduced RNA turnover as a driver of cellular senescence. *Life science alliance*, *4*(3).

797 [49] Harries, L. W. (2022). Dysregulated RNA processing and metabolism: a new hallmark of ageing
798 and provocation for cellular senescence. *The FEBS Journal*.

799 [50] Chen, C. H., Hsia, T. C., Yeh, M. H., Chen, T. W., Chen, Y. J., Chen, J. T., ... & Huang, W. C. (2017).
800 MEK inhibitors induce Akt activation and drug resistance by suppressing negative feedback ERK-
801 mediated HER2 phosphorylation at Thr701. *Molecular oncology*, *11*(9), 1273-1287.

802 [51] Ortega-Muelas, M., Roche, O., Fernández-Aroca, D. M., Encinar, J. A., Albandea-Rodríguez, D.,
803 Arconada-Luque, E., ... & Sánchez-Prieto, R. (2021). ERK5 signalling pathway is a novel target of
804 sorafenib: Implication in EGF biology. *Journal of cellular and molecular medicine*, *25*(22), 10591-10603.

805 [52] Zhang, J., Pearson, A. J., Sabherwal, N., Telfer, B. A., Ali, N., Kan, K., ... & Tournier, C. (2022).
806 Inhibiting ERK5 overcomes breast cancer resistance to anti-HER2 therapy by targeting the G1–S cell-
807 cycle transition. *Cancer Research Communications*, *2*(3), 131-145.

808 [53] Benito-Jardón, Lucía, et al. "Resistance to MAPK Inhibitors in Melanoma Involves Activation of the
809 IGF1R–MEK5–Erk5 PathwayResistance Mechanisms to MAPK Inhibitors in Melanoma." *Cancer*
810 *Research* 79.9 (2019): 2244-2256.

811 [54] Anerillas, Carlos, et al. "A BDNF-TrkB autocrine loop enhances senescent cell viability." *Nature*
812 *communications* 13.1 (2022): 1-17.

813 [55] Adam, Christian, et al. "Efficient suppression of NRAS-driven melanoma by co-inhibition of ERK1/2
814 and ERK5 MAPK pathways." *Journal of Investigative Dermatology* 140.12 (2020): 2455-2465.

815 [56] Randic, Tijana, et al. "NRAS mutant melanoma: towards better therapies." *Cancer Treatment*
816 *Reviews* 99 (2021): 102238.

817 [57] Cook, Simon J., and Pamela A. Lochhead. "ERK5 Signalling and Resistance to ERK1/2 Pathway
818 Therapeutics: The Path Less Travelled?." *Frontiers in Cell and Developmental Biology* 10 (2022).

819 [58] Jiang, W., Cai, F., Xu, H., Lu, Y., Chen, J., Liu, J., ... & Hua, Z. C. (2020). Extracellular signal regulated
820 kinase 5 promotes cell migration, invasion and lung metastasis in a FAK-dependent manner. *Protein &*
821 *cell*, *11*(11), 825-845.

822 [59] Ortiz, Maria A., et al. "Src family kinases, adaptor proteins and the actin cytoskeleton in epithelial-
823 to-mesenchymal transition." *Cell Communication and Signaling* 19.1 (2021): 1-19.

824 [60] Saleiro, D., Blyth, G. T., Kosciuczuk, E. M., Ozark, P. A., Majchrzak-Kita, B., Arslan, A. D., ... &
825 Platanias, L. C. (2018). IFN-γ–inducible antiviral responses require ULK1-mediated activation of MLK3
826 and ERK5. *Science signaling*, *11*(557), eaap9921.

827 [61] Lee, Bongyong, et al. "MicroRNA-211 modulates the DUSP6-ERK5 signaling axis to promote
828 BRAFV600E-driven melanoma growth in vivo and BRAF/MEK inhibitor resistance." *Journal of*
829 *Investigative Dermatology* 141.2 (2021): 385-394.

830 [62] Santiappillai, Nancy T., et al. "CDK4/6 Inhibition Reprograms Mitochondrial Metabolism in
831 BRAFV600 Melanoma via a p53 Dependent Pathway." *Cancers* 13.3 (2021): 524.

832 [63] Teh, Jessica LF, et al. "Metabolic Adaptations to MEK and CDK4/6 Cotargeting in Uveal
833 MelanomaMetabolic Adaptations to Inhibitors in Ocular Melanoma." *Molecular cancer therapeutics*
834 19.8 (2020): 1719-1726.

835 [64] Lee, Jae-Seon, et al. "Targeting oxidative phosphorylation reverses drug resistance in cancer cells
836 by blocking autophagy recycling." *Cells* 9.9 (2020): 2013.

837 [65] Corazao-Rozas, Paola, et al. "Mitochondrial oxidative phosphorylation controls cancer cell's life
838 and death decisions upon exposure to MAPK inhibitors." *Oncotarget* 7.26 (2016): 39473.

839 [66] Carpintero-Fernández, Paula, et al. "Genome wide CRISPR/Cas9 screen identifies the coagulation
840 factor IX (F9) as a regulator of senescence." Cell death & disease 13.2 (2022): 1-13.

841 [67] Martínez-Zamudio, Ricardo Iván, et al. "Escape From Oncogene-Induced Senescence is Controlled
842 by POU2F2 and Memorized by Chromatin Scars." bioRxiv (2022)

843 [68] Lee, Won Jae, et al. "Genome-wide overexpression screen identifies genes able to bypass p16-
844 mediated senescence in melanoma." SLAS DISCOVERY: Advancing Life Sciences R&D 22.3 (2017): 298-
845 308.

846 [69] Nagaraj, Karthik, et al. "Long-Term IGF1 Stimulation Leads to Cellular Senescence via Functional
847 Interaction with the Thioredoxin-Interacting Protein, TXNIP." *Cells* 11.20 (2022): 3260.]

848 [70] Rambow, Florian, et al. "Toward minimal residual disease-directed therapy in melanoma." Cell
849 174.4 (2018): 843-855.

850 [71] Marin-Bejar, Oskar, et al. "Evolutionary predictability of genetic versus nongenetic resistance to
851 anticancer drugs in melanoma." *Cancer Cell* 39.8 (2021): 1135-1149.

852 [72] Mölder, Felix, et al. "Sustainable data analysis with Snakemake." *F1000Research* 10 (2021).

[73] Xiao, Yufei, et al. "A novel significance score for gene selection and ranking." *Bioinformatics* 30.6 (2014): 801-807.

[74] Metz, Kathleen S., et al. "Coral: Clear and customizable visualization of human kinome data." *Cell systems* 7.3 (2018): 347-350.

[75] Glaab, E., Baudot, A., Krasnogor, N., Schneider, R., & Valencia, A. (2012). EnrichNet: network-based gene set enrichment analysis. *Bioinformatics*, *28*(18), i451-i457

[76] Travis, A. J., Moody, J., Helwak, A., Tollervey, D., & Kudla, G. (2014). Hyb: a bioinformatics pipeline for the analysis of CLASH (crosslinking, ligation and sequencing of hybrids) data. *Methods*, *65*(3), 263-273.

[77] Gligorijević, V., Malod-Dognin, N. & Pržulj, N. (2016). Patient-specific data fusion for cancer stratification and personalised treatment. *Pac. Symp. Biocomput*. 21, 321–332.

[78] Ding, C., Li, T., Peng, W. & Park, H. (2006). Orthogonal nonnegative matrix tri-factorizations for clustering. In Proc. *ACM SIGKDD International Conference on Knowledge Discovery and Data Mining*, Vol. 2006, 126–135, ACM Press.

[79] Hart, T., Komori, H. K., LaMere, S., Podshivalova, K., & Salomon, D. R. (2013). Finding the active genes in deep RNA-seq gene expression studies. *BMC Genomics*, *14*(1), 1-7.

[80] Pržulj, N. (2019). Analyzing Network Data in Biology and Medicine: An Interdisciplinary Textbook for Biological, Medical and Computational Scientists. Cambridge University Press.

[81] Qiao, H. (2015). New svd based initialization strategy for non-negative matrix factorization. *Pattern Recognition Letters*, 63, 71–77.

[82] Pržulj, N., Corneil, D. G. & Jurisica, I. (2004). Modeling interactome: scale-free or geometric? *Bioinformatics* 20, 3508–3515.

876 **Figure Legends**

877 Fig. 1 Experimental setup, cellular phenotypes and omics characterization. IPC298, MELJUSO and
878 SKMEL30 cell lines display different phenotypes upon CDK4/6i and MEKi. We characterised those using
879 RNA-seq, kinome profiling and qCLASH method. RNA-seq and qCLASH data were further combined to
880 construct a resistant miRNA network. Bulk and single-cell RNA-seq were finally integrated into "iCell"
881 networks.

882 Fig. 2 NRAS mutant melanoma trigger IFN and EMT responses upon MEKi and CDK4/6i. A. Principal
883 component analysis clusters cell lines separately reflecting distinct observed phenotypes. B. Gene Set
884 Enrichment Analysis using the hallmarks gene sets from MSigDB. All cell lines display an enrichment
885 in interferons responses and at day 14 in EMT. C. Senescence scores predicted by Cancer
886 SENESCopedia. SENESCopedia webtool (https://ccb.nki.nl/publications/cancer-senescence) uses a
887 gene expression classifier to predict senescence in cancer cell samples [18].

888 Fig. 3 MEKi and CDK4/6i lead to RTKs reactivation. A. Summary of significantly deregulated kinases. B.
889 Kinase activities after MEKi and CDK4/6i. ERK1/2 inhibition leads to RTKs activation. Rreceptors names
890 are colored according to the enriched pathways. C. Phylogenetic tree for SKMEL30 on day 1. The size
891 of the leafs represents the "Median Final Score", a score greater than 1.2 indicates a significant change
892 between conditions. The color of the branches and leaves shows the "Median Kinase Statistic", which
893 is the difference in kinase activity. Circles highlight RTKs contributing to enriched pathways. D. andE.
894 Activity of ERK5 in the senescent and adaptative cell lines. D. zoom on the MAPK pathway showing
895 the deregulation of ERK5 (*MAPK7*) in MELJUSO cell line. E. same for the SKMEL30 cell line.

896 Fig. 4 miRNA-mRNA interactions potentially contributing to resistance. A. Summary of the interactions
897 detected through the qCLASH method. B. Top part, correlations between hybrid counts (qCLASH) and
898 miRNA/mRNA counts (RNA-seq). Bottom part, summing hybrid counts per mRNA or miRNA (qCLASH)
899 further strengthen the correlations with the RNA-seq. To select candidates, we considered the
900 interactions detected in three technical replicates (colored circles). Then for the two cell lines,

901 interactions present in the resistant state but absent in the sensitive state were considered. Finally,
902 interactionscommon to the two cell lines IPC298 and SKMEL30 were used. D. RNA-seq data for
903 SKMEL30 cell line as log fold changes overlayed onto the resistant miRNA network. Selected
904 interactions for further validation by qPCR are represented with thick lines and the corresponding
905 mRNAs and miRNAs with bolded borders. E. Relative expression of LGALS3BP, TXNIP and TYRP1
906 mRNAs assessed by qPCR across three NRAS and two BRAF mutant melanoma cell lines. F. Relative
907 expression of miR-211-5p across the same cell lines.

908 Fig. 5 "iCell" integration of bulk and single-cell RNA-seq. A. Comparison of iCell networks topology
909 using Graphlet Correlation Distances (GCD). iCELL networks recapitulate phenotypic observations and
910 early adaptation of IPC298. B. Venn diagrams representing genes overlap between conditions. C.
911 Comparison of gene local topology using Graphlet Degree Signature Similarity (GDSS). Within all cell
912 lines, the different time points were compared. ORA was performed on the top 10% most "stable" or
913 "perturbated" genes. D. Genes were clustered according to their Graphlets Degree Signatures. ORA
914 was performed to associate gene clusters with biological function. E. Left panel: number of enriched
915 clusters detected for each gene across all conditions. Right panel, Number of detected clusters for the
916 EMT and iFN gamma pathways (related to senescence escape) for the two algorithms. F. Protein-
917 protein interactions (BioGRID) between P53 and the genes associated with EMT and IFN gamma.

918 Fig. 6 Graphical summary. The phenotypes observed across three different NRAS mutant melanoma
919 cell lines can be summarised as “senescent” (left) and “resistant” (right). Insulin signalling is associated
920 with the “senescent” phenotype and can be explained by the mechanism of action of MEKi, which
921 downregulates ERK1/2, suppressing negative feedback on RTKs. Interferon signaling Can be explained
922 by CDK4/6i, which downregulates DNMT1 leadingand lead to hypomethylation of the genome and
923 expression of Endogenous Retroviruses (ERVs). Induced expression of intracellular ERVs trigger an
924 innate immune response and production of interferons. IFN gamaγ can activate ERK5, inducing EMT.

925 This phenotype is moreover associated with upregulation of miR-211-5p, which indirectly regulates
926 ERK5.

927 **Tables**

928 Table 1. Enrichment results from PamGene data. Network-based enrichment was performed on the
929 significantly deregulated kinases at different time points. MELJUSO and SKMEL30 cells show at all time
930 points an enrichment in ErbB and neurotrophin pathway. Only MELJUSO cells show an enrichment in
931 insulin pathway at day 4 and day 33.

932 **Supplementary figures**

933 Supplementary Figure 1. Volcano plots for the total RNA-seq. MELJUSO, SKMEL30 and IPC298 cell lines
934 were treated with CDK4/6i and MEKi.

935 Supplementary Figure 2. Pamgene data acquisition, processing and interpretation workflow.

936 Supplementary Figure 3. Phylogenetic trees representing the kinome responses to MEKi and CDK4/6i.
937 The size of the leafs represents the "Median Final Score", a score greater than 1.2 indicates a
938 significant change between conditions. The color of the branchs and leafs shows the "Median Kinase
939 Statistic" which is the difference in kinase activity. Circles highlight RTKs contributing to enriched
940 pathways. SKMEL30 and MELJUSO cell lines show similar responses at early time points but not at 33
941 days.

942 Supplementary Figure 4. Pathway representation of ErbB signaling in MELJUSO cell line. The color of
943 the nodes represents the cellular localization while kinases are illustrated as rectangles with stripes
944 showing their activity at day 1, day4 and day 33.

945 Supplementary Figure 5. Pathway representation of ErbB signaling in SKMEL30 cell line. The color of
946 the nodes represents the cellular localization while kinases are illustrated as rectangles with stripes
947 showing their activity at day 1, day4 and day 33.

948 Supplementary Figure 6. Pathway representation of Neurotrophin signaling in MELJUSO cell line. The
949 color of the nodes represents the cellular localization while kinases are illustrated as rectangles with
950 stripes showing their activity at day 1, day4 and day 33.

951 Supplementary Figure 7. Pathway representation of Neurotrophin signaling in SKMEL30 cell line. The
952 color of the nodes represents the cellular localization while kinases are illustrated as rectangles with
953 stripes showing their activity at day 1, day4 and day 33.

954 Supplementary Figure 8. Pathway representation of Insulin signaling in MELJUSO cell line. The color of
955 the nodes represents the cellular localization while kinases are illustrated as rectangles with stripes
956 showing their activity at day 1, day4 and day 33.

957 Supplementary Figure 9. Upregulation of RTKs upon MEKi and CDK4/6i. The heatmap represents the
958 "Median Kinase Statistic" for kinases, significant values are represented in black. RTKs are colored
959 according to the enriched pathways in which they are involved.

960 Supplementary Figure 10. Volcano plots for the small RNA-seq. MELJUSO, SKMEL30 and IPC298 cell
961 lines were treated with CDK4/6i and MEKi.

962 Supplementary Figure 11. Principal Component analysis (PCA) for the top 500 most detected
963 interactions. PCA clearly distinguishes cell lines and conditions.

964 Supplementary Figure 12. miRNA/mRNA vs hybrids count detected in one, two or three biological
965 replicates. Interaction detected in triplicates are associated with greater expression values.

966 Supplementary Figure 13. miRNA/mRNA expression detected by qPCR across three NRAS and two
967 BRAF cell lines. Statistical significance was calculated for each condition using multiple welch's t-test
968 and an FDR of 0.01. Red rectangles highlight upregulated elements and blue rectangles,
969 downregulated elements.

970 Supplementary Figure 14. Expression of miRNAs and mRNAs detected by qPCR in let-7a, let-7f, miR-
971 27a, miR-146a, miR-211 and miR-320a hubs in SKMEL30.

972 Supplementary Figure 15. Expression of miRNAs and mRNAs detected by qPCR in let-7a, let-7f, miR-
973 27a, miR-146a, miR-211 and miR-320a hubs in IPC298.

974 Supplementary Figure 16. Workflow of the data integration, construction an investigation of the iCELL
975 networks.

976 Supplementary Figure 17. Comparison of gene topology using Graphlet Degree Signature Similarity
977 (GDSS) for matching time points. ORA was performed on the top 10% most "stable" or "perturbated"
978 genes. Venn diagrams represent genes overlap between conditions.

979 Supplementary Figure 18. Activation of the viral mimicry upon MEKi and CDK4/6i. MEK and CDK4/6
980 inhibitors converge on the E2F2 transcription factor. E2F2 regulates the DNA methyltransferase 1
981 enzyme (DNMT1) responsible for maintaining the DNA methylation profil. The downregulation of
982 DNMT1 leads to a global hypomethylation of the genome and allows the expression of Endogenous
983 retroviruses (ERVs). These transcripts hybridise in the cytoplasm and form dsRNA reminiscent of a viral
984 infection. Cytosolic Pattern Recognition Receptors (PRR) such as RIG-I or MDA5 or endosomal one
985 such as TLR3 then activate the innate immune system leading to an interferon signaling.

986 Supplementary Figure 19. Expression of common regulators of senescence and EMT as listed by (Mir
987 Mohd Faheem et al. 2020) upon MEKi and CDK4/6i.

988 Supplementary Figure 20. Trend in expression between the “EMT” and IFN gamma gene sets from the
989 hallmarks MSigDB and a recent “senescence” gene list. A. Scheme representing the relationships
990 between the different gene sets. B. Heatmap for the "INTERFERON GAMMA RESPONSE" and
991 "EPITHELIAL MESENCHYMAL TRANSITION" hallmarks gene sets and the “SenMayo” gene list [28].

992 Supplementary Figure 21. Activation of Src Family Kinases (SFKs). The heatmap represents the
993 "Median Kinase Statistic" for kinases, significant values are represented in black.

994 Supplementary Figure 22. Interferon Gamma response upon MEKi and CDK4/6i. The heatmap
995 represents the logFC of the genes which contribute to the enrichment result. More precisely, it

996 represents a sub-selection of the "INTERFERON GAMMA RESPONSE" gene set which contributes to
997 the "leading edge" (ascendant portion) of the running sum used in GSEA.

998 Supplementary Figure 23. Expression of TRPM1 transcripts in total RNA-seq. TRPM1 transcript
999 contains miR-211-5p in an intronic region.

1000 Supplementary Figure 24. Pathway enrichment on qCLASH data using KEGG references. Samples were
1001 normalised for read depth and total number of detections for hybrids was summed across technical
1002 replicates. Those were further summarised per mRNA and contrasted between conditions. Finally, the
1003 top 5% most differentially targeted were used to perform ORA to relate these gene lists to KEGG
1004 pathways.

1005 **Supplementary tables**

1006 Supplementary Table 1. Characteristics and concentrations of inhibitors used for the different cell
1007 lines across the study.

1008 Supplementary Table 2. 90 genes associated with senescence escape and numbers of clusters
1009 enriched for the two algorithms: hierarchical clustering and k-medoids.

1010 Supplementary Table 3. Primer list for mRNA and miRNAs measured by qPCR.

1011

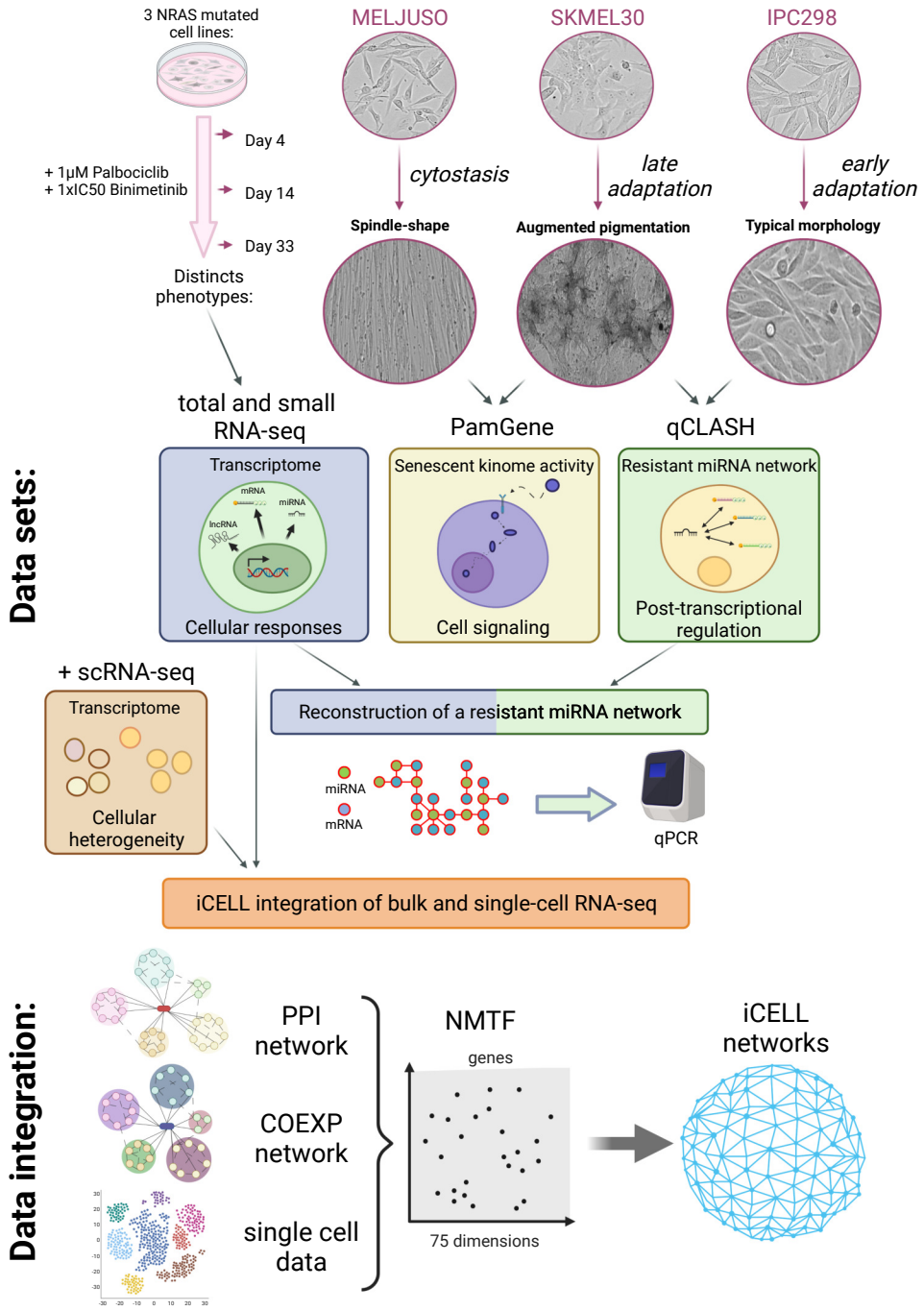
3 NRAS mutated cell lines:
MELJUSO
SKMEL30
IPC298
Day 4
+ 1μM Palbociclib
+ 1xIC50 Binimetinib
Day 14
Day 33
cytostasis
late adaptation
early adaptation
Spindle-shape
Augmented pigmentation
Typical morphology
Distincts phenotypes:
total and small RNA-seq
PamGene
qCLASH
Data sets:
Transcriptome
mRNA
miRNA
lncRNA
Cellular responses
Senescent kinome activity
Cell signaling
Resistant miRNA network
Post-transcriptional regulation
+ scRNA-seq
Transcriptome
Cellular heterogeneity
Reconstruction of a resistant miRNA network
miRNA
mRNA
qPCR
iCELL integration of bulk and single-cell RNA-seq
Data integration:
PPI network
COEXP network
single cell data
NMTF
genes
75 dimensions
iCELL networks

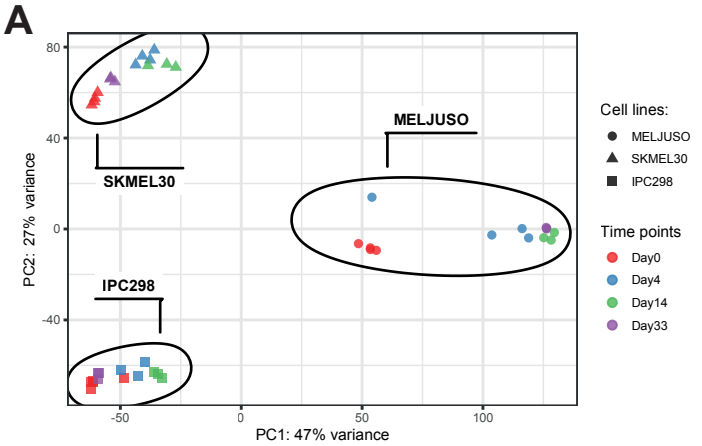
A
MELJUSO
SKMEL30
IPC298
PC2: 27% variance
PC1: 47% variance
80
40
0
-40
-50
0
50
100
Cell lines:
MELJUSO
SKMEL30
IPC298
Time points
Day0
Day4
Day14
Day33

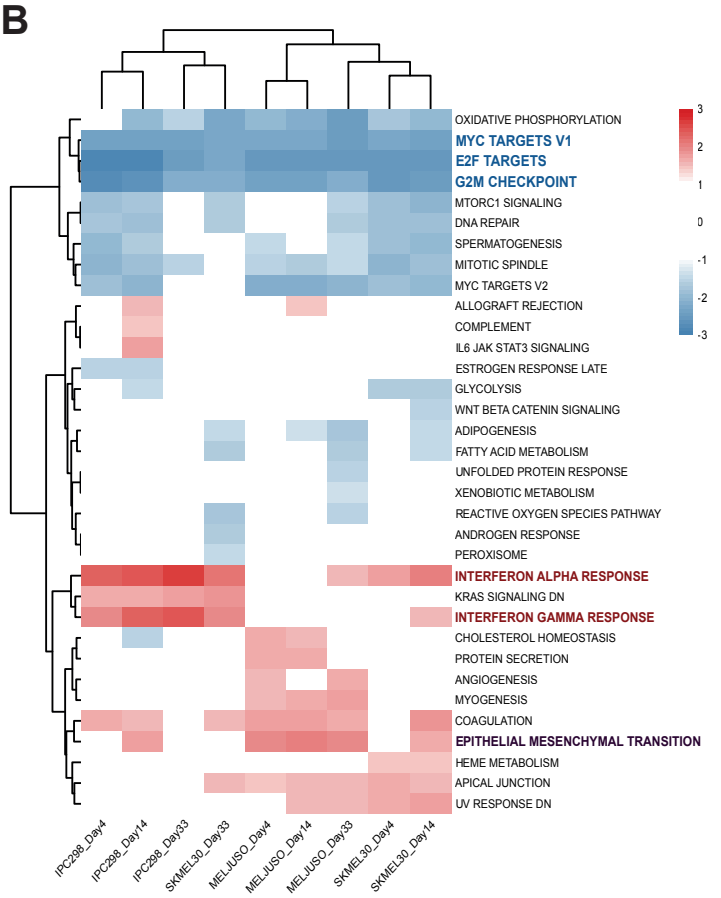
B
OXIDATIVE PHOSPHORYLATION
MYC TARGETS V1
E2F TARGETS
G2M CHECKPOINT
MTORC1 SIGNALING
DNA REPAIR
SPERMATOGENESIS
MITOTIC SPINDLE
MYC TARGETS V2
ALLOGRAFT REJECTION
COMPLEMENT
IL6 JAK STAT3 SIGNALING
ESTROGEN RESPONSE LATE
GLYCOLYSIS
WNT BETA CATENIN SIGNALING
ADIPOGENESIS
FATTY ACID METABOLISM
UNFOLDED PROTEIN RESPONSE
XENOBIOTIC METABOLISM
REACTIVE OXYGEN SPECIES PATHWAY
ANDROGEN RESPONSE
PEROXISOME
INTERFERON ALPHA RESPONSE
KRAS SIGNALING DN
INTERFERON GAMMA RESPONSE
CHOLESTEROL HOMEOSTASIS
PROTEIN SECRETION
ANGIOGENESIS
MYOGENESIS
COAGULATION
EPITHELIAL MESENCHYMAL TRANSITION
HEME METABOLISM
APICAL JUNCTION
UV RESPONSE DN
IPC298_Day4
IPC298_Day14
IPC298_Day33
SKMEL30_Day33
MELJUSO_Day4
MELJUSO_Day14
MELJUSO_Day33
SKMEL30_Day4
SKMEL30_Day14
3
2
1
0
-1
-2
-3

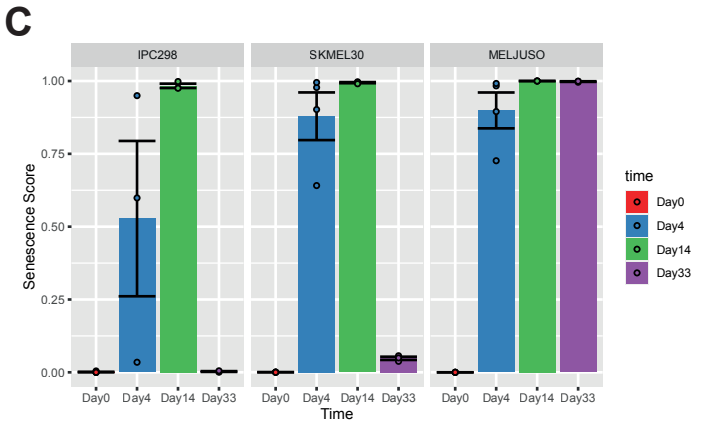
C
IPC298
SKMEL30
MELJUSO
Senescence Score
1.00
0.75
0.50
0.25
0.00
Day0
Day4
Day14
Day33
Time
time
Day0
Day4
Day14
Day33

A

Cell line	Time	Deregulated kinases	Total kinases
MelJuso	Day1	61	157
MelJuso	Day4	73	157
MelJuso	Day33	90	157
SKMel30	Day1	52	162
SKMel30	Day4	71	162
SKMel30	Day33	40	162

B

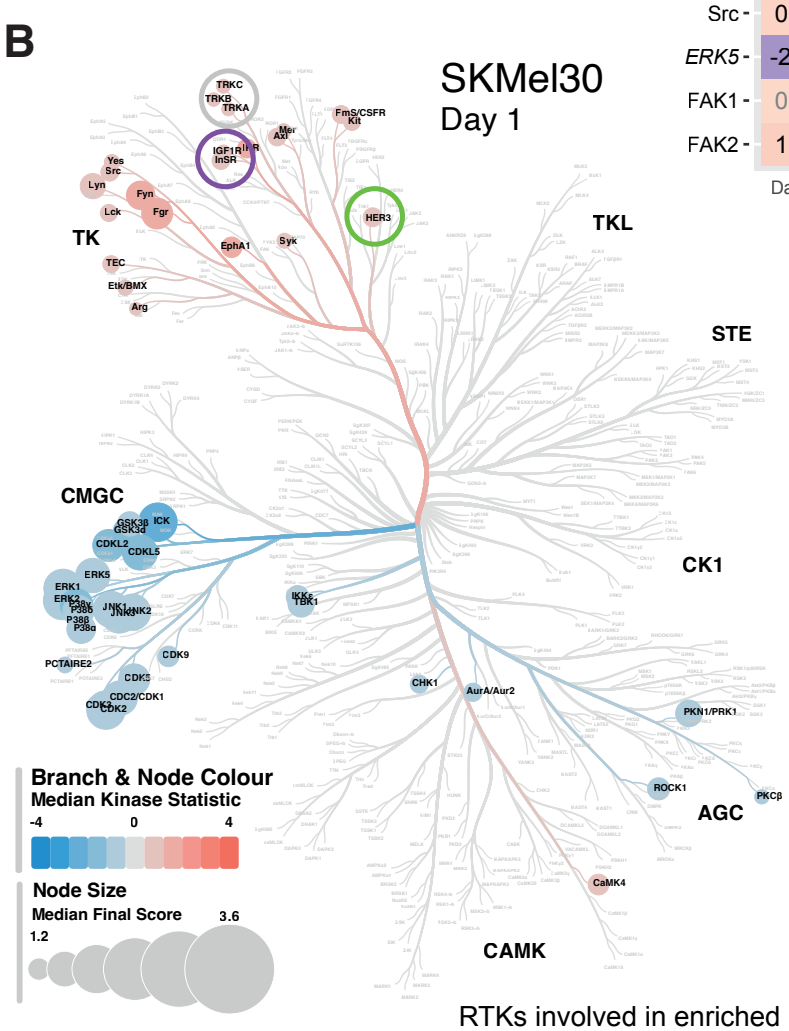

C

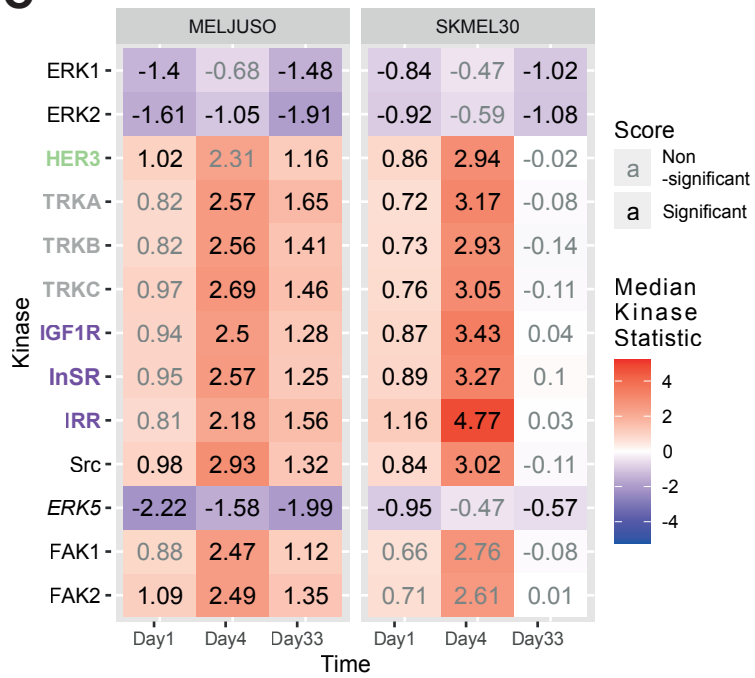

D

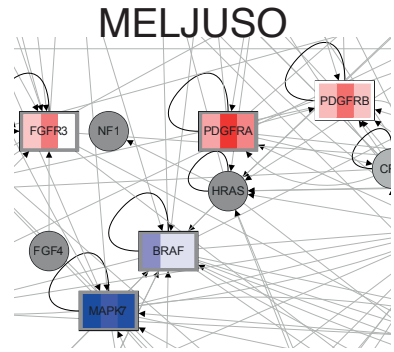

E

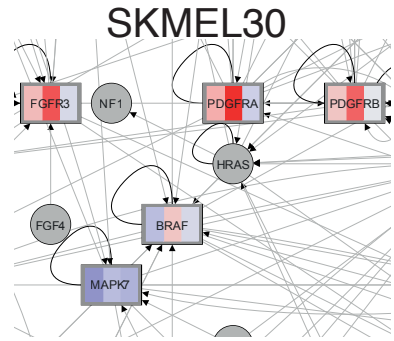

RTKs involved in enriched pathways:

○: ErbB signaling ○ : Neurotrophin signaling ○ : Insulin signaling

A

Cell line	Time	Deregulated kinases	Total kinases
MelJuso	Day1	61	157
MelJuso	Day4	73	157
MelJuso	Day33	90	157
SKMel30	Day1	52	162
SKMel30	Day4	71	162
SKMel30	Day33	40	162

B

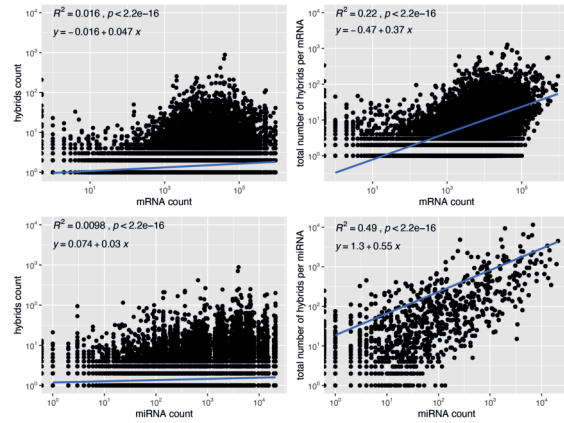

C

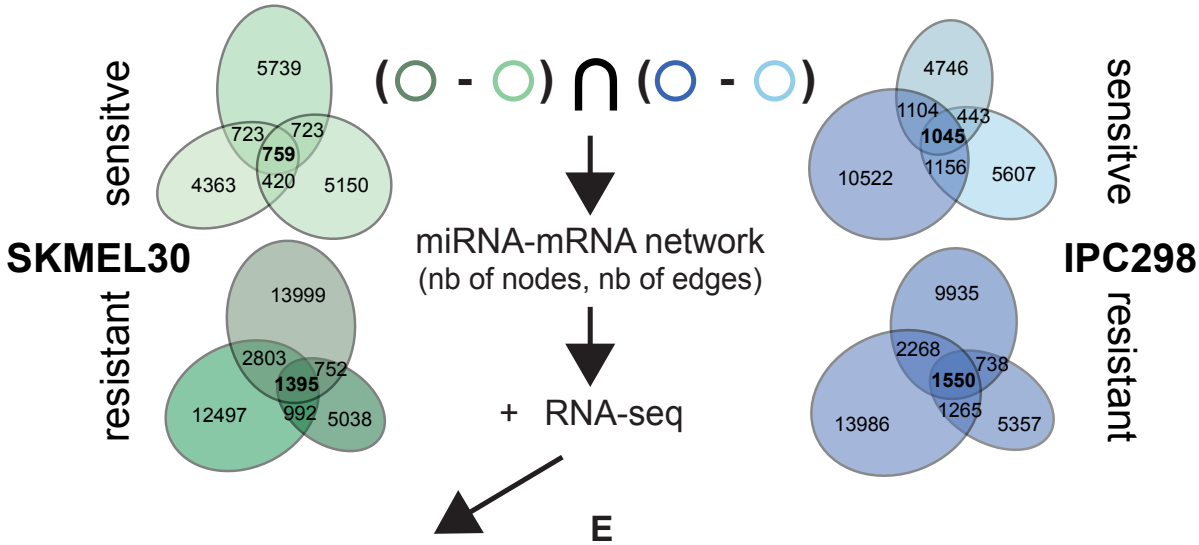

D

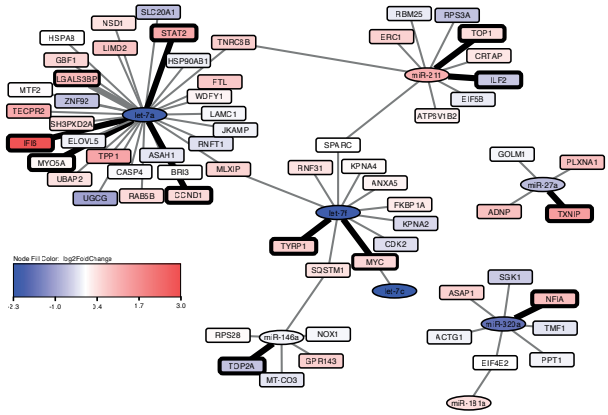

E

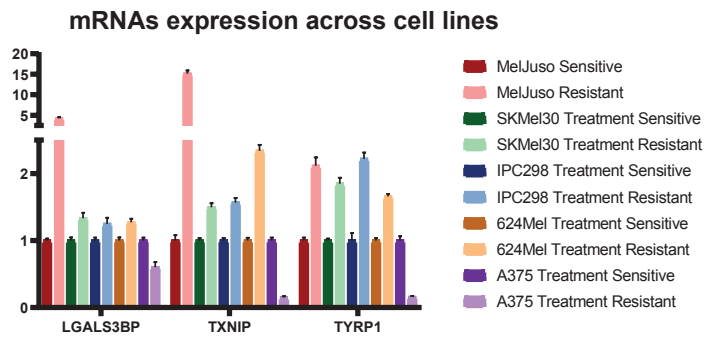

F

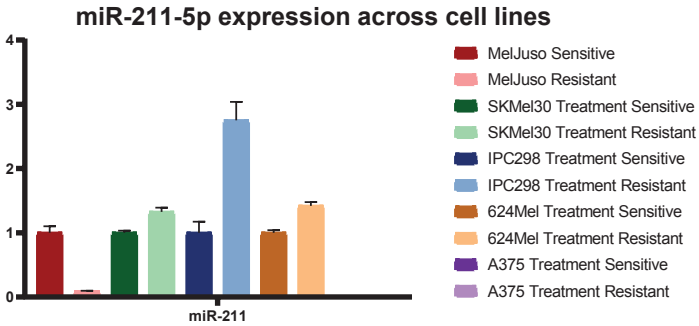

G

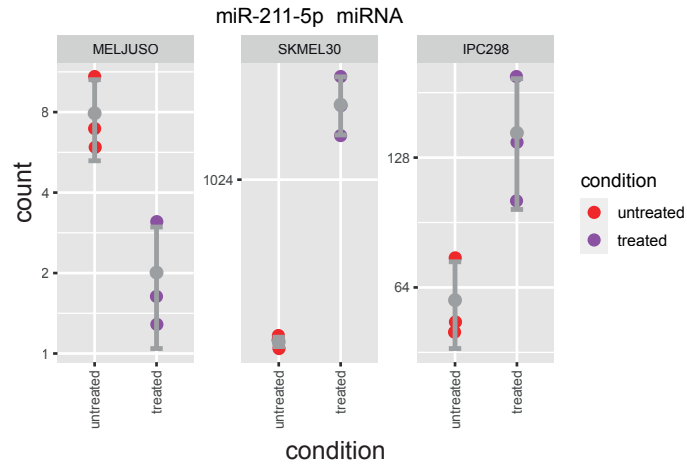

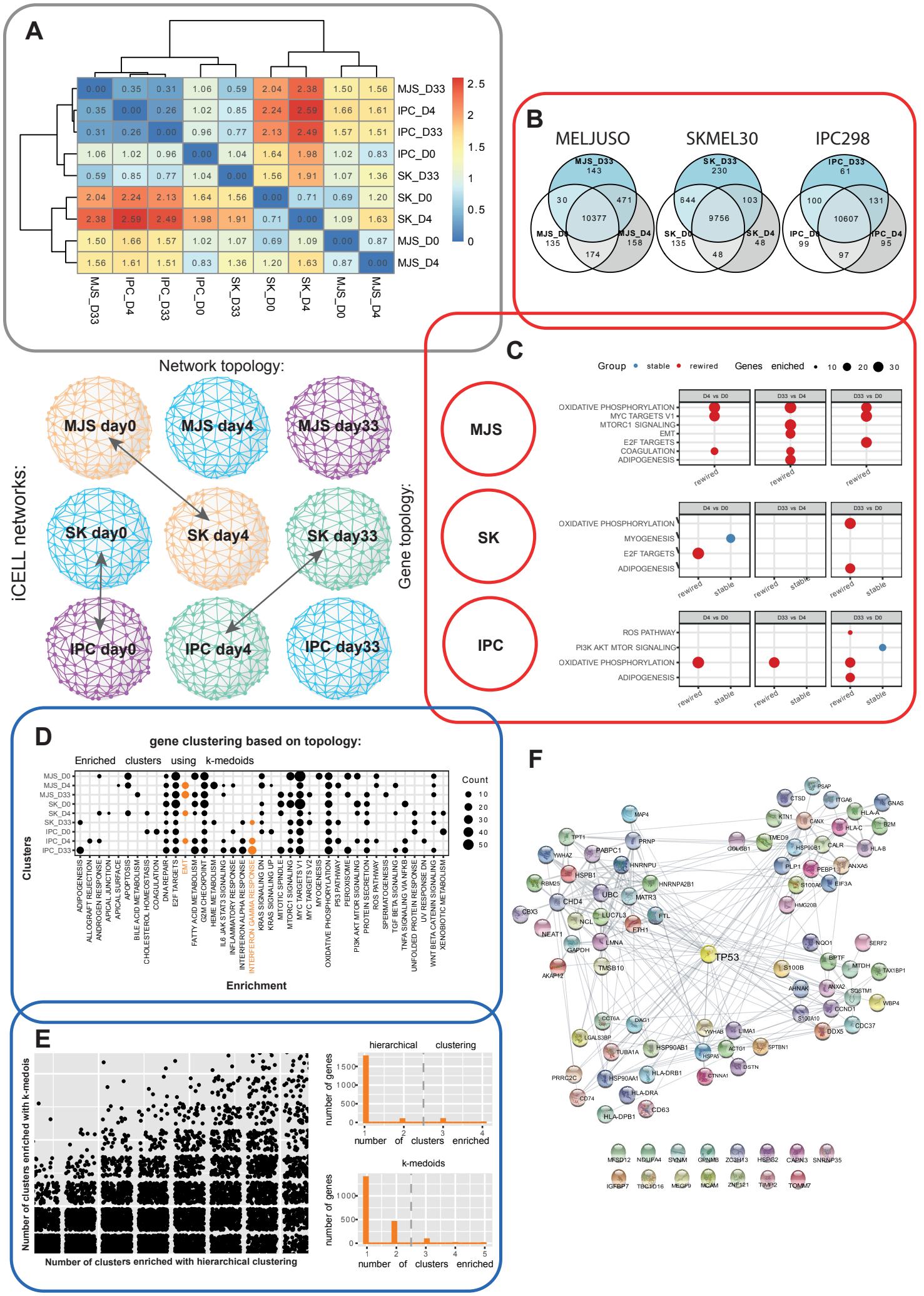
A
MJS_D33 0.00 0.35 0.31 1.06 0.59 2.04 2.38 1.50 1.56
IPC_D4 0.35 0.00 0.26 1.02 0.85 2.24 2.59 1.66 1.61
IPC_D33 0.31 0.26 0.00 0.96 0.77 2.13 2.49 1.57 1.51
IPC_D0 1.06 1.02 0.96 0.00 1.04 1.64 1.98 1.02 0.83
SK_D33 0.59 0.85 0.77 1.04 0.00 1.56 1.91 1.07 1.36
SK_D0 2.04 2.24 2.13 1.64 1.56 0.00 0.71 0.69 1.20
SK_D4 2.38 2.59 2.49 1.98 1.91 0.71 0.00 1.09 1.63
MJS_D0 1.50 1.66 1.57 1.02 1.07 0.69 1.09 0.00 0.87
MJS_D4 1.56 1.61 1.51 0.83 1.36 1.20 1.63 0.87 0.00
2.5
2
1.5
1
0.5
0
B
MELJUSO
MJS_D33 143
30
471
10377
MJS_D0 135
MJS_D4 158
174
SKMEL30
SK_D33 230
644
103
9756
SK_D0 135
SK_D4 48
48
IPC298
IPC_D33 61
100
131
10607
IPC_D0 99
IPC_D4 95
97
Network topology:
MJS day0
MJS day4
MJS day33
SK day0
SK day4
SK day33
IPC day0
IPC day4
IPC day33
iCELL networks:
Gene topology:
C
Group stable rewired
Genes enriched 10 20 30
MJS
SK
IPC
D4 vs D0
D33 vs D4
D33 vs D0
OXIDATIVE PHOSPHORYLATION
MYC TARGETS V1
MTORC1 SIGNALING
EMT
E2F TARGETS
COAGULATION
ADIPOGENESIS
MYOGENESIS
ROS PATHWAY
PI3K AKT MTOR SIGNALING
rewired
stable
D
gene clustering based on topology:
Enriched clusters using k-medoids
Clusters
Count
10
20
30
40
50
MJS_D0
MJS_D4
MJS_D33
SK_D0
SK_D4
SK_D33
IPC_D0
IPC_D4
IPC_D33
ADIPOGENESIS
ALLOGRAFT REJECTION
ANDROGEN RESPONSE
APICAL JUNCTION
APICAL SURFACE
APOPTOSIS
BILE ACID METABOLISM
CHOLESTEROL HOMEOSTASIS
COAGULATION
DNA REPAIR
E2F TARGETS
EMT
FATTY ACID METABOLISM
G2M CHECKPOINT
HEME METABOLISM
IL6 JAK STAT3 SIGNALING
INFLAMMATORY RESPONSE
INTERFERON ALPHA RESPONSE
INTERFERON GAMMA RESPONSE
KRAS SIGNALING DN
KRAS SIGNALING UP
MITOTIC SPINDLE
MTORC1 SIGNALING
MYC TARGETS V1
MYC TARGETS V2
MYOGENESIS
OXIDATIVE PHOSPHORYLATION
P53 PATHWAY
PEROXISOME
PI3K AKT MTOR SIGNALING
PROTEIN SECRETION
ROS PATHWAY
SPERMATOGENESIS
TGF BETA SIGNALING
TNFA SIGNALING VIA NFKB
UNFOLDED PROTEIN RESPONSE
UV RESPONSE DN
WNT BETA CATENIN SIGNALING
XENOBIOTIC METABOLISM
Enrichment
E
Number of clusters enriched with k-medois
Number of clusters enriched with hierarchical clustering
hierarchical clustering
number of genes
1500
1000
500
0
1 2 3 4
number of clusters enriched
k-medoids
number of genes
1000
500
0
1 2 3 4 5
number of clusters enriched
F
TP53
MAP4
PRNP
TPT1
PABPC1
YWHAZ
HNRNPU
HSPB1
HNRNPA2B1
RBM25
UBC
MATR3
CHD4
CBX3
LUC7L3
NCL
FTL
FTH1
NEAT1
LMNA
GAPDH
TMSB10
AKAP12
PSAP
CTSD
ITGA6
GNAS
KTN1
CANX
HLA-A
HLA-C
B2M
GOLGB1
TMED9
HSP90B1
CALR
HLA-B
PLP1
PEBP1
ANXA5
S100A6
EIF3A
HMG20B
NQO1
SERF2
BPTF
S100B
MTDH
TAX1BP1
AHNAK
ANXA2
SQSTM1
WBP4
CCND1
S100A10
CDC37
DDX5
CCT6A
DAG1
YWHAB
LIMA1
LGALS3BP
TUBA1A
HSP90AB1
ACTG1
SPTBN1
HSPA5
DSTN
PRRC2C
HSP90AA1
HLA-DRB1
CTNNA1
HLA-DRA
CD74
CD63
HLA-DPB1
MFSD12
NDUFA4
SYNM
GRNMB
ZC3H13
HSPG2
CAPN3
SNRNP35
IGFBP7
TBC1D16
MEGF9
MCAM
ZNF121
TIMP2
TOMM7

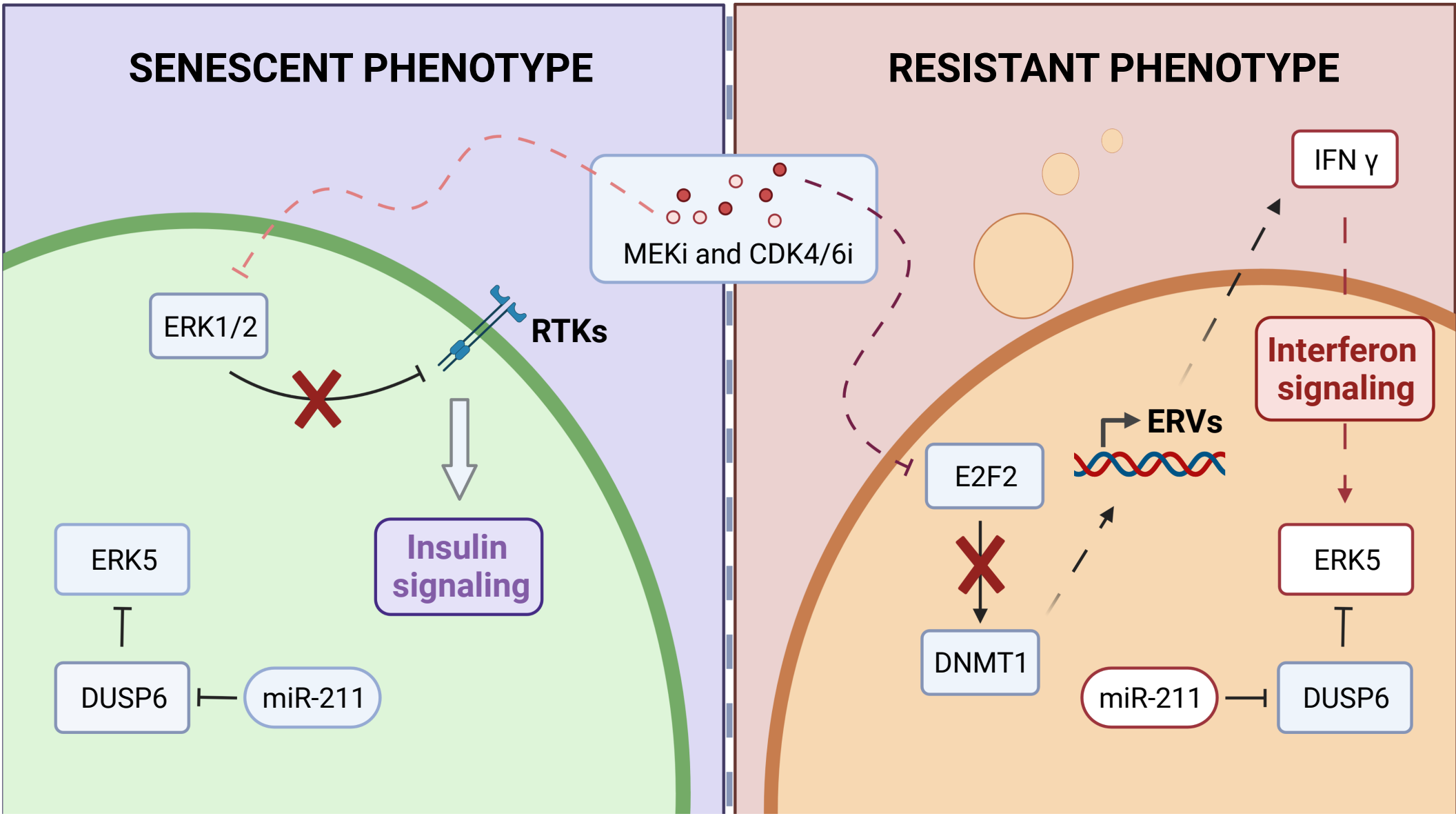
SENESCENT PHENOTYPE
RESISTANT PHENOTYPE
MEKi and CDK4/6i
ERK1/2
RTKs
Insulin signaling
ERK5
DUSP6
miR-211
IFN γ
Interferon signaling
ERVs
E2F2
DNMT1
ERK5
miR-211
DUSP6

Pathway enrichment results for MELJUSO cell line

Day1			Day4			Day33		
Pathway Name	XD-score	p-adj	Pathway Name	XD-score	p-adj	Pathway Name	XD-score	p-adj
Shigellosis	1.83	6.12E-20	mTOR signaling pathway	1.13	1.33E-10	Type II diabetes mellitus	1.42	1.49E-09
NOD-like receptor signaling pathway	1.38	6.69E-14	Acute myeloid leukemia	1.05	1.50E-09	mTOR signaling pathway	1.08	2.57E-11
Epithelial cell signaling in Helicobacter pylori infection	1.12	3.49E-13	Type II diabetes mellitus	0.89	3.91E-06	**ErbB signaling pathway**	1.01	3.31E-12
Progesterone-mediated oocyte maturation	1.02	1.41E-14	Glioma	0.86	8.12E-08	Acute myeloid leukemia	1.00	3.13E-10
RIG-I-like receptor signaling pathway	1.00	1.99E-11	**ErbB signaling pathway**	0.86	2.02E-10	Fc epsilon RI signaling pathway	0.95	4.51E-12
ErbB signaling pathway	0.97	2.54E-13	Gap junction	0.77	3.34E-09	Progesterone-mediated oocyte maturation	0.95	4.23E-12
GnRH signaling pathway	0.93	1.47E-14	Prion diseases	0.75	2.78E-04	Glioma	0.95	1.69E-08
Type II diabetes mellitus	0.91	8.02E-07	Adherens junction	0.72	1.69E-07	Prion diseases	0.95	2.91E-05
Fc epsilon RI signaling pathway	0.90	6.70E-13	Fc gamma R-mediated phagocytosis	0.71	2.99E-10	Adipocytokine signaling pathway	0.87	2.60E-08
Neurotrophin signaling pathway	0.89	4.52E-17	VEGF signaling pathway	0.68	5.13E-08	VEGF signaling pathway	0.86	5.62E-10
Toll-like receptor signaling pathway	0.89	5.76E-14	Fc epsilon RI signaling pathway	0.65	7.58E-09	Shigellosis	0.86	1.53E-07
Pancreatic cancer	0.76	1.12E-08	Prostate cancer	0.65	5.45E-08	**Neurotrophin signaling pathway**	0.83	5.38E-13
Colorectal cancer	0.75	1.52E-07	Long-term potentiation	0.65	1.48E-06	Aldosterone-regulated sodium reabsorption	0.82	4.81E-05
T cell receptor signaling pathway	0.73	2.23E-12	Aldosterone-regulated sodium reabsorption	0.64	3.96E-04	Gap junction	0.82	7.28E-11
VEGF signaling pathway	0.69	6.13E-09	Tight junction	0.62	6.96E-11	Prostate cancer	0.80	1.21E-09
Acute myeloid leukemia	0.57	9.12E-08	Vascular smooth muscle contraction	0.60	4.24E-09	Adherens junction	0.79	3.65E-08
Prostate cancer	0.56	9.34E-08	**Insulin signaling pathway**	0.59	1.38E-10	GnRH signaling pathway	0.77	9.13E-11
Leishmaniasis	0.48	6.22E-06	**Neurotrophin signaling pathway**	0.59	2.88E-10	T cell receptor signaling pathway	0.75	3.13E-11
Dorso-ventral axis formation	0.48	1.13E-02	Progesterone-mediated oocyte maturation	0.58	8.17E-07	Long-term potentiation	0.72	2.77E-07
			GnRH signaling pathway	0.55	6.47E-08	NOD-like receptor signaling pathway	0.71	1.45E-06
			Adipocytokine signaling pathway	0.53	2.89E-05	Pancreatic cancer	0.69	2.77E-07
			Hedgehog signaling pathway	0.52	7.95E-05	Fc gamma R-mediated phagocytosis	0.65	1.68E-09
			Long-term depression	0.51	7.43E-07	Toll-like receptor signaling pathway	0.64	4.58E-09
			T cell receptor signaling pathway	0.47	2.18E-07	Epithelial cell signaling in Helicobacter pylori infection	0.63	2.77E-07
			Chemokine signaling pathway	0.44	4.38E-14	Long-term depression	0.59	1.26E-07
						Vascular smooth muscle contraction	0.55	2.33E-08
						Insulin signaling pathway	0.54	9.87E-10
						Colorectal cancer	0.54	3.31E-05

RTKs involved in enriched pathways: ◯: ErbB signaling ◯: Neurotrophin signaling ◯: Insulin signaling

Pathway enrichment results for SKMEL30 cell line

Day1			Day4			Day33		
Pathway Name	XD-score	p-adj	Pathway Name	XD-score	p-adj	Pathway Name	XD-score	p-adj
Shigellosis	1.27	1.09E-13	Acute myeloid leukemia	1.27	8.19E-10	Shigellosis	1.17	1.64E-11
Fc epsilon RI signaling pathway	1.17	2.92E-16	Glioma	0.91	4.31E-08	NOD-like receptor signaling pathway	1.02	3.88E-10
NOD-like receptor signaling pathway	1.12	5.18E-11	mTOR signaling pathway	0.83	1.43E-09	Dorso-ventral axis formation	0.94	2.69E-04
Progesterone-mediated oocyte maturation	0.95	1.99E-13	**ErbB signaling pathway**	0.80	1.52E-09	Pancreatic cancer	0.85	1.06E-09
Type II diabetes mellitus	0.94	4.51E-07	Type II diabetes mellitus	0.74	4.02E-05	Type II diabetes mellitus	0.80	2.89E-06
RIG-I-like receptor signaling pathway	0.91	3.10E-10	Adipocytokine signaling pathway	0.71	1.06E-06	Epithelial cell signaling in Helicobacter pylori infection	0.79	1.70E-08
Epithelial cell signaling in Helicobacter pylori infection	0.88	2.11E-10	Long-term potentiation	0.69	7.97E-07	Progesterone-mediated oocyte maturation	0.78	4.11E-10
GnRH signaling pathway	0.87	2.04E-13	Fc gamma R-mediated phagocytosis	0.66	2.29E-09	Fc epsilon RI signaling pathway	0.75	1.53E-09
Neurotrophin signaling pathway	0.86	3.07E-16	Gap junction	0.60	3.74E-07	GnRH signaling pathway	0.74	1.54E-11
ErbB signaling pathway	0.80	9.43E-11	Prostate cancer	0.59	3.74E-07	**ErbB signaling pathway**	0.65	5.44E-09
Toll-like receptor signaling pathway	0.75	1.70E-11	Fc epsilon RI signaling pathway	0.58	6.98E-08	Toll-like receptor signaling pathway	0.62	1.04E-09
VEGF signaling pathway	0.73	2.85E-09	Vascular smooth muscle contraction	0.57	2.42E-08	RIG-I-like receptor signaling pathway	0.58	6.16E-07
Aldosterone-regulated sodium reabsorption	0.69	9.10E-05	Prion diseases	0.54	2.70E-03	T cell receptor signaling pathway	0.57	1.31E-09
T cell receptor signaling pathway	0.69	2.45E-11	Adherens junction	0.52	1.93E-05	Leishmaniasis	0.57	6.62E-07
Leishmaniasis	0.65	1.91E-07	**Neurotrophin signaling pathway**	0.49	2.15E-08	Colorectal cancer	0.54	9.30E-06
Adherens junction	0.65	2.25E-07	Apoptosis	0.49	4.20E-06	Endometrial cancer	0.51	9.97E-05
Colorectal cancer	0.64	1.78E-06	Tight junction	0.46	5.47E-08	**Neurotrophin signaling pathway**	0.47	3.13E-09
Prion diseases	0.54	1.08E-03	Non-small cell lung cancer	0.46	7.94E-05	VEGF signaling pathway	0.42	8.77E-06
Dorso-ventral axis formation	0.52	8.88E-03	Vibrio cholerae infection	0.46	7.74E-04			
Amyotrophic lateral sclerosis (ALS)	0.48	2.12E-04	Aldosterone-regulated sodium reabsorption	0.46	3.50E-03			
			Long-term depression	0.43	6.55E-06			
			Salivary secretion	0.42	6.05E-05			
			Progesterone-mediated oocyte maturation	0.41	6.05E-05			
			Gastric acid secretion	0.40	2.79E-04			
			VEGF signaling pathway	0.37	1.14E-04			

Supplementary Figures

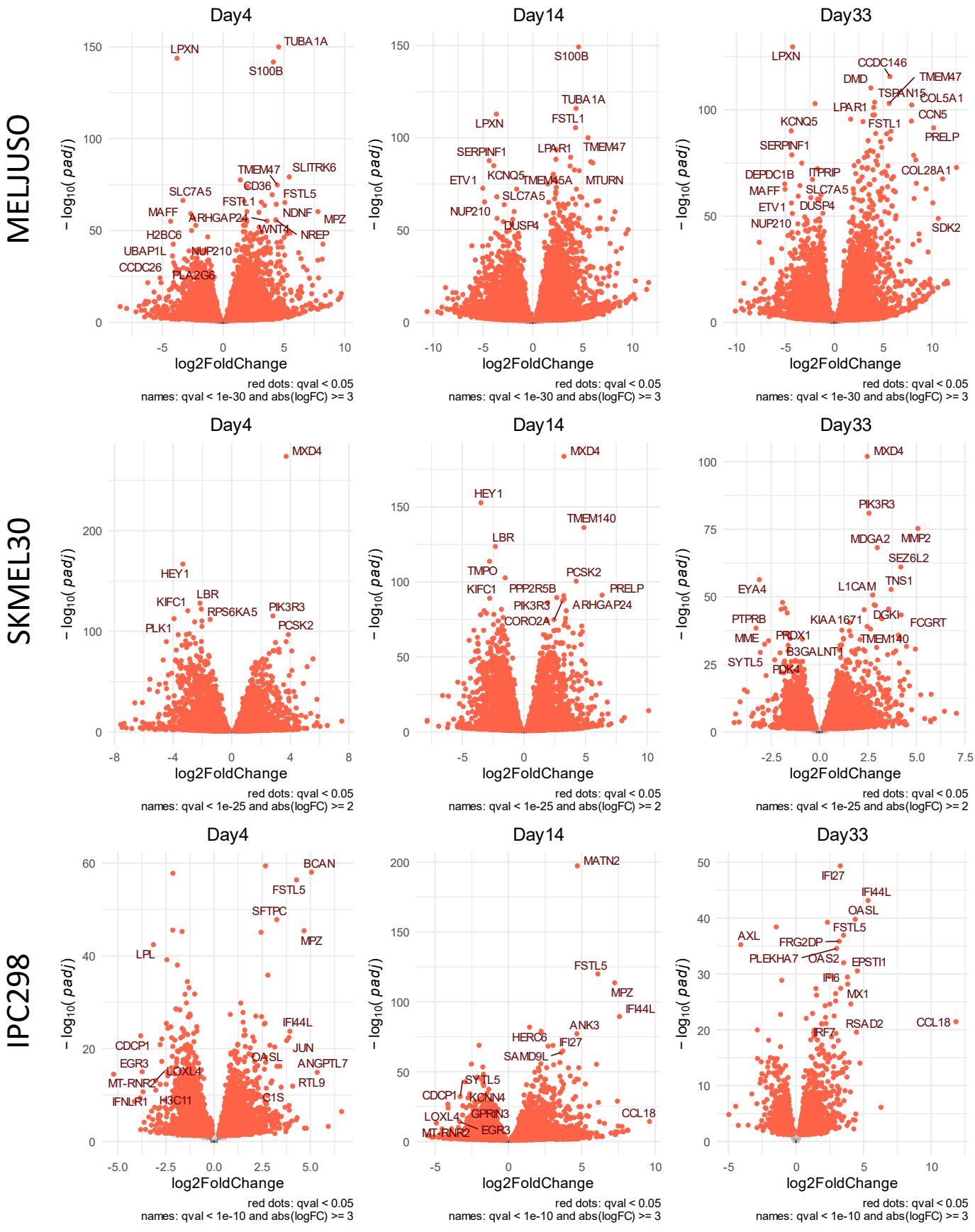

Supplementary Figure 1.

DATA COLLECTION

1

Cell lysate

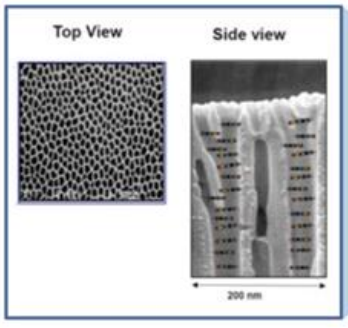

PamStation®12

Peptides phosphorylation level

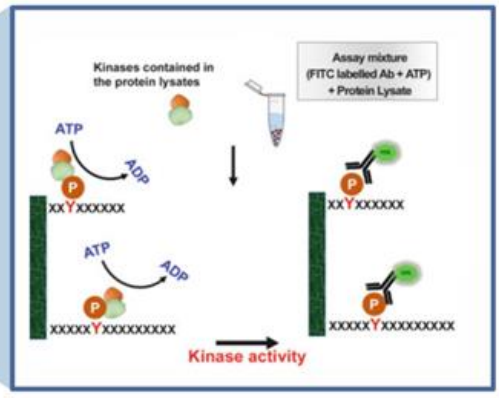

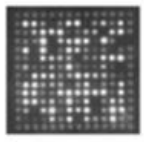

Light intensity read-out

DATA PROCESSING

2

Quality control → Normalization (Combat vs. VSN) → Inference of kinases activities

INTERPRETATION

3

Pathway enrichment

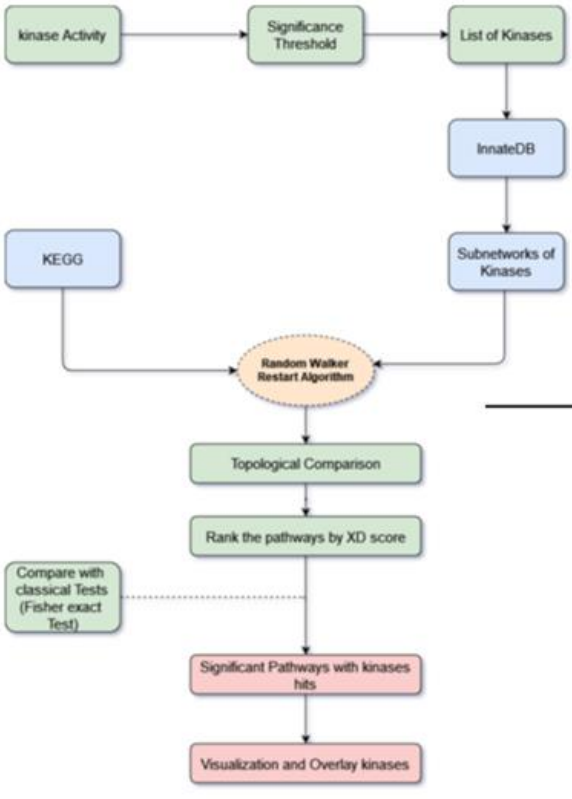

Pathway overlay

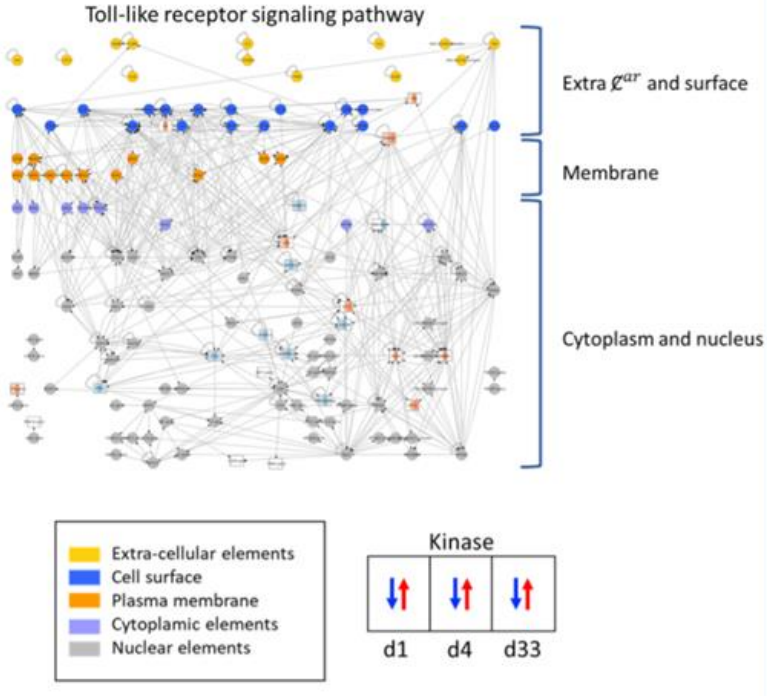

Supplementary Figure 2.

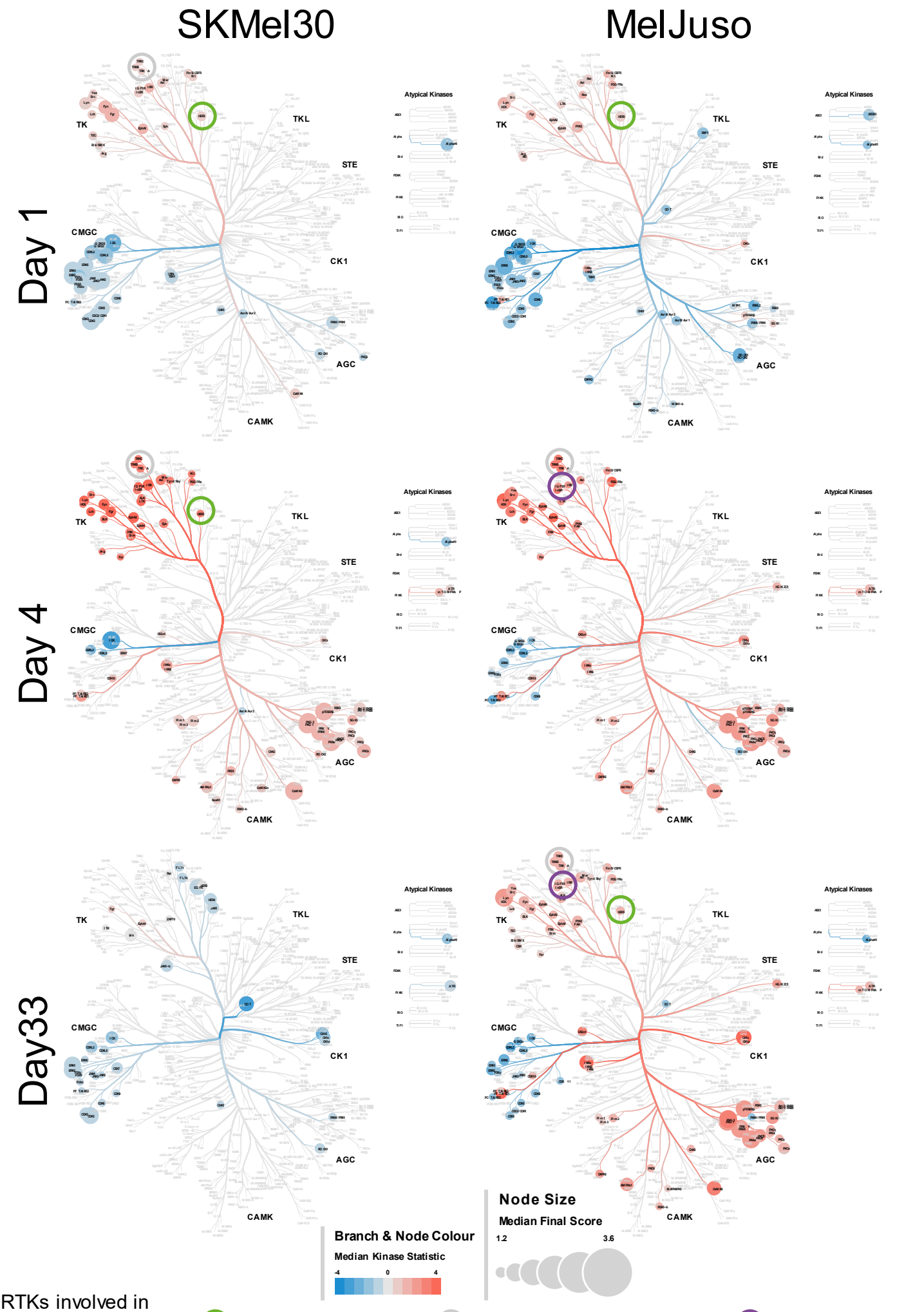

RTKs involved in enriched pathways: : ErbB signaling : Neurotrophin signaling : Insulin signaling

Supplementary Figure 3.

MELJUSO

ErbB signaling pathway

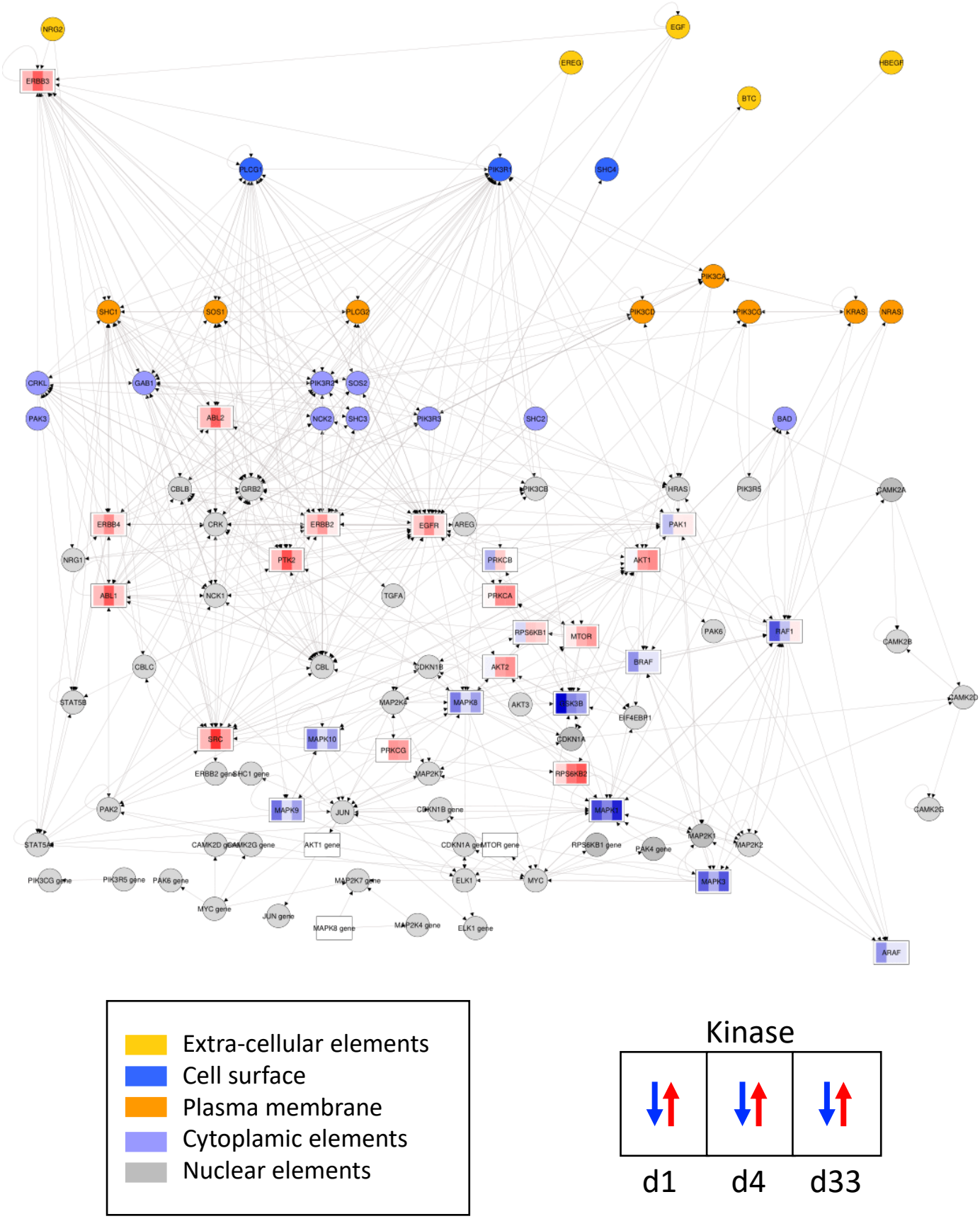

Extra-cellular elements
Cell surface
Plasma membrane
Cytoplamic elements
Nuclear elements

Kinase

d1 d4 d33

Supplementary Figure 4.

SKMEL30

ErbB signaling pathway

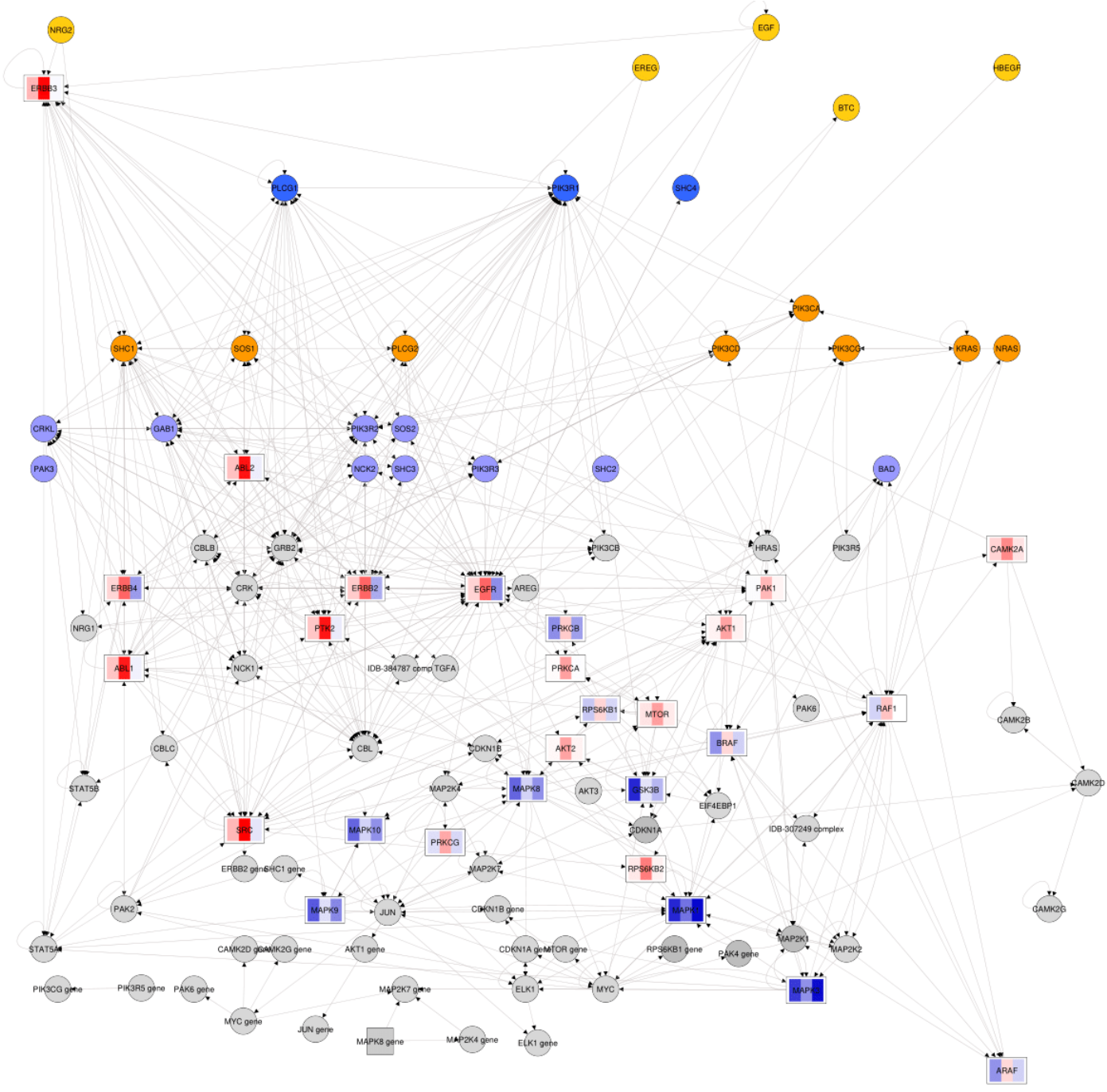

Extra-cellular elements
Cell surface
Plasma membrane
Cytoplamic elements
Nuclear elements

Kinase

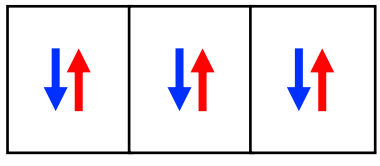

d1 d4 d33

Supplementary Figure 5.

MELJUSO

Neurotrophin signaling pathway

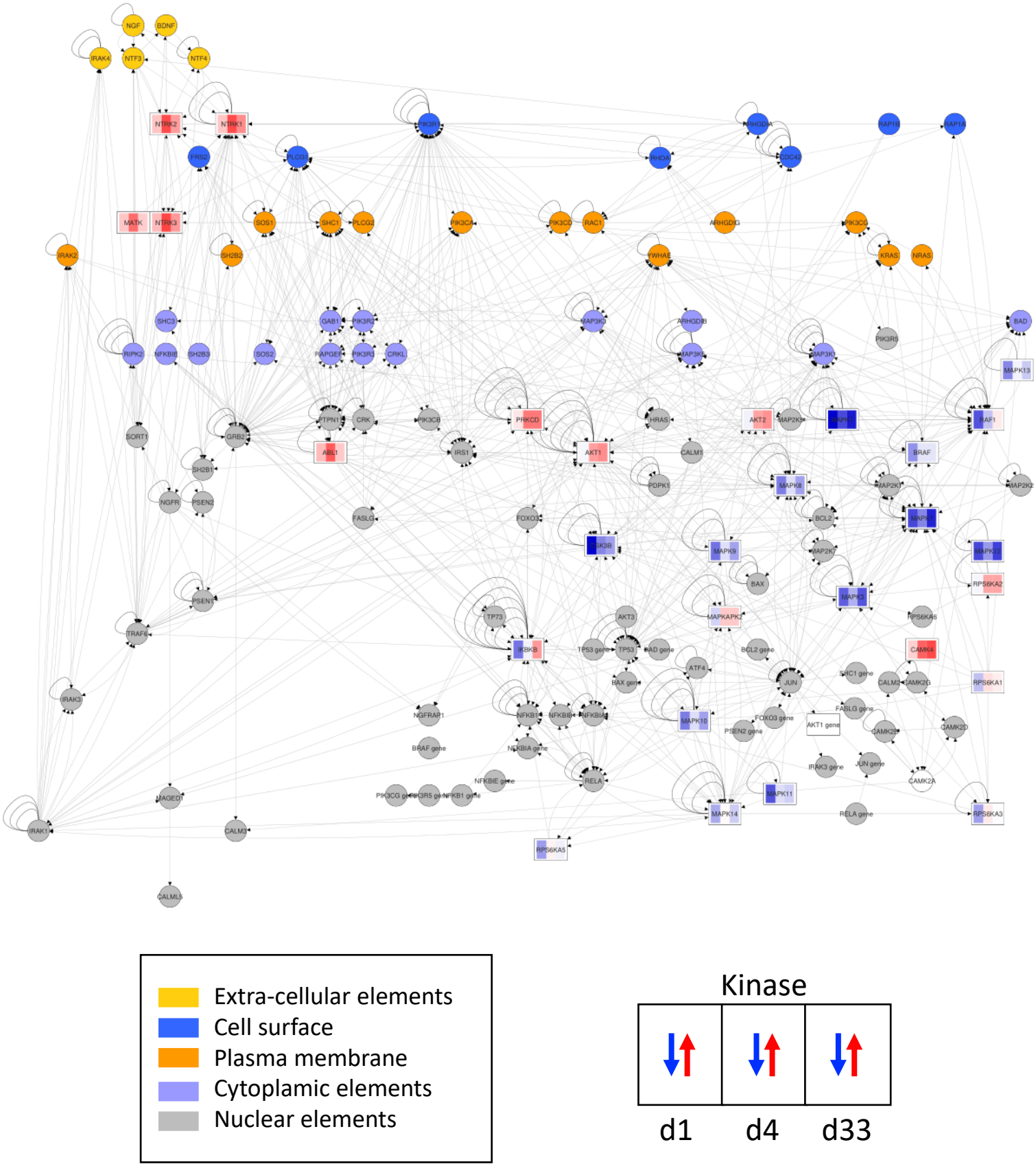

Supplementary Figure 6.

SKMEL30

Neurotrophin signaling pathway

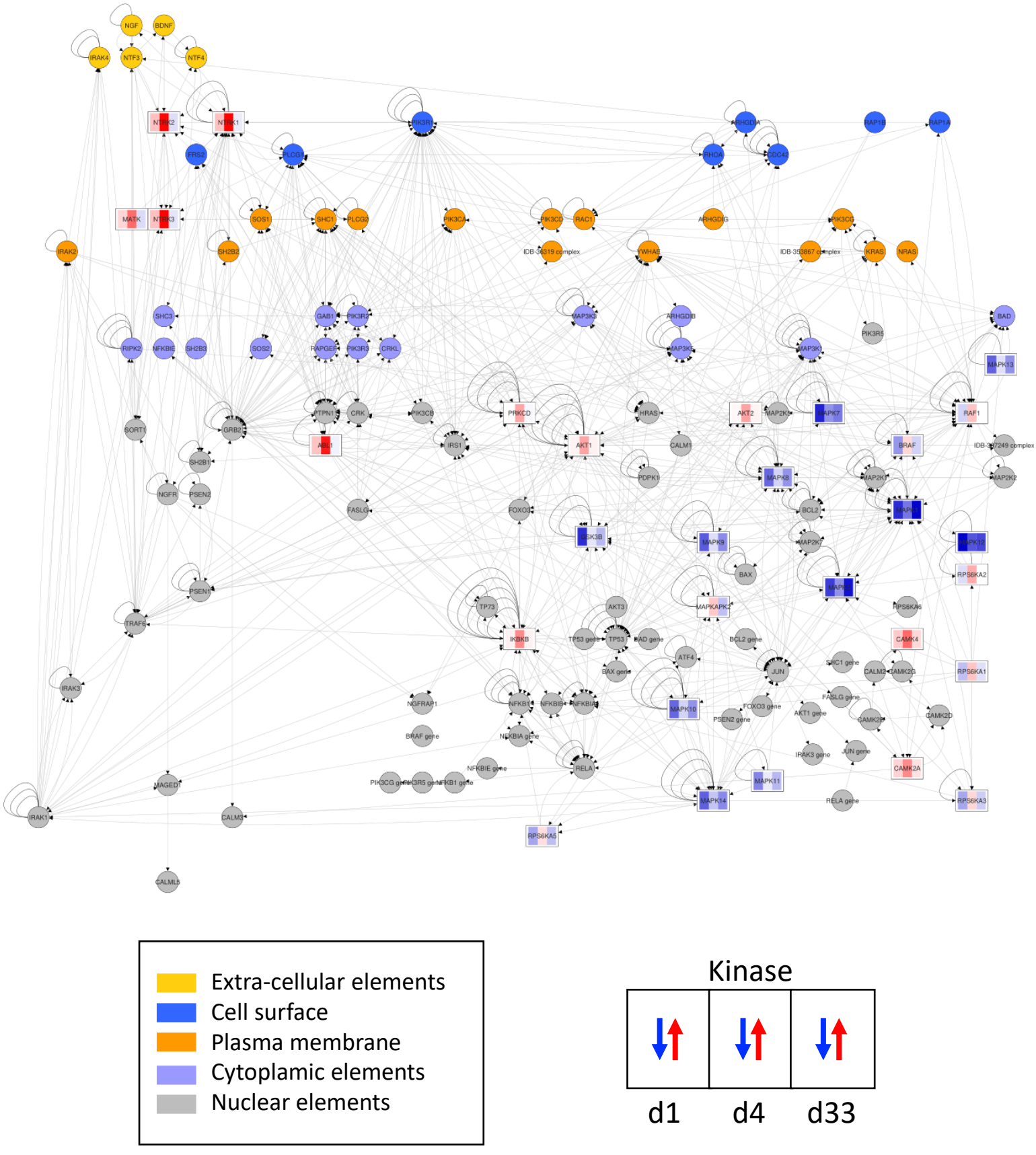

Supplementary Figure 7.

MELJUSO

Insulin signaling pathway

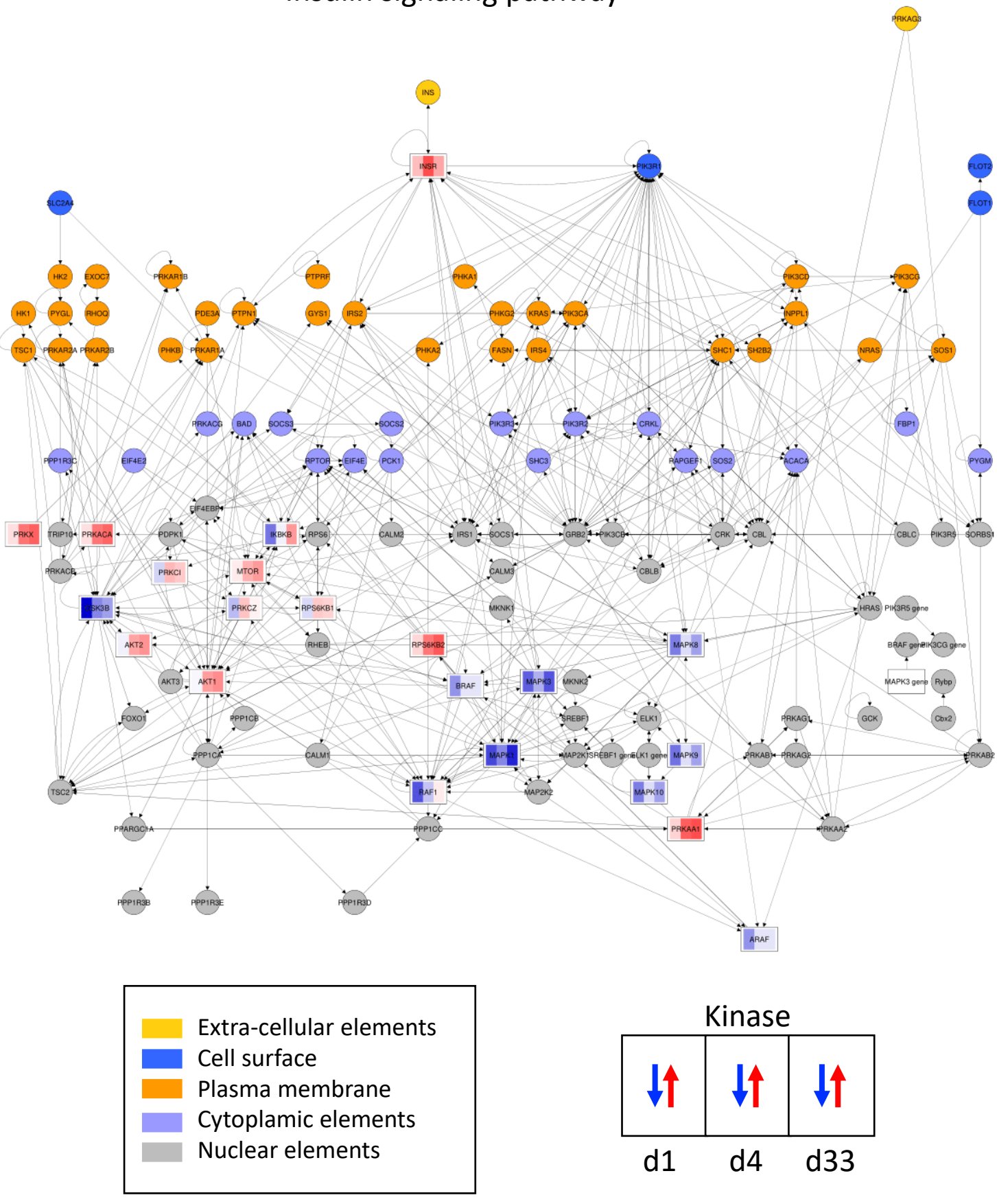

Supplementary Figure 8.

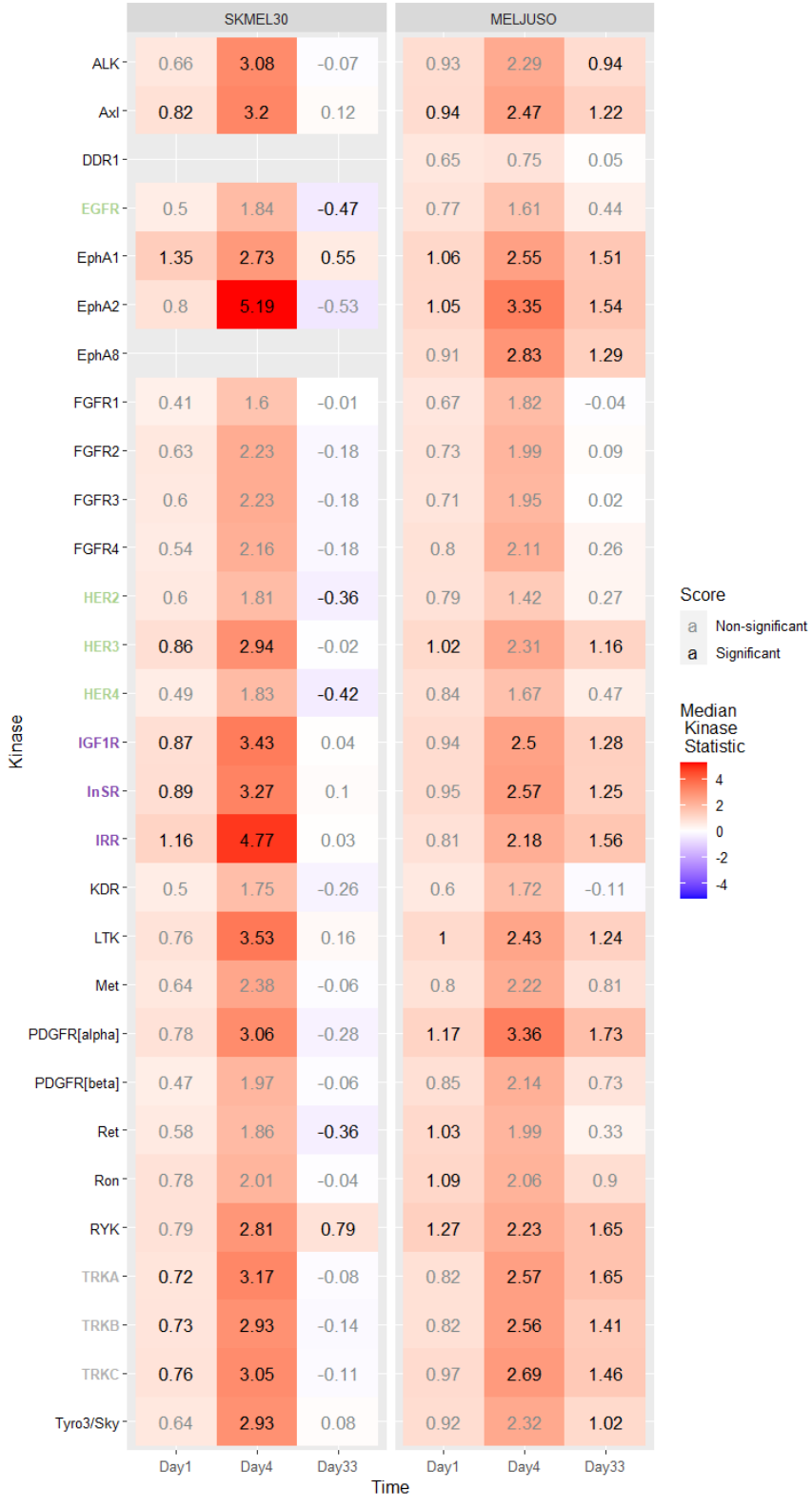

Supplementary Figure 9.

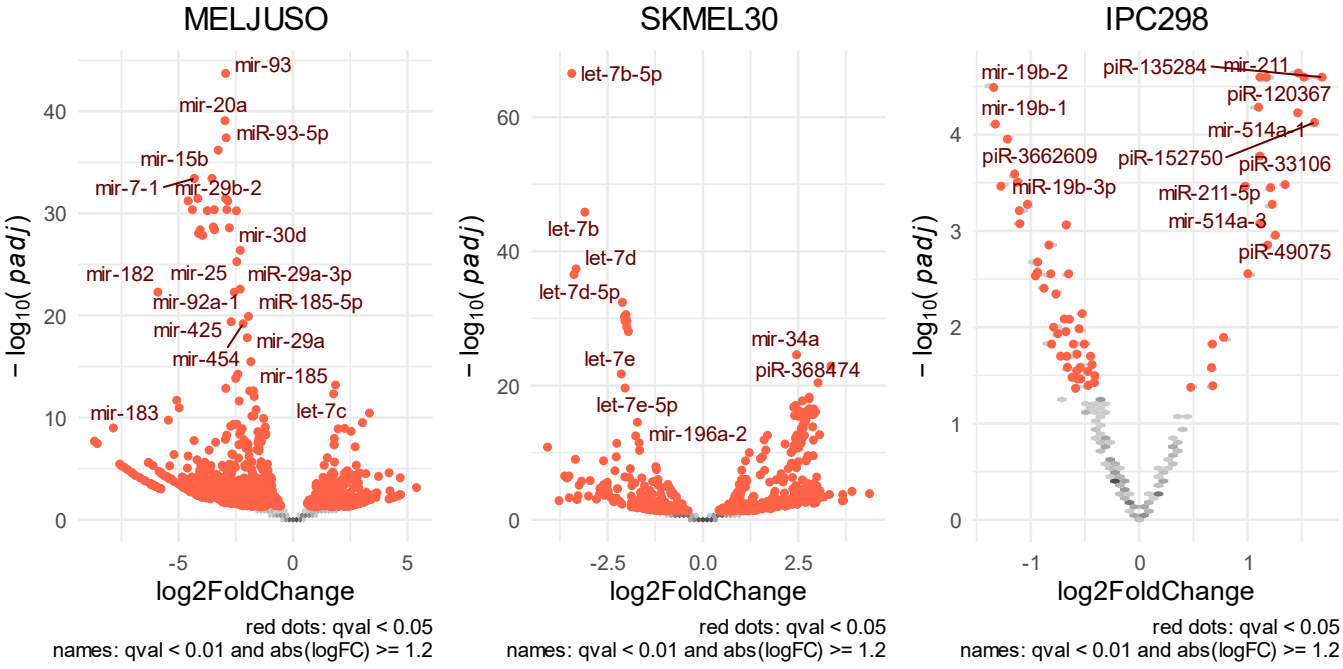

Supplementary Figure 10.

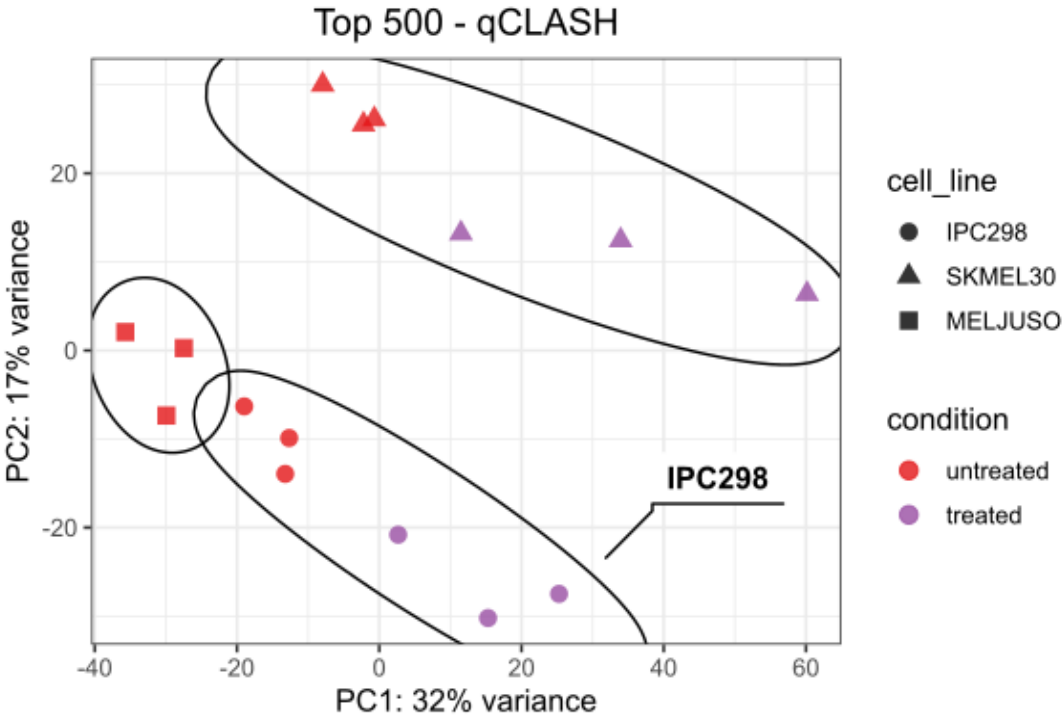

Supplementary Figure 11.

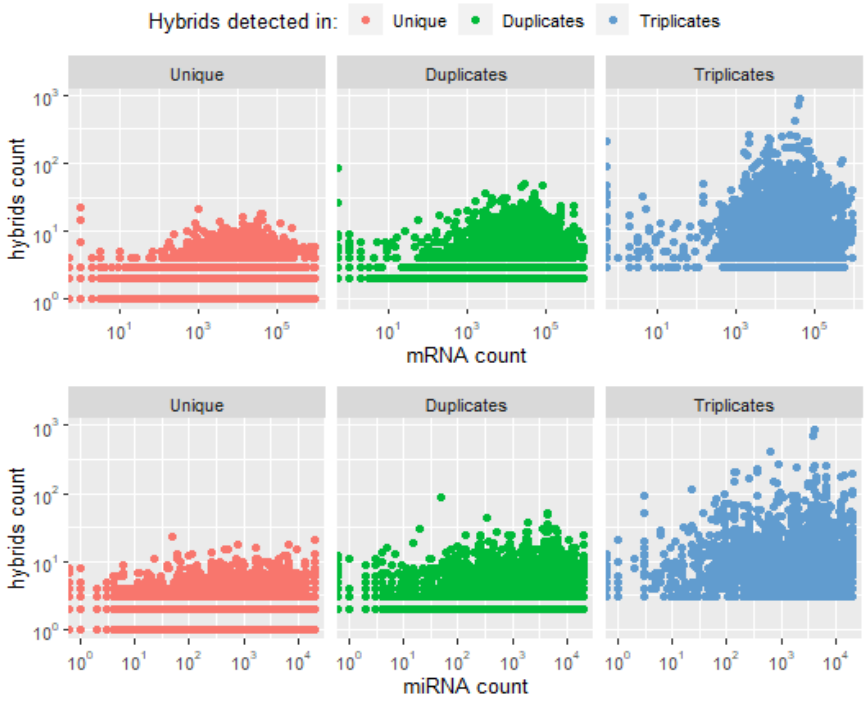

Supplementary Figure 12.

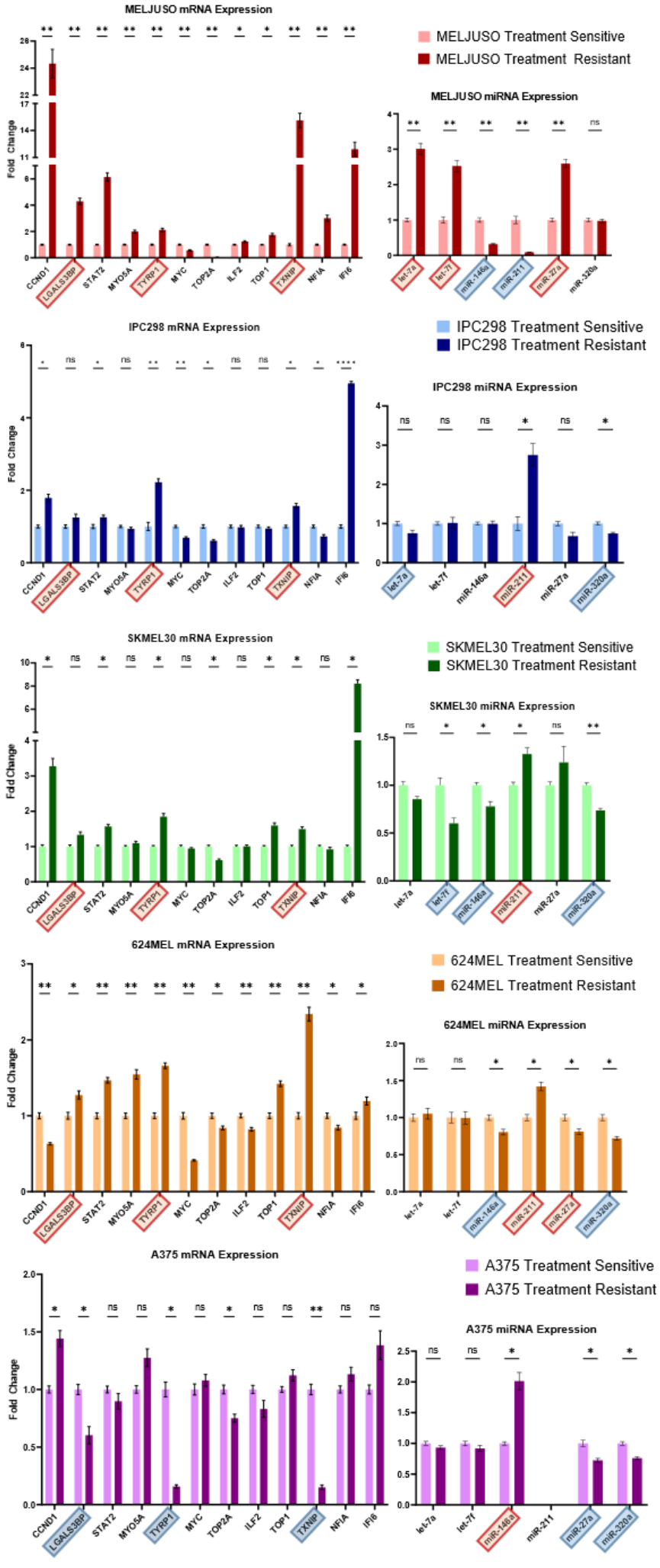

Supplementary Figure 13.

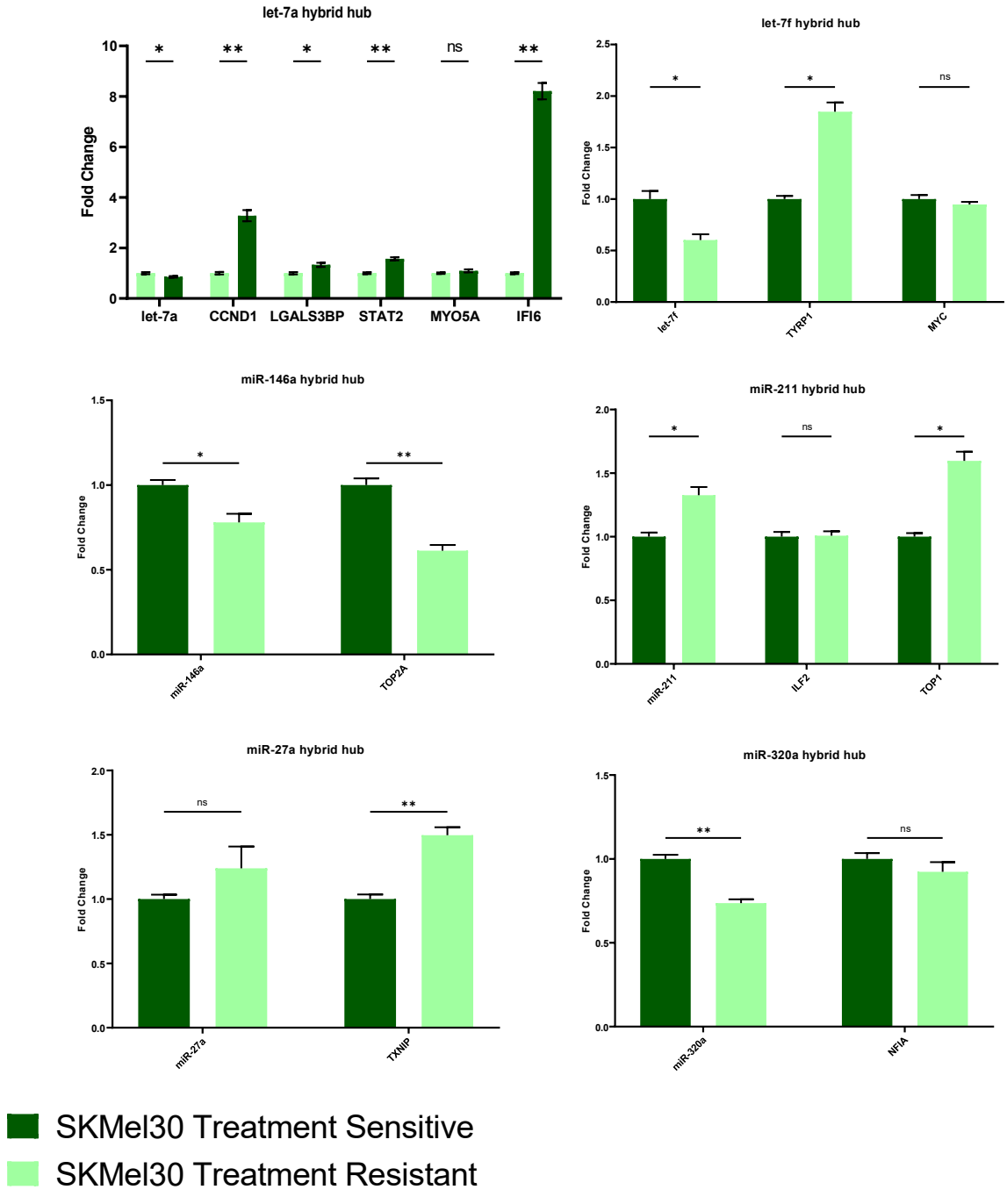

Supplementary Figure 14.

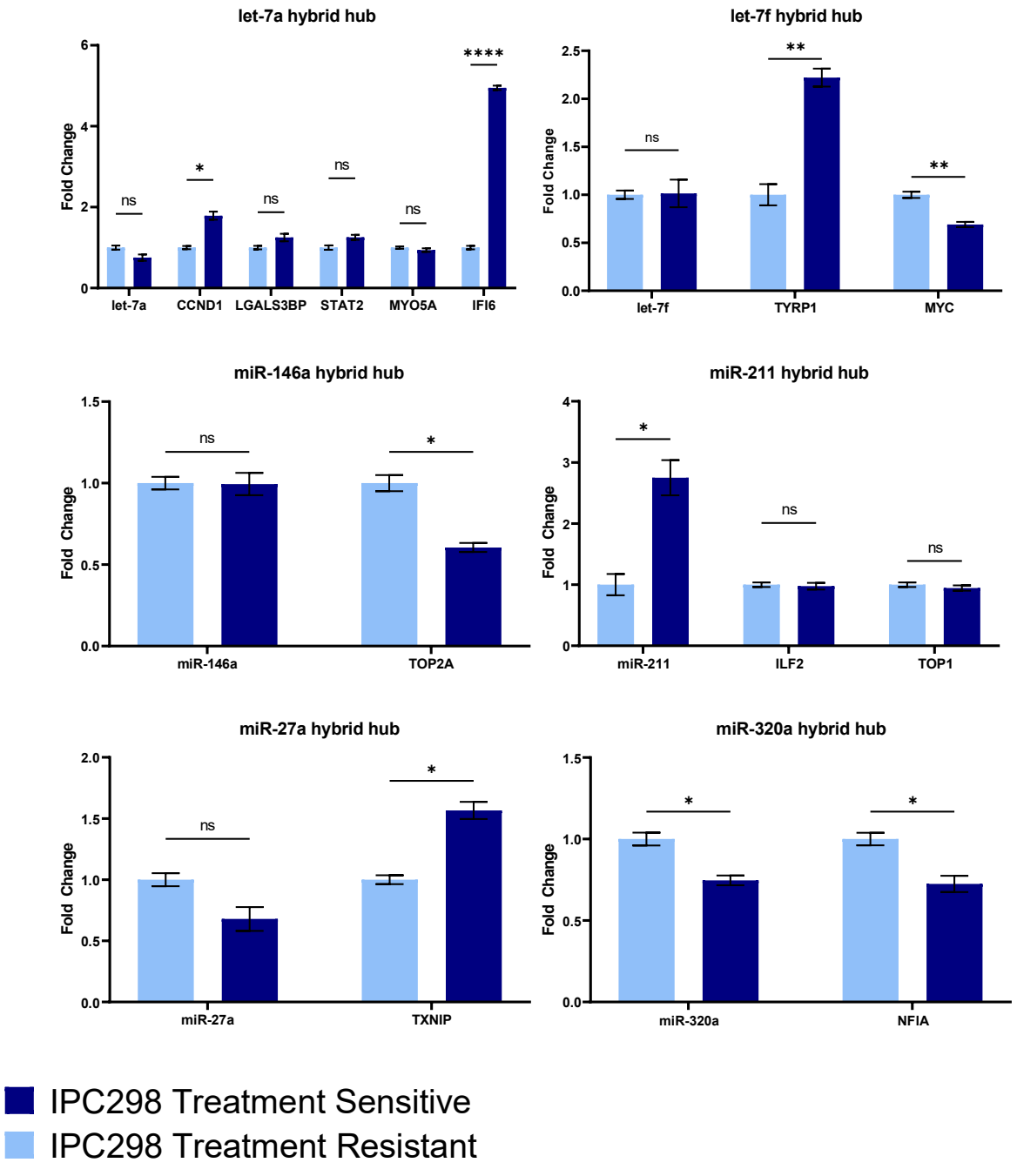

Supplementary Figure 15.

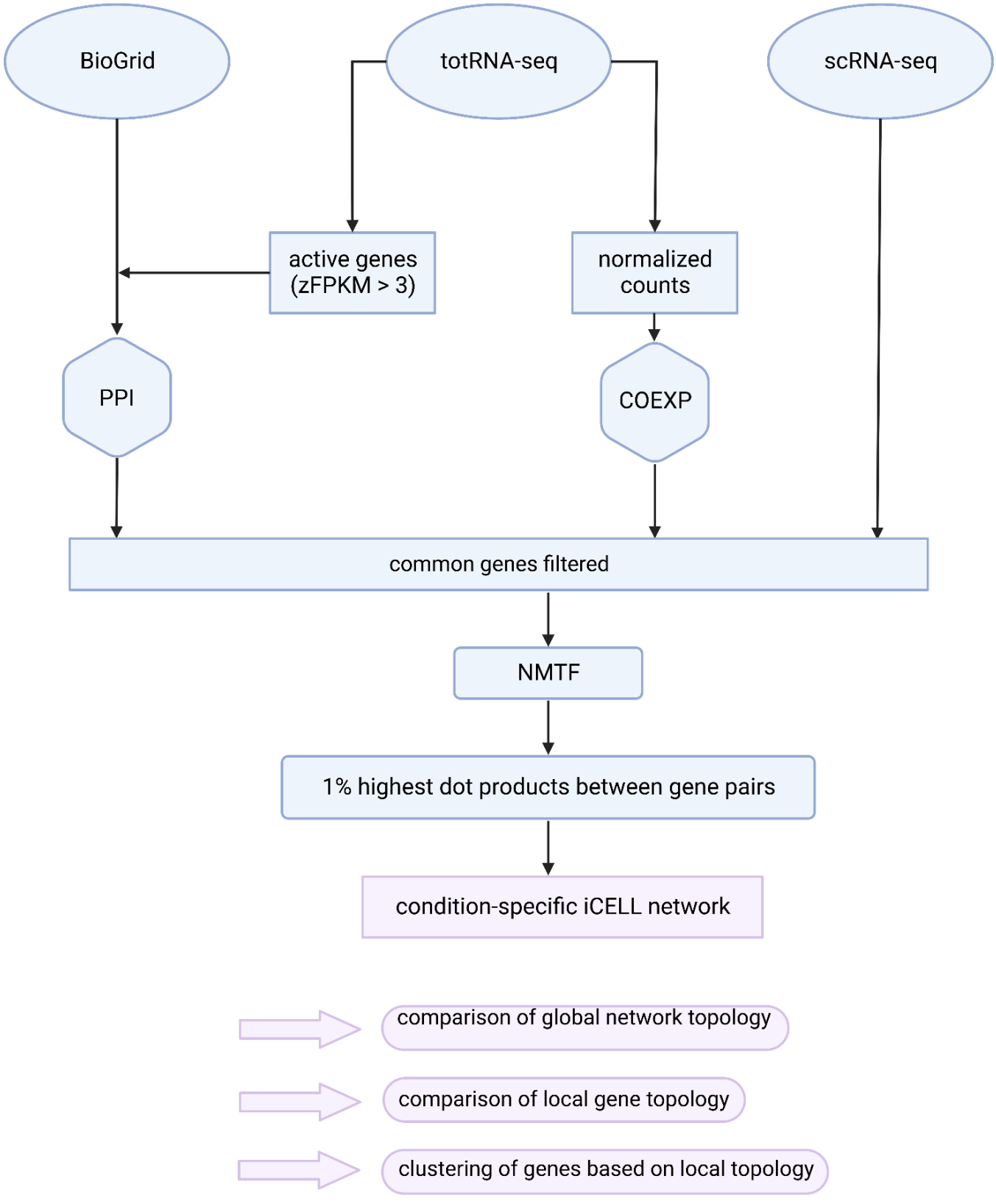

Supplementary Figure 16.

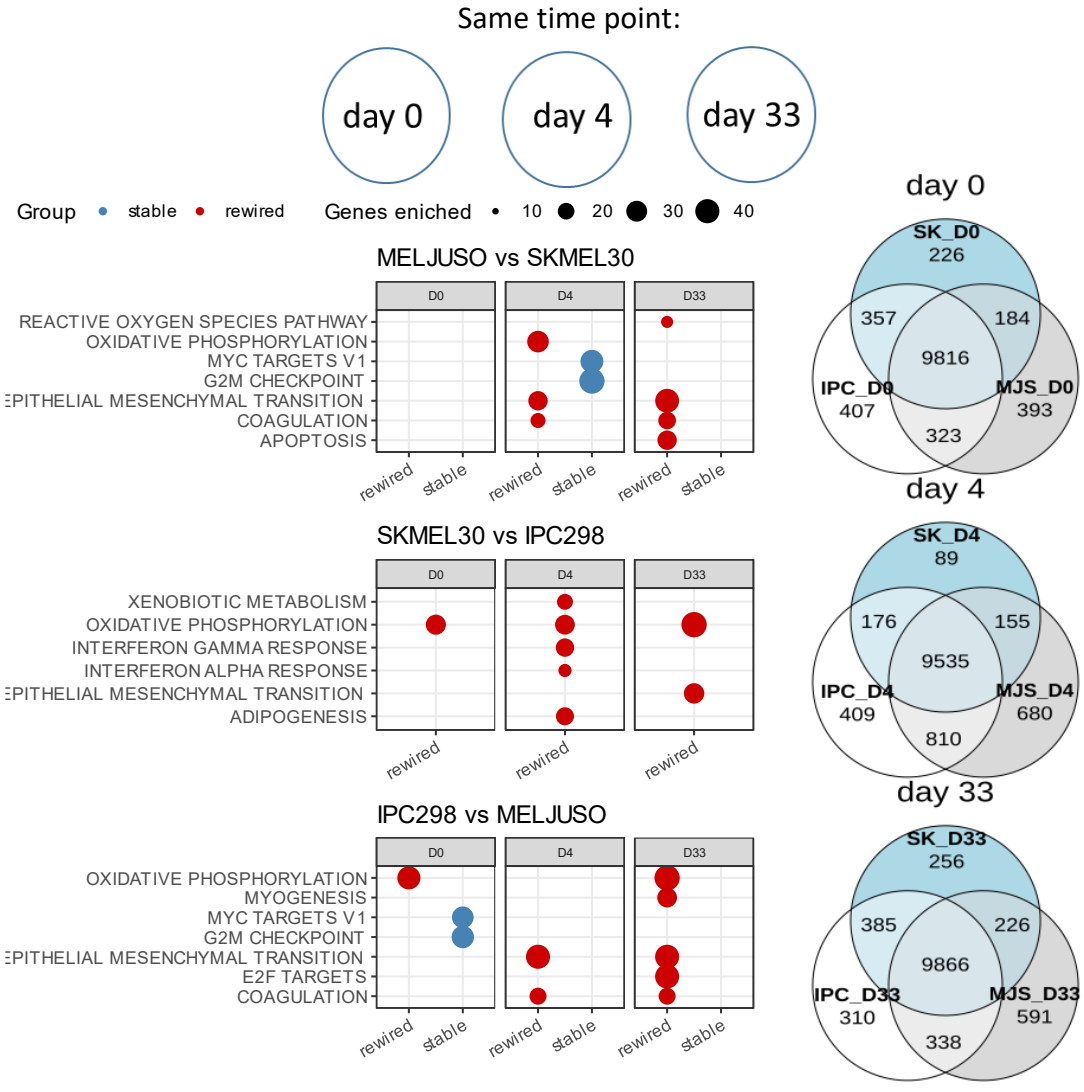

Supplementary Figure 17.

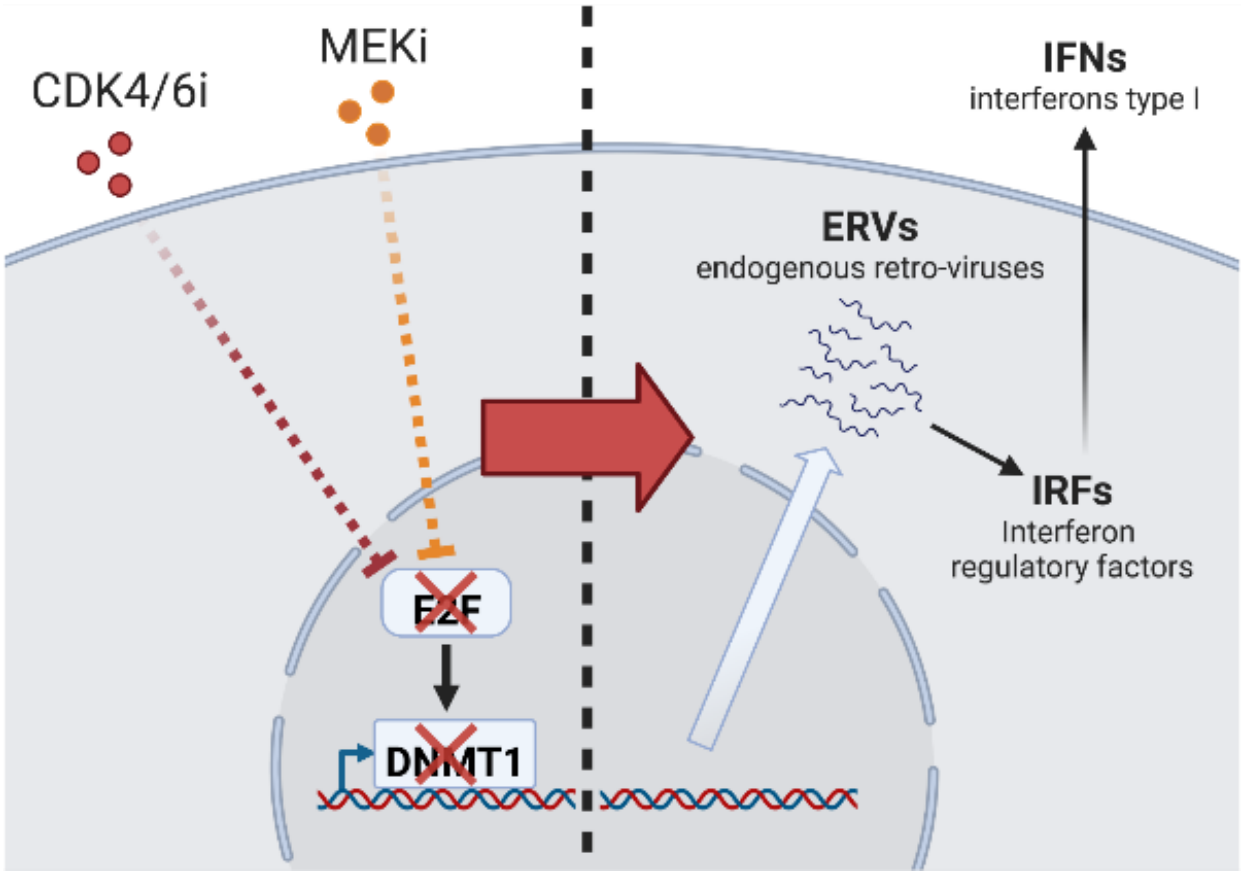

Supplementary Figure 18.

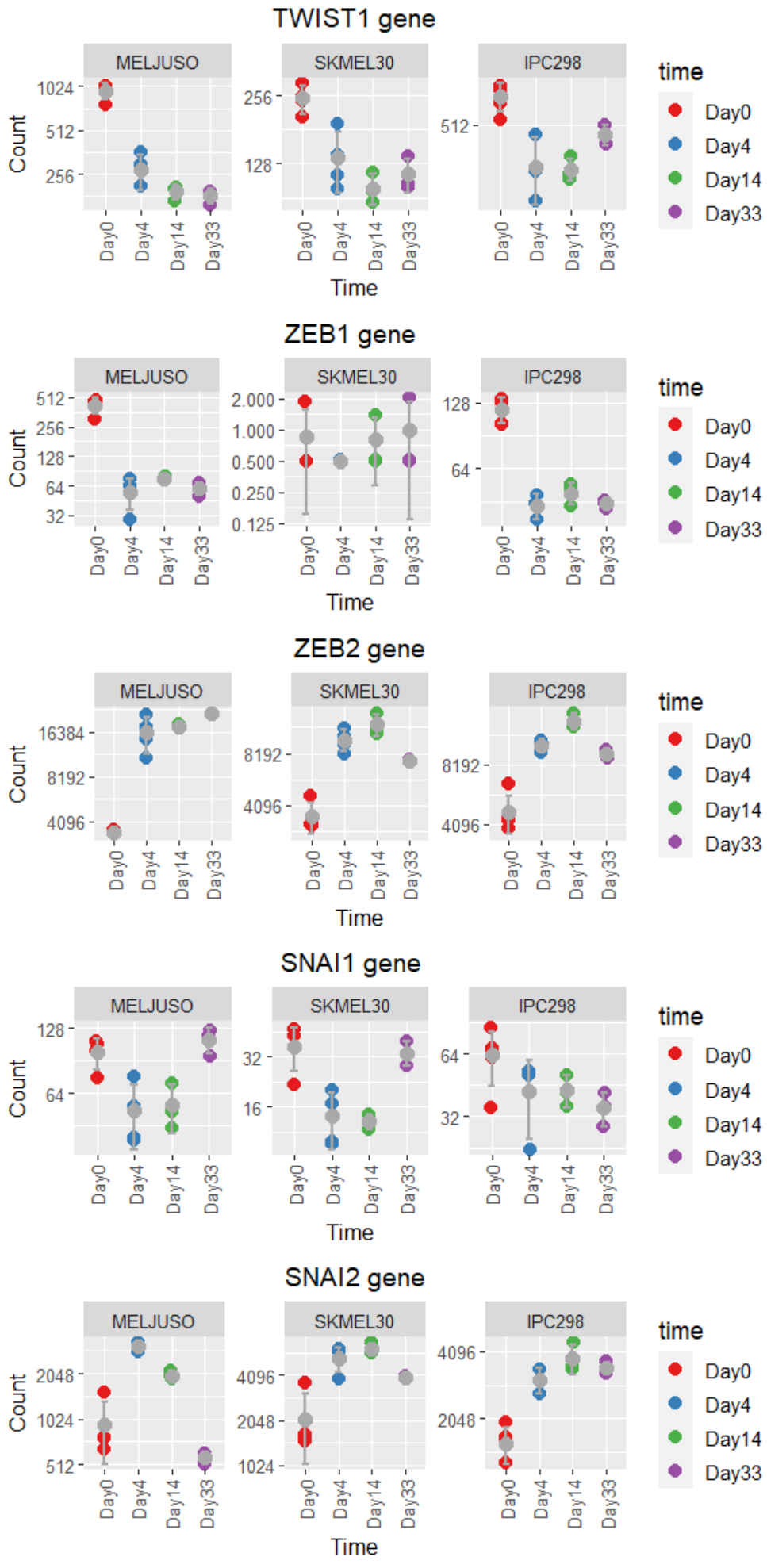

Supplementary Figure 19.

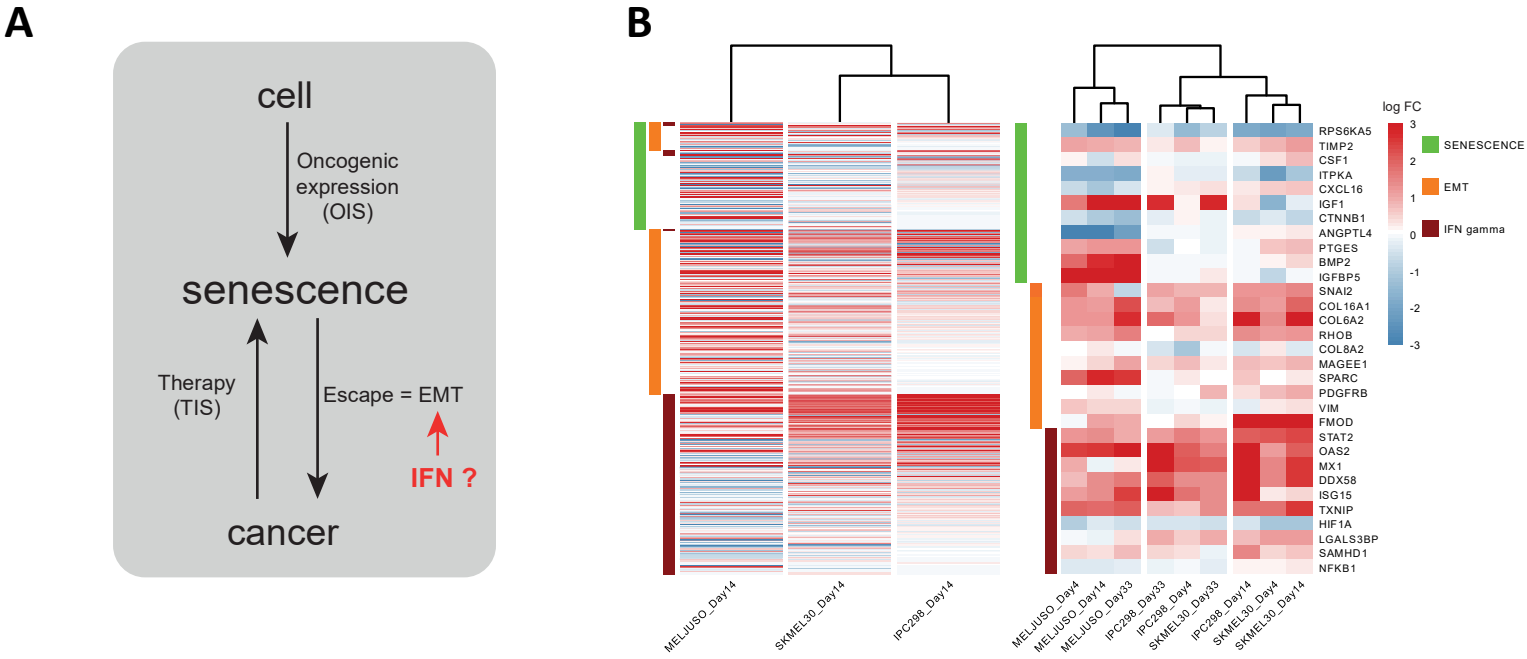

Supplementary Figure 20.

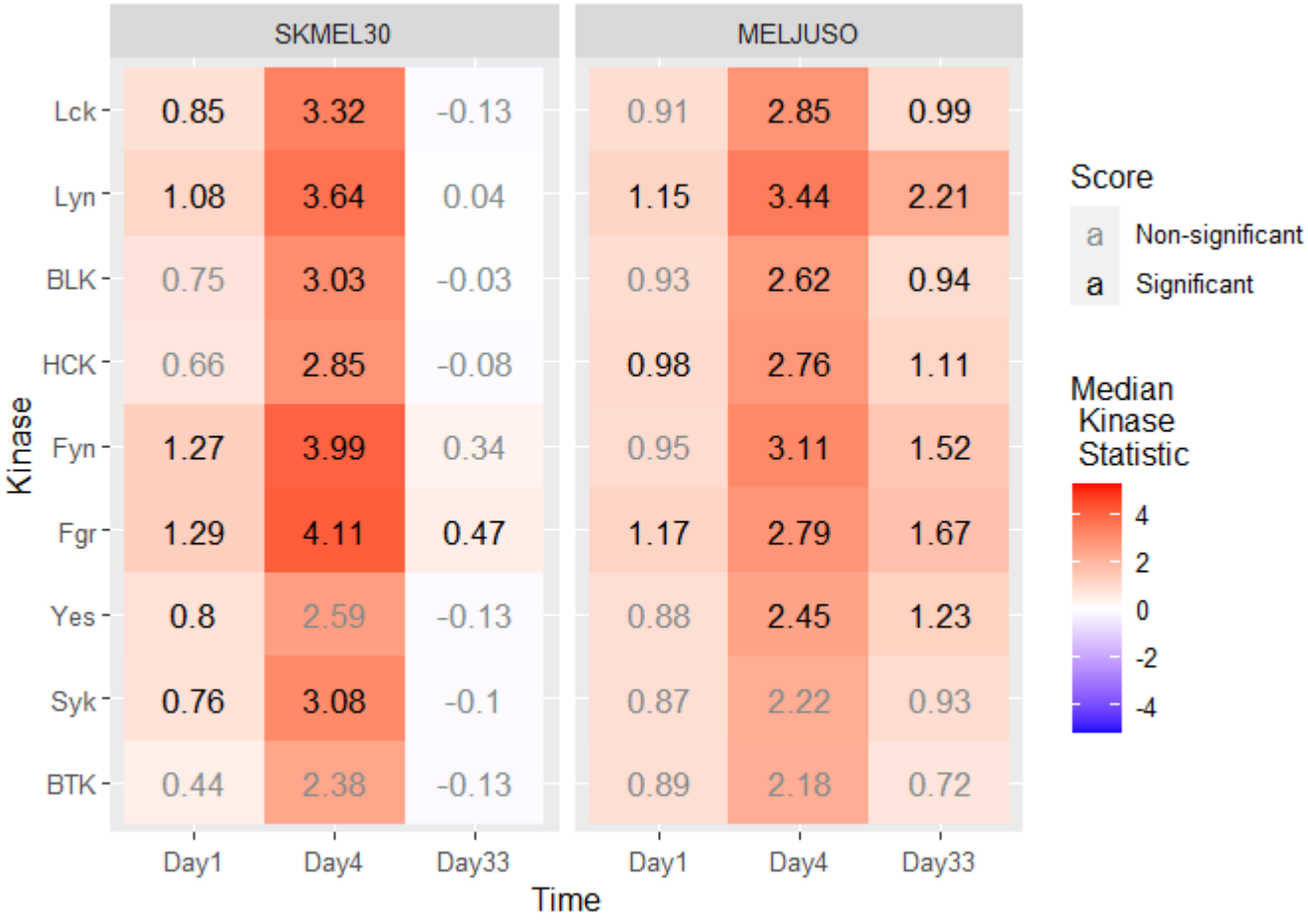

Supplementary Figure 21.

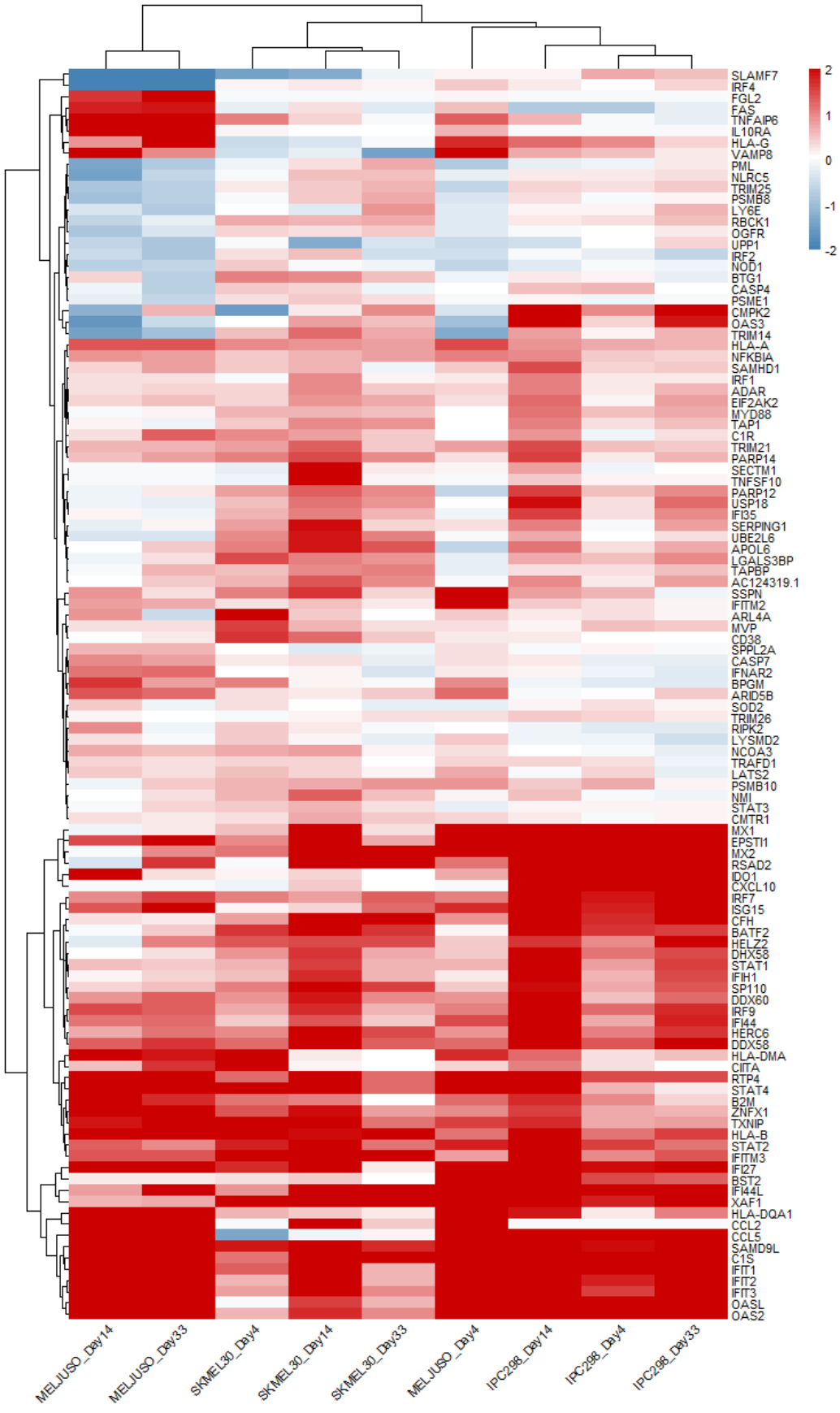

Supplementary Figure 22.

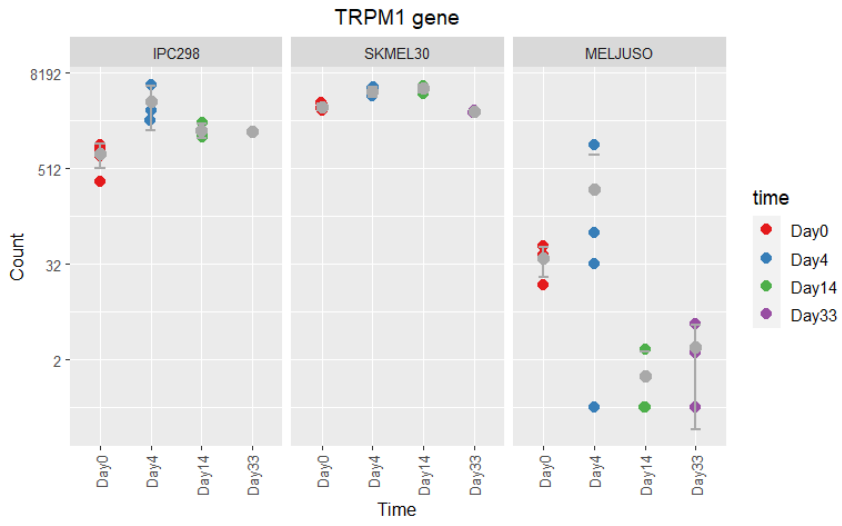

Supplementary Figure 23.

Supplementary Tables

	Gender	Stade	Mutations	Binimetinib (MEKi)	Palbociclib (CDK4/6i)	Phenotype
MELJUSO	Female	Primary	NRAS, TP53, CDKN2A, TERT, APC	110nM	1µM	Filliform
SKMEL30	Male	Metastatic	NRAS, HRAS	35nM	1µM	Pigmented
IPC298	Female	Primary	NRAS, TP53, CDKN2A, TERT	16nM	1µM	Normal
A375	Female	-	BRAF, CDKN2A, TERT	30nM	1µM	-
624MEL	Male	-	BRAF, TP53	50nM	1µM	-

Supplementary Table 1.

Gene	Total number of clusters enriched	Hierarchical clustering	k-medoids
NEAT1	8	3	5
GOLGB1	7	3	4
HMG20B	7	3	4
LUC7L3	7	3	4
MFSD12	7	3	4
S100B	7	3	4
TAX1BP1	7	3	4
TIMP2	7	3	4
ACTG1	6	3	3
ANXA5	6	3	3
B2M	6	3	3
BPTF	6	3	3
CANX	6	3	3
CD63	6	3	3
CHD4	6	3	3
CTSD	6	3	3
FTL	6	3	3
GNAS	6	3	3
GPNMB	6	3	3
HLA-A	6	3	3
HLA-C	6	3	3
HSP90B1	6	3	3
HSPA5	6	3	3
IGFBP7	6	3	3
KTN1	6	3	3
LGALS3BP	6	3	3
LMNA	6	3	3
NCL	6	3	3
PSAP	6	3	3
S100A6	6	3	3
SERF2	6	3	3
TMSB10	6	3	3
TOMM7	6	3	3
TUBA1A	6	3	3
UBC	6	3	3
YWHAB	6	3	3
ANXA2	5	3	2
CALR	5	3	2
CBX3	5	3	2
CCND1	5	3	2
CCT6A	5	3	2
DDX5	5	3	2
DSTN	5	3	2
EIF3A	5	3	2
FTH1	5	3	2
GAPDH	5	3	2
HLA-DRB1	5	3	2
HNRNPA2B1	5	3	2
HNRNPU	5	3	2
HSPB1	5	3	2
LIMA1	5	3	2
MAP4	5	3	2
MATR3	5	3	2
NDUFA4	5	3	2
PEBP1	5	3	2
PLP1	5	3	2
PRRC2C	5	3	2
RBM25	5	3	2
S100A10	5	3	2
SPTBN1	5	3	2
SQSTM1	5	3	2
SYNM	5	3	2
TPT1	5	3	2
YWHAZ	5	3	2
CAPN3	5	2	3
CDC37	5	2	3
HSP90AA1	5	2	3
HSP90AB1	5	2	3
AHNAK	4	2	2
AKAP12	4	2	2
CD74	4	2	2
CTNNA1	4	2	2
DAG1	4	2	2
HLA-B	4	2	2
HLA-DPB1	4	2	2
HLA-DRA	4	2	2
HSPG2	4	2	2
ITGA6	4	2	2
MCAM	4	2	2
MEGF9	4	2	2
MTDH	4	2	2
NQO1	4	2	2
PABPC1	4	2	2
PRNP	4	2	2
SNRNP35	4	2	2
TBC1D16	4	2	2
TMED9	4	2	2
WBP4	4	2	2
ZC3H13	4	2	2
ZNF121	4	2	2

Supplementary Table 2.

Gene	Forward Primer (5' - 3')	Reverse Primer (5' - 3')	Size (bp)
NFIA	AGTGGATGGCATGAAGTGGA	CAGGGAGGAGGTCTGTGAAG	105
ILF2	CGTGGAAAGCCTAAGAGCAC	AAGATTGGGTGGCACTGTTG	127
TOP2A	CGCCCAGACACCTACATTG	TGTTTGTTGTCCGCAGCATT	155
LGALS3BP	TGAGTGTGGATGCTGAGTGT	CTTGACTGACGACAGGGTGA	94
CCND1	AGAGGCGGAGGAGAACAAAC	ATGGAGGGCGGATTGGAAAT	99
TXNIP	GAGCCAGCCAACTCAAGAGA	GAGCAGAGACAGACACCCGC	152
TOP1	GAATCAAGGGTGAGAAGG	GATGAAGTACAGGGCTAC	146
STAT2	GTTCTCCTCCTATGTTGG	CTCTCGCTTAGTGAAGTC	127
MYC	ACAGCATACATCCTGTCCGT	CGCACAAGAGTTCCGTAGC	119
MYO5A	CGGAAAGACCTGGAGCAAACTC	TGCTGCACGATGCGGTGATTGA	153
IFI6	GTGGCTGCCTCGCTGAT	TTACCTATGACGACGCTGCT	119
TYRP1	ACCAGAGGGTTCTCATAGTCAG	GCTTTGCCATATCCAGGG	90
HPRT	TGGACAGGACTGAACGTCTT	GAGCACACAGAGGGCTACAA	77
PPIA	CAGACAAGGTCCCAAAGACA	CCATTATGGCGTGTGAAGTC	139
TBP	ACCCAGCAGCATCACTGTT	CGCTGGAACTCGTCTCACTA	120

miRNA	Forward Sequence	ISB-UNI Sequence
miR-146a	UGAGAACUGAAUUCCAUGGGUU	ATCGAGCACCAGTTACGC
miR-211	UUCCCUUUGUCAUCCUUCGCCU	""
miR-320a	AAAAGCUGGGUUGAGAGGGCGA	""
miR-27a	UUCACAGUGGCUAAGUUCCGC	""
let-7a	UGAGGUAGUAGGUUGUAUAGUU	""
let-7f	UGAGGUAGUAGAUUGUAUAGUU	""

Supplementary Table 3.